Master's Thesis of Engineering

Behavior and Design of Longitudinal Plate-to-CHS Joints under Combined Axial Loading and In-plane Bending

축력과 모멘트를 동시에 받는 횡방향
플레이트–원형강관 접합부의 거동과 설계

August 2021

Graduate School of Engineering
Seoul National University
Architecture and Architectural Engineering

Sang-Hui Han

Behavior and Design of Longitudinal Plate-to-CHS Joints under Combined Axial Loading and In-plane Bending

Advisor: Cheol-Ho Lee

Submitting a Master's thesis of
Architecture and Architectural Engineering

August 2021

Graduate School of Engineering
Seoul National University
Architecture and Architectural Engineering

Sang-Hui Han

Confirming the Master's thesis written by
Sang-Hui Han

July 2021

Chair

Vice Chair

Examiner

Abstract

Behavior and Design of Longitudinal Plate-to-CHS Joints under Combined Axial Loading and In-plane Bending

Sang-Hui Han
Department of Architecture and Architectural Engineering
College of Engineering
Seoul National University

Up-to-date design rules for tubular joints with welded branch plate(s) were recently formulated in prEN 1993-1-8. For plate-to-circular hollow section (CHS) joint, the design rules cover joints of high-strength steel tubular members whose yield stress is up to 460 MPa by incorporating the material factor (or joint strength reduction factor). These limitations on the high-strength steel joints are from concerns about lower strain hardening and the reduced ductility of high-strength steel compared to mild steel. However, the background data for the regulations need to be further augmented. In this study, to evaluate the current limitations on high-strength steel for plate-to-CHS joint, the strength and ductility of the high-strength steel joint were investigated based on the experimental and test-validated numerical studies. Meanwhile, it was also noted that the current design standards or guides do not provide an interaction relationship for the design of joints under combined axial

compression and in-plane bending (IPB). To establish an interaction relationship of combined axial compression and IPB for longitudinal plate-to-CHS joints, the numerical parametric study was conducted.

In the experiment, high-strength steel with a yield stress of 460 or 700 MPa was applied on the longitudinal X-type plate-to-CHS joints. The deformation capacity for the high-strength steel joints was sufficient relative to the ultimate deformation limit which determines the joint strength. The joint strength also provided high safety margin compared to the design resistance, suggesting that the yield stress limitation ($f_y \leq 460$ MPa) may be relaxed. The material factor for steel grade 460 was further investigated based on an extensive test-validated numerical analysis. Longitudinal X- and T-type plate-to-CHS joints were considered in the analysis, and their nondimensional geometric parameters were carefully chosen to induce a ductile chord plastification failure only. For the loading conditions, the combined axial compression and IPB were included in addition to the individual loading case. It was first shown that when IPB loading is involved, the use of a widely accepted 3% deformation limit criterion often yields a conservative joint strength rating. A more reasonable criterion is proposed considering both the 3% indentation limit and an additional limit in terms of the joint rotation angle. With the new deformation limit criterion, the code-specified material factor (0.90) for steel grade 460 was found to be appropriate for the X- and T-joints regardless of the loading type. Moreover, based on the analysis results of this study, the use of a linear interaction equation is newly proposed for both mild and high-strength steel joints.

Keyword: High-strength steel; Plate-to-circular hollow section (CHS) joints; X-joint; T-joint; P-M interaction;

Student Number: 2019-29294

Contents

List of Tables

List of Figures

List of Symbols

C_f : Material factor

$C_{f,req}$: Required material factor

CoV : Coefficient of variation

d_0 : Chord diameter

f_y : Yield stress

f_{y0} : Chord yield stress

f_u : Ultimate stress

f_{u0} : Chord ultimate stress

h_1 : Branch plate depth

L_0 : Chord length

L_1 : Branch plate length

M : Sample mean

M_0 : Bending moment applied to chord

M_{ip} : IPB moment applied to joint

$M_{ip,Rd}$: Deign resistance for joints under IPB

M_{p0} : Plastic moment capacity of chord

M_{peak} : Peak bending moment applied to joint

M_{prEN} : Deign resistance for joints under IPB according to prEN 1993-1-8

M_u : Ultimate joint strength under IPB

M_{uc} : IPB component of ultimate joint strength under combined loading

N : Axial load applied to joint

N_{peak} : Peak axial load applied to joint

N_{prEN} : Deign resistance for joints under axial compression according to prEN 1993-1-8

N_{Rd} : Deign resistance for joints under axial compression

N_u : Ultimate joint strength under axial load

N_{uc} : Axial compression component of ultimate joint strength under combined loading

Q_f : Chord stress function

t_0 : Chord thickness

t_1 : Branch plate thickness

$t_{1,eff}$: Effective plate thickness ($t_{1,eff} = t_1+2w$)

w : Weld leg size

α : Chord length-to-radius ratio ($\alpha = 2(L_0/d_0)$)

α' : Effective chord length parameter ($\alpha' = 2(L_0 - h_1)/d_0$)

β : Branch plate thickness-to-chord diameter ratio ($\beta = t_1/d_0$)

β' : Effective branch plate thickness-to-chord diameter ratio ($\beta' = t_{1,eff}/d_0$)

2γ : Chord diameter-to-thickness ratio ($2\gamma = d_0/t_0$)

δ_1, δ_2 : Joint deformations at crown points

δ_{avg} : Average joint deformation ($\delta_{avg} = (\delta_1 + \delta_2)/2$)

δ_{lim} : Deformation limit for axially loaded joint

η : Branch plate depth-to-chord diameter ratio ($\eta = h_1/d_0$)

φ : Joint rotation angle

φ_{lim} : Proposed joint rotation angle limit for joints under IPB

$\varphi_{lim,Yu}$: Joint rotation angle limit proposed by Yu (1997)

$\varphi_{lim,Lu}$: Joint rotation angle limit proposed by Lu and Wardenier (1994)

$\varphi_{lim,Kim}$: Joint rotation angle limit proposed by Kim and Lee (2021)

Chapter 1. Introduction

1.1. Research Background

1.1.1. Tubular joints with high-strength steel

Tubular members have many advantages in terms of their structural performance as a closed section and are aesthetically appealing. The application of high-strength steel in tubular members can bring about further advantages owing to the reduction in section size and weight. Regarding steel materials used in tubular members, those with a yield stress (f_y) of approximately 460 MPa or higher are typically classified as high-strength steel.

In response to the increasing demand for such steel, active investigations have recently been conducted on the structural behavior of high-strength steel tubular members and their joints (e.g., Kim et al. (2013), Meng and Gardner (2020), Lee et al. (2017), and Lan et al. (2020)). Specifically, representative international design standards such as ISO 14346 (ISO (2013)) and prEN 1993-1-8 (CEN (2019)) have tried to extend their tubular joint design provisions to high-strength steel of up to f_y = 460 or 700 MPa beyond the traditional upper limit of f_y = 355 MPa. Following these standards, high-strength steel tubular joints can be designed but with a reduced design resistance by imposing the strength reduction factor (or the material factor, C_f) and limiting the yield stress to less than 80% of the ultimate tensile stress ($0.8f_u$).

These restrictions are primarily related to the low strain hardening and reduced ductility of high-strength steel materials (Kim and Lee (2020)). In Figure 1.1, the stress-strain curves of high-strength steel and mild steel obtained from Kim and Lee (2018) are described. The material properties of high-strength steel have characteristics of higher yield ratio, lower strain hardening, and indistinct yield plateau compared to mild steel, indicating low ductility of the material.

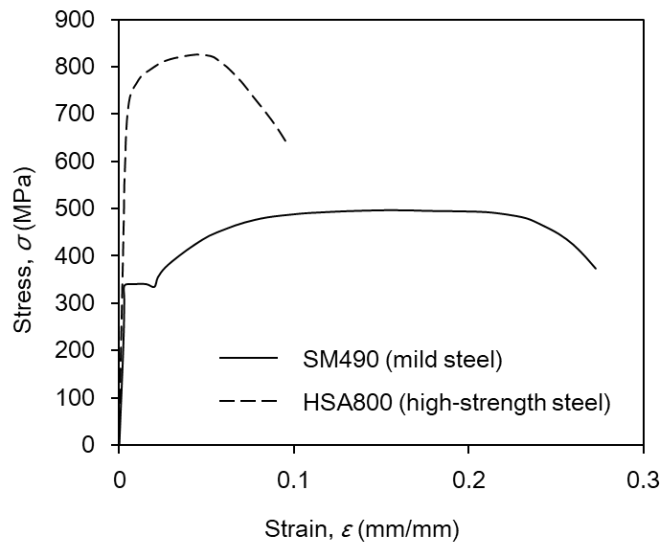

Figure 1.1. Stress-strain curves of high-strength steel and mild steel obtained from Kim and Lee (2018)

1.1.2. Plate-to-CHS joints with high-strength steel

For plate-to-circular hollow section (CHS) joint, ISO 14346 (ISO (2013)) and prEN 1993-1-8 (CEN (2019)) cover $f_y \leq 460$ MPa with $C_f = 0.9$ for $355 < f_y \leq 460$ MPa, and also limit the yield stress to less than $0.8f_u$. It should be noted that the use of $C_f = 0.9$ for $f_y = 460$ MPa was originally proposed for a rectangular hollow section (RHS)-to-RHS gap K-joint (Liu and Wardenier (2004)), and extended later to all other types of joints. A recent extensive analysis of the test database for high-strength

steel tubular joints (Wardenier (2020)) indicated that the effect of the steel grade can vary depending on the joint types and failure modes, implying that a current material factor of 0.9 for f_y = 460 MPa may be inappropriate for some types of joints and their relevant design limit states. Because the mechanical background behind the limitations for high-strength steel plate-to-CHS joints is not clear, the code-specified material factor 0.9 needs to be re-examined.

Meanwhile, for high-strength steel joints, the fracture failure may become critical because of its low ductility (see Fig 1.1), causing rapid failure at earlier deformation level than mild steel joint. Moreover, due to the high stress concentration on the plate-to-CHS joint along the weld line, the effect of high-strength steel on the deformation capacity and failure mode of the joint under tension load is necessary.

1.1.3. Plate-to-CHS joints under combined loading

In the case of plate welded tubular joints, although the axial load and bending moment often act simultaneously, current design standards do not clearly suggest the interaction equation. ISO 14346 (ISO (2013)) provides an interaction equation, as shown in equation 1.1, for CHS joints based on the experimental evidence (Hoadley (1984)). This equation is applicable only to the CHS-to-CHS connections and therefore, in this study, a test-validated finite element (FE) analysis is performed to evaluate whether the existing interaction equation can be extrapolated to longitudinal plate-to-CHS joints, or if different interaction equations are required.

$$\frac{N}{N_{Rd}} + \left(\frac{M_{ip}}{M_{ip,Rd}} \right)^2 \leq 1.0 \qquad (1.1)$$

where N and M_{ip} are the axial load and in-plane bending (IPB) acting simultaneously on the joint, and N_{Rd} and $M_{ip,Rd}$ are the axial and IPB design resistances, respectively.

The out-of-plane bending term was omitted because it is not relevant to the joints with longitudinally welded branch plate.

1.2. Objectives and scope

The joint types studied in this thesis were limited to longitudinal X- and T-type plate-to-CHS joint (longitudinal XP and TP joint, respectively). In the experimental program, longitudinal XP joints with steel grades 460 and 700 under tension load or IPB were considered in order to confirm the deformation capacity and failure mode of high-strength steel joints. In the parametric study, steel grades 235 (mild steel) and 450 (high-strength steel) were applied to longitudinal XP and TP joints under axial compression or IPB. The influence of the steel grade on the chord plastification behavior of longitudinal branch plate-to-CHS joints was investigated, and the relevant material factors were evaluated. The behavior of plate-to-CHS joint under combined axial compression and IPB was also examined and a new interaction equation was proposed together with the new ultimate deformation limit for the combined loading.

1.3. Overview of research program

This thesis contains five chapters.

Chapter 1 provides an introduction, objectives and scopes of this research work.

Chapter 2 reviews the existing design recommendations and previous research related to this study.

Chapter 3 shows the experimental program of longitudinal XP joints with high-strength steel under branch tension or IPB.

Chapter 4 shows parametric studies for longitudinal XP and TP joint under branch plate compression, IPB, and their combined load with applying mild steel and high-strength steel.

Chapter 5 gives conclusions of this thesis.

Chapter 2. Literature Review

2.1. Existing design recommendations for plate-to-CHS joint

2.1.1. Failure modes and design resistance formulae

For plate-to-circular hollow section (CHS) joint, there are two representative limit states of chord plastification and chord punching shear. The design for the plate

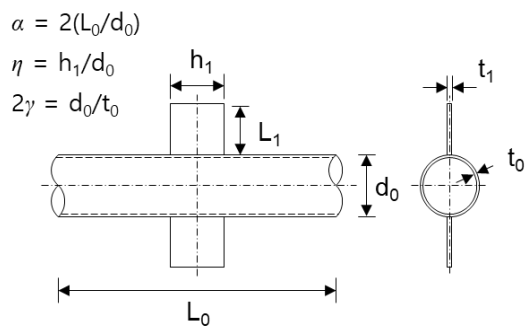

(a) Longitudinal XP joint

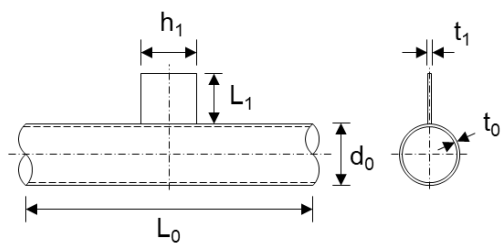

(b) Longitudinal TP joint

Figure 2.1. Configurations and definition of symbols for longitudinal plate-to-CHS joints

yielding and the failure of weld should be also considered. Table 2.1 summarizes the design formulae of chord plastification and chord punching shear for longitudinal plate-to-CHS joint according to prEN 1993-1-8 (CEN (2019)) and ISO 14346 (ISO (2013)). The design recommendations in prEN 1993-1-8 and ISO 14346 are almost identical. Nonetheless, in this study, prEN 1993-1-8 was mainly discussed because it reflected the latest research on the plate-to-CHS joints. In Figure 2.1, the configuration and definition of symbols of longitudinal X- and T-type plate-to-CHS

Table 2.1. Design resistance formulae for longitudinal plate-to-CHS joints

Limit state	Design resistance formulae	
Chord plastification under axial load [a]	ISO 14346	$N_{Rd} = 5C_f f_{y0} t_0^2 (1+0.25\eta) Q_f$
	prEN 1993-1-8	X-type $N_{Rd} = 4.4C_f f_{y0} t_0^2 (1+0.4\eta) Q_f$
		T-type $N_{Rd} = 7.1C_f f_{y0} t_0^2 (1+0.4\eta) Q_f$
Chord plastification under in-plane bending	ISO 14346	$M_{ip,Rd} = 0.8 N_{Rd} h_1$
	prEN 1993-1-8	$M_{ip,Rd} = 0.7 N_{Rd} h_1$
Chord punching shear	$\frac{N}{A_1} + \frac{M_{ip}}{W_{el,ip,1}} \le 1.16 f_{y0} \frac{t_0}{t_1}$ N, M_{ip}: brace load acting, A_1, $W_{el,ip,1}$: area and elastic section modulus of plate	
Chord stress function (Q_f)	$Q_f = \left(1 - \lvert n \rvert\right)^{0.20}$ for chord in tension $Q_f = \left(1 - \lvert n \rvert\right)^{0.25}$ for chord in compression $n = \frac{N_0}{N_{pl,0}} + \frac{M_0}{M_{pl,0}}$ N_0, M_0: chord axial force and bending moment, $N_{pl,0}$, $M_{pl,0}$: chord axial yield capacity and plastic moment capacity	

[a] C_f: see Table 2.2

joint (longitudinal XP and TP joint, respectively) are shown.

The chord stress function in Table 2.1 is purpose to reflect the reduction in joint strength due to the stress acts on the chord. Though the chord stress effect is beyond the scope of this thesis, the use of chord stress function was inevitable due to the induced internal force of the joint that cannot be compensated, which will be discussed in Chapter 4.

i. Chord plastification

Chord plastification is a ductile failure mode in which overall plastification is exhibited on the chord with excessive deformation. The chord plastification design formulae are based on the analytical ring model approach (Togo, 1967). The influence functions for η, β, and γ were adjusted to the ring model equation using multi-regression analyses of the experimental and FE results, and have been adopted to various design standards (Wardenier (2008)).

In the ring model, the plastic hinges were assumed in the simplified 2-dimensional CHS-to-CHS joint. The ring model approach is a method of analytically calculating the joint strength from the moment equilibrium equation derived by the free body diagram of the assumed model. The induced joint strengths using ring model approach for CHS-to-CHS X- and T-joint are written as equations 2.1 and 2.2, respectively.

$$N_u = \frac{2(B_e / d_0)}{1-\beta} f_{y0} t_0^2 \tag{2.1}$$

$$N_u = f(\beta) \cdot 2(B_e / d_0) f_{y0} t_0^2 \tag{2.2}$$

where B_e is effective length of the chord assumed that the joint load is distributed over the effective length, and $f(\beta)$ in equation 2.2 is a function of shear load transfer

in the ring model, which is rather complicated form. It is noteworthy that for longitudinal joint, β term in the equations is assumed to be zero due to the small plate thickness.

Chord plastification design formula for plate-to-CHS joint under in-plane bending (IPB) is based on the assumption that the joint subjected to IPB is mechanically identical to the joint subjected to axial load with an eccentric distance. In the formula, the term of $0.7h_1$ (or $0.8h_1$) means effective moment arm.

The analytical equations 2.1 and 2.2 have been a basis of the existing design formulae. Using regression analysis, the equations developed for plate-to-CHS joints design formulae in Table 2.1.

ii. Chord punching shear

Chord punching shear is a brittle failure mode in which the plate is to be separated from the chord along the weld by crack initiation at a point of high stress concentration on the chord. The uniform shear yield stress per unit length can be expressed as equation 4.3. The chord punching shear strength for longitudinal plate-to-CHS joints can be presented by multiplying the perimeter length of the weld and equation 4.3 (see equation 4.4). However, the existing design formula in Table 4.1 is suggested to neglect the length of weld leg (w) and plate thickness (t_1), as a conservatism.

$$\frac{f_{y0}t_0}{\sqrt{3}} \tag{2.3}$$

$$2(h_1 + t_1 + 4w)\frac{f_{y0}t_0}{\sqrt{3}} \tag{2.4}$$

2.1.2. Range of applicability

i. Material limitations

As mentioned in Section 1.1, the design standards, such as ISO 14346 (ISO (2013)) and prEN 1993-1-8 (CEN (2010)), limit the use of high-strength steel on the tubular joints due to the less strain-hardening and lower ductility of high-strength steel. The applicable range of material for plate-to-CHS joint is summarized in Table 2.2. ISO 14346 and prEN 1993-1-8 propose identical range: $f_y \leq 460$ MPa and $f_y/f_u \leq 0.8$. The material factor (C_f) 0.9 should be applied to design resistance for the joint with $355 < f_y \leq 460$ MPa. The yield ratio limitation is suggested in order to allow ample joint ductility in cases where brittle failure govern since strength formulae for these failure modes are based on the yield stress (Wardenier et al. (2008)).

Table 2.2. Applicable range of material for plate-to-CHS joint

Property	Applicable range
Yield stress f_y	The material factor C_f should be multiplied as follows: (1) 1.0 for $f_y \leq 355$ MPa (2) 0.9 for $355 \leq f_y \leq 460$ MPa
Yield ratio f_{y0}/f_{u0}	≤ 0.80 (when yield ratio exceeds 0.8, f_{y0} should be taken as $0.8f_{u0}$)

ii. Geometric properties

The suggested applicable range of geometric properties for longitudinal plate-to-CHS joints according to ISO 14346 and prEN 1993-1-8 is summarized in Table 4.3. Joints with parameters outside these specified ranges of validity are allowed, but they may result in lower joint efficiencies and generally require considerable engineering judgement and verification (Wardenier et al. (2008)). In Table 4.3, class 1 and 2 indicate section classification that provide the extent to which the resistance and

rotation capacity of a cross section are limited by its local buckling resistance, and the class limitation is depending on the steel grade. Although one tested specimen in this study violated the section limitation due to the very high yield stress, the study on the section classification will not be dealt with in this thesis because it is outside the scope and the chord section did not exhibit local buckling during the test.

Table 2.3. Applicable range of geometric properties for longitudinal plate-to-CHS joint

Nondimensional parameter	Applicable range
$2\gamma = d_0/t_0$	Compression chords must be class 1 or 2 and $2\gamma \leq 50$ (T-type) or $2\gamma \leq 40$ (X-type) Tension chords must be $2\gamma \leq 50$ (T-type) or $2\gamma \leq 40$ (X-type)
$\eta = h_1/d_0$	ISO 14346 $1 \leq \eta \leq 4$ prEN 1993-1-8 $0.6 \leq \eta \leq 4$

2.2. Previous research

2.2.1. Brief history of plate-to-CHS joint studies

Makino et al. (1994) conducted a set of experiments on plate-to-CHS joints under an axial load or IPB and collected test data from other sources, including Akiyama et al. (1974), Washio et al. (1970), and Makino (1984). The existing design resistance formulae (1970–1980s) were evaluated using the collected data, wherein the yield stress of the chord ranged from 272 to 490 MPa. Makino et al. (1994) defined the joint strength as the peak load, or if there was no clear peak, as the load at which the regaining of the joint stiffness commenced. The load at the end of the test was reported when the joint strength could not be determined, as described above. It should be noted that, since the 1990s, the tubular joint strength has been generally

defined as the preceding load among the ultimate load or the load corresponding to some ultimate deformation limit. An out-of-plane deformation of the chord face corresponding to 3% of the chord diameter (3%d_0) suggested by Lu et al. (1994) has been widely accepted as the ultimate deformation limit (Wardenier (2008)). Unfortunately, when based on the deformation limit criterion, the utilization of the numerous Japanese test data (Makino et al. (1994), Akiyama et al. (1974), Washio et al. (1970) and Makino (1984)) is greatly limited, except for a few studies providing a full load-deformation diagram.

Voth and Packer (2012a) conducted experiments on plate-to-CHS joints under axial loads. Mild steel with a measured yield stress of 389 MPa was used. They concluded that the chord plastification design resistance in ISO 14346 (ISO (2013)) was highly conservative for all types of plate-to-CHS joints. In addition, Voth (2010) and Voth and Packer (2012a, 2012b) conducted numerical studies on transverse or longitudinal XP and TP joints under compression or tension. They proposed new design recommendations for XP and TP joints, in which an improved prediction accuracy was achieved by including a plate thickness term in the resistance formulae. The design rules for the compressive and tensile brace-loading cases were proposed separately. Wardenier et al. (2018) slightly modified the Voth–Packer equations (Voth and Packer (2012a, 2012b)), and modified equations were adopted in prEN 1993-1-8 (CEN (2019)).

2.2.2. Deformation limit for tubular joints subjected to bending moment

During the formulation of the prEN 1993-1-8 design equations, Wardenier et al. (2018) rigorously applied the 3% deformation limit criterion to the database on axially loaded plate-to-CHS joints. Rigorous application of the deformation limit to the axially loaded case was possible because a large number of numerical data,

containing a full load-deformation relationship, were available. However, the 3% rule was not fully applied for the case under a bending moment because only the joint strength data reported by Makino et al. (1994) were used. As mentioned previously, Makino et al. (1994) did not consider any deformation-limit criteria.

For tubular joints subjected to a bending moment, joint deformation limits other than the 3%d_0 limit have been adopted as well. For RHS-to-RHS joints, Yu (1997) proposed using the 3%d_0 limit in combination with another limit corresponding to the joint rotation angle of 0.1 rad. The primary reason for introducing the 0.1 rad limit was that when based only on the 3%d_0 limit, an unrealistically large rotation angle would be permitted in the joints with small-sized braces. The 3%d_0 limit corresponds to $0.06/\eta$ (rad) in terms of the joint rotation angle, and Yu's limit on the joint rotation angle can be expressed as equation 2.5 below. The parameter η for the RHS-to-RHS joints is defined in the same manner as for longitudinal plate connections, or as the ratio of the brace height to chord width. Another joint rotation-based deformation limit was also proposed by Lu and Wardenier (1994) for I beam-to-RHS column connections under IPB, as shown in equation 2.6, and the 3%d_0 limit is not considered here. The parameter η in equation 2.6 represents the ratio of the I beam depth to the RHS width, and β represents the ratio of the I beam width to the RHS width.

$$\varphi_{lim,Yu} = \frac{0.06}{\eta} \leq 0.1 \text{ (rad)} \tag{2.5}$$

$$\varphi_{lim,Lu} = 0.1\frac{\beta}{\eta} \text{ (rad)} \tag{2.6}$$

More recently, Kim and Lee (2021) proposed a new deformation limit for CHS-to-CHS joints under IPB based on the concept of the available joint rotation capacity, which is defined by the ultimate-to-yield stress ratio of the chord material

(f_{u0}/f_{y0}) (equation 2.7). They observed that, for the CHS-to-CHS T-joints under IPB, the joint rotation at the peak was generally smaller in high-strength steel joints than in mild steel joints, which is opposite the general trend observed in axially loaded joints, wherein the joint indentation at the peak is generally larger in high-strength steel joints. Equation 2.7 is based on the observation that the low rotation capacity of high-strength steel joints under IPB is mainly due to the low strain-hardening property of high-strength steel. Note that $\varphi_{lim,Kim}$ is equivalent to 0.1 rad for the reference steel S235. The nominal ultimate-to-yield stress ratio of S235 steel can be approximated as 1.5 for simplicity. In this study, by combining the key ideas from the existing joint rotation limits (equations 2.5–2.7), a new deformation limit is proposed for plate-to-CHS joints under IPB (which will be explained later in Section 4.4).

$$\varphi_{lim,Kim} = 0.1\frac{\left(f_{u0}/f_{y0}\right)}{\left(f_u/f_y\right)_{S235}} = \frac{1}{15}\left(\frac{f_{u0}}{f_{y0}}\right) \text{ (rad)} \qquad (2.7)$$

2.2.3. High-strength steel plate-to-CHS joints

Despite increasing interest in high-strength steel tubular joints (Lee et al. (2017) and Lan et al. (2020)), only a limited number of studies have been conducted on high-strength steel plate-to-CHS joints. The high-strength steel considered in these rare studies mostly had a yield stress close to 460 MPa. It is noteworthy that prEN 1993-1-8 (CEN (2019) permits only up to 460 MPa for plate connections, whereas the yield stress limit is $f_y \leq 700$ MPa for the joints between tubular members. The more restrictive limit imposed on plate connections seems to reflect a lack of experimental evidence, higher detrimental stress concentration, and reduced ductility expected in plate connections.

Lee et al. (2012b) reported a rare high-strength steel study of plate joints. They conducted a testing program on compression-loaded longitudinal XP joints. A mild steel SS400 (with a nominal yield stress of 235 MPa) and high-strength steel HSB600 (with a nominal yield stress of 450 MPa) were used for the test specimens. Both the mild and high-strength steel joints failed owing to chord plastification, and their ultimate strength exceeded the ISO 14346 (ISO (2013)) chord plastification design resistance, even when a material factor of 0.9 was not applied for HSB600. As a continuing study, Lee et al. (2019) conducted supplemental FE analyses for the longitudinal XP joints in compression with nominal yield stresses of 460, 650, 900, and 1100 MPa, and suggested relevant material factors. The major criterion in determining the material factor was to minimize scatter in the prediction, and therefore, the material factor was separately proposed for each design formula considered (ISO 14346 and EN 1993-1 (CEN (2005, 2007)). In principle, the material factor should be evaluated based on a direct comparison of mild and high-strength steel joints in the same geometry (Liu and Wardenier (2004)). The material factor of 460 grade steel was not proposed for ISO 14346 and EN 1993-1 because these standards already included $C_f = 0.9$ for $f_y = 460$ MPa. For steel grades of 650, 900, and 1100 MPa, the proposed material factors were respectively 0.9, 0.75–0.8, and 0.62–0.67 (depending on the design formula). Lee et al. (2012a) also conducted IPB tests on longitudinal XP joints fabricated from SS400 and HSB600. In contrast to the axial load testing, their study showed that the ISO 14346 (ISO (2013)) design resistance formula generally overestimates the IPB strength of all SS400 and HSB600 joints.

2.2.4. Plate-to-CHS joints under combined loading

Regarding plate-to-CHS joints subjected to combined branch loading, only one relevant study (Lee et al. (2017)) was found in the author's literature survey. Lee et al. (2017) numerically investigated the ultimate behavior of longitudinal XP joints under combined axial compression and IPB. Steel grade HSB600 was considered. The chord preload and its effect on the joint behavior (i.e., the chord stress effect) were also included in the analysis. The linear interaction equation was found to be more appropriate for longitudinal XP joints than the more generous, convex-shaped interaction relationships, such as in equation 1.1. However, because the FE analysis only covered limited geometries (2γ = 20 or 29, η = 1 or 2), the linear interpolation equation needs to be further examined for a wider range of geometric parameters. It should also be noted that for CHS joints under IPB loading, unless the chord section is sufficiently slender (e.g., $2\gamma \geq 30$), a premature punching shear failure at the tension side of the joint is also possible before sufficient plastification in the chord face develops (Lee et al. (2021)). The numerical modeling of Lee et al. (2017) did not incorporate any rupture criterion, which might have led to inaccurate results because of possible chord punching shear failure.

Chapter 3. Experimental Program

The objective of the experimental program was to investigate the influence of high-strength steel on the behavior of X-type longitudinal plate-to-circular hollow section (CHS) joints. Most of representative design standards suggest to use steels with yield stress (f_{y0}) up to 460 MPa for plate-to-CHS joints due to the limited experimental data as well as concerns about the low ductility of high-strength steel. Especially, when the high-strength steel joint is subjected to tension load, the fracture failure usually causes the insufficient deformation capacity of the joint. The fracture failure mode is difficult to predict reliably through FE analysis. Thus, in this chapter, by conducting experiments for high-strength steel joints under tension or in-plane bending moment (IPB), the material effect on the deformation capacity and failure mode of the joint, and the applicability of the design formulae to high-strength steel joints are examined.

3.1. Geometric and material properties

3.1.1. Design of test specimens

A total of three X-type longitudinal plate-to-CHS joints (longitudinal XP joints) were tested: two specimens under axial tension load and the other one under IPB.

The configuration and definition of symbols for the specimens are shown in Figures 3.1–3.3. In the tension specimens, two grades of high-strength steel, SM460 (f_{yn} = 460 MPa) and ATOS80 (f_{yn} = 700 MPa), were applied on the chord. The key

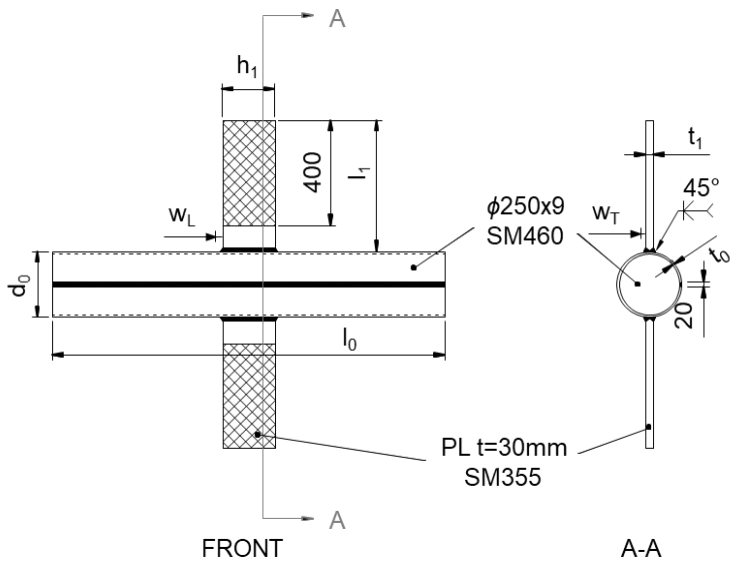

Figure 3.1. Configuration of C-XP2-T-460

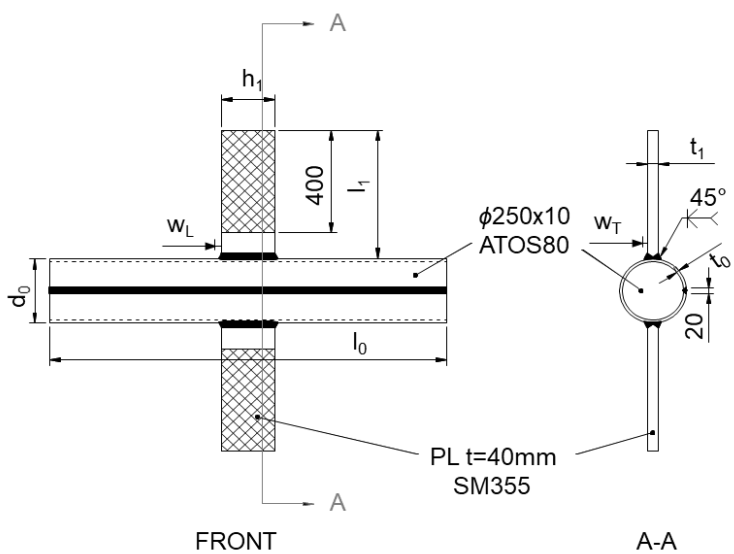

Figure 3.2. Configuration of C-XP2-T-700

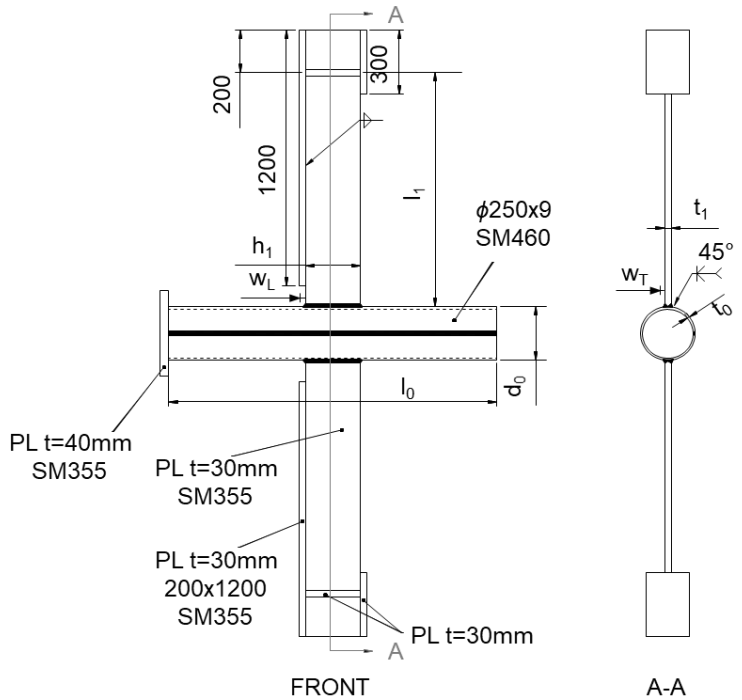

Figure 3.3. Configuration of C-XP2-I-460

parameters of plate depth-to-chord diameter ratio (η) was designed to 0.8 and a chord diameter-to-thickness ratio (2γ) was designed to 29.8 (SM460) or 25.0 (ATOS80). In the IPB specimen, steel grade of SM460 was chosen with η = 0.8 and 2γ = 29.8. For branch plates of all specimens, a mild steel SM355 (f_{yn} = 355 MPa) was used.

ATOS80 is a very high-strength steel designed for automobile structure, and has excellent cold formability by lower carbon content. ATOS80 was applied due to the difficulty in supply of high-strength steel with yield stress of 700 MPa for building structures, however, as will be shown in the stress-strain relationship in Section 3.2.2, it has comparable performance and characteristics to high-strength steel used in building structures.

The tension-loaded joints were designed to exhibit full chord plastification during the test, and the IPB joint was designed to observe chord punching shear

failure before sufficient plastification on the chord. The design of the test specimens will be dealt with in detail in Chapter 4.

The measured geometric properties and nondimensional parameters are summarized in Tables 3.1 and 3.2. Weld size of the joint were measured in the longitudinal direction (w_L) and the transverse direction (w_T). To exclude the influence of the chord length on the joint behavior, the effective chord length-to-radius ratio (α') was set to approximately 10. The thickness of the branch plates was designed to be thick enough to prevent plate yielding. For IPB specimen, the plate length (L_1) was sized to about $4h_1$ in order to minimize the effect of shear on the joints relative to the bending moment. To avoid plate local buckling due to the slender plate, the upper flange was added on the plate at a distance from the joint.

Table 3.1. Measured geometric properties

Specimen	Load type	d_0 (mm)	t_0 (mm)	h_1 (mm)	t_1 (mm)	w_L (mm)	w_T (mm)
C-XP2-T-460	Tension	249.0	9.4	197.5	30.3	20.0	12.4
C-XP2-T-700	Tension	252.2	9.9	199.0	40.0	15.3	11.0
C-XP2-I-460	IPB	249.5	9.4	249.0	30.0	18.0	14.0

Additional properties:
l_0 = 1500.0 mm (nominal) for all specimens, l_1 = 500.0 mm (nominal) for tension specimens, l_1 = 1100.3 mm for IPB specimen

Table 3.2. Steel grades and nondimensional geometric properties

Specimen	Load type	Steel grade	η	2γ	α'[a]
C-XP2-T-460	Tension	SM460	0.8	26.5	10.5
C-XP2-T-700	Tension	ATOS80	0.8	25.4	10.3
C-XP2-I-460	IPB	SM460	1.0	26.5	10.0

[a] Effective length parameter $\alpha' = 2(l_0-h_1)/d_0$

The CHS chord members were fabricated through press bending and connected with full penetration weld. Branch plates were partial penetration welded on both side of the chord face at 90° angle from the weld seam. For the seam welding of ATOS80 chords, a matching electrode with a tensile stress of 780 MPa was used. For SM460 steel, the electrode used for ATOS80 was also used because an appropriate matching electrode was unavailable. The electrode used for tube seaming was especially equivalent to American Welding Society E121T1-G (AWS (2010)). In welding the plate-to-CHS joints, a matching electrode SF71 was applied with a tensile stress of 490 MPa.

3.1.2. Coupon test results

The stress-strain curves of SM460 and ATOS80 was obtained through coupon tests. A total 18 coupons were tested which can be divided into three groups: three coupons cut from parental flat plate (flat coupon), three coupons cut from CHS chord (curved coupon), and three coupons groove-welded in the center of the flat coupon (W/D coupon) for each steel grade (see Figure 3.4). The curved coupons were obtained

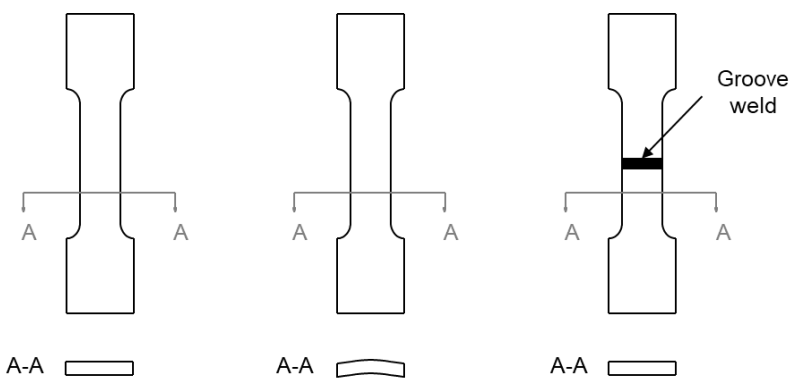

(a) Flat coupon (b) Curved coupon (c) W/D coupon

Figure 3.4. Configuration of coupons

from the remaining chord with diameter of 250 mm after manufacturing the specimens. Thickness of the coupons was equal to the chord of the test specimen (9 mm for SM460 and 10 mm for ATOS80). Changes in material properties due to cold-forming or welding process are investigated.

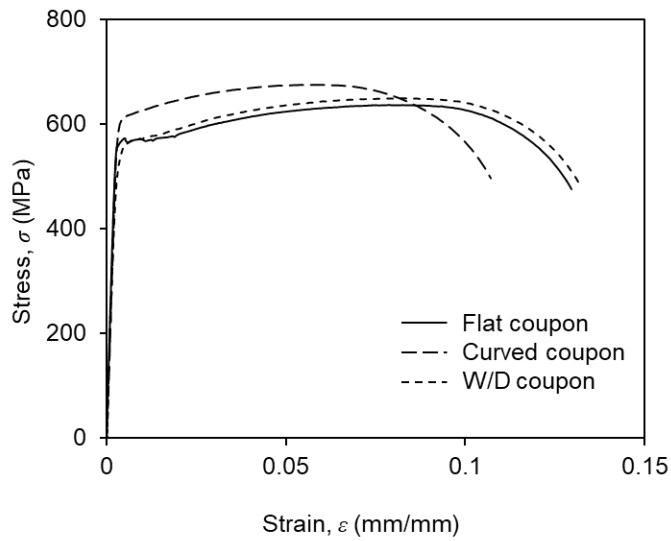

Figure 3.5. Stress-strain behavior of SM460

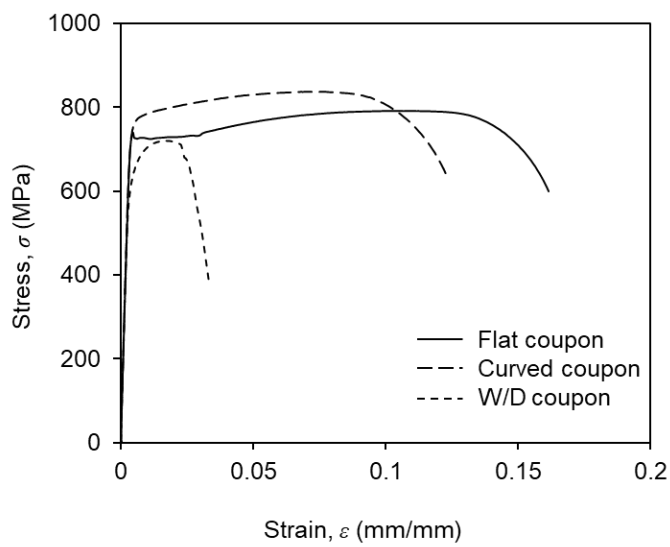

Figure 3.6. Stress-strain behavior of ATOS80

The representative stress-strain curves for each group of coupons are shown in Figures 3.5 (SM460) and 3.6 (ATOS80). The stress-strain curves of curved coupons for SM460 and ATOS80 have less strain-hardening region and slightly increased yield stress compared to that of flat coupons, resulting from cold-forming process. In W/D coupon tests, while SM460 has little change in properties, ATOS80 has a remarkable decrease in ultimate strain (ε_u) and reduced yield stress by about 10%, indicating that the heat affected zone would become highly brittle for steel grade ATOS80.

Figure 3.7 shows the test results of the curved coupons of SM460 and ATOS80 altogether with the stress-strain curve of SS275 (f_{yn} = 275 MPa) for comparison with mild steel. The SS275 curved coupon was extracted from a 15 mm-thick CHS with a diameter of 400 mm. The high-strength steels (SM460, ATOS80) have shorter strain-hardening region relative to mild steel (SS275). While the yield ratio (f_y/f_u) of the mild steel SS275 is 0.72, it is 0.91 for both high-strength steels SM460 and

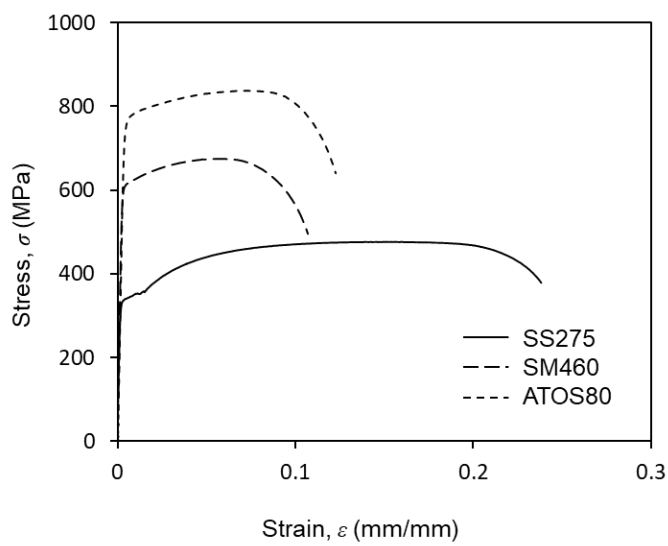

Figure 3.7. Comparison of stress-strain behavior depending on steel grades

Table 3.3. Average measured material properties

Coupon	E (GPa)	f_y (MPa)[a]	f_u (MPa)	ε_u (%)	Yield ratio
SM460-T9-flat	220.5	572.5	640.2	6.9	0.89
SM460-T9-curved	220.5	609.0	672.1	5.4	0.91
SM460-T9-W/D	218.3	562.4	649.5	8.4	0.87
ATOS80-T10-flat	206.5	719.5	786.6	10.7	0.91
ATOS80-T10-curved	218.9	761.5	834.2	7.4	0.91
ATOS80-T10-W/D	195.1	647.0	719.7	1.7	0.90

Nominal yield stress and tensile stress:
f_{yn} = 460 MPa, f_{un} = 570 MPa for SM460
f_{yn} = 700 MPa, f_{un} = 780 MPa for ATOS80

[a] Yield stress calculated by 0.2% offset method

(a) SM460

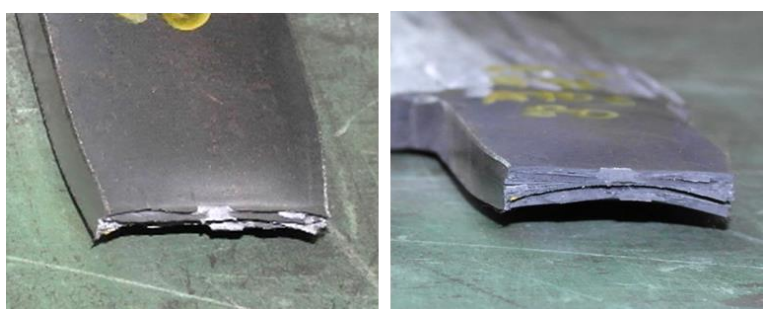

(b) ATOS80

Figure 3.8. Fracture surface of curved coupons

ATOS80. Although the yield stress of ATOS80 is 25% higher than SM460, the deformation capacity of the material is comparable. In Table 3.3, the average measured material properties of SM460 and ATOS80 obtained from the stress-strain diagrams are summarized. The effect of these material properties on longitudinal XP joints is analyzed through experiments.

The fracture surface of the tested coupons is shown in Figure 3.8. For ATOS80, layers were observed on the fracture surface unlike SM460. This may be one of the properties of ATOS80 induced by the manufacturing process.

3.2. Test setup

The tension test for longitudinal XP joints was conducted using 3,000 kN universal testing machine (UTM), and the IPB test was carried out using 10,000 kN UTM. The tension-loaded joints were tested in the configuration shown in Figure 3.9. The upper and lower branch plates of the specimen were clamped with hydraulic grips.

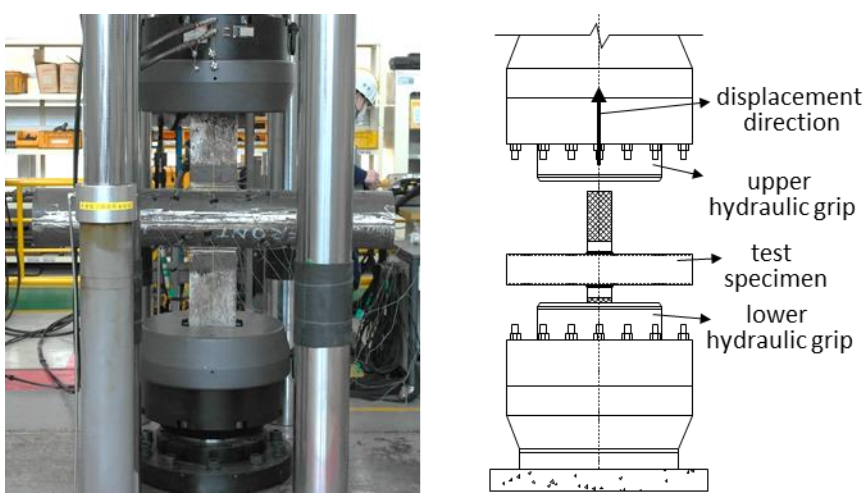

Figure 3.9. Test setup for tension-loaded longitudinal XP joints

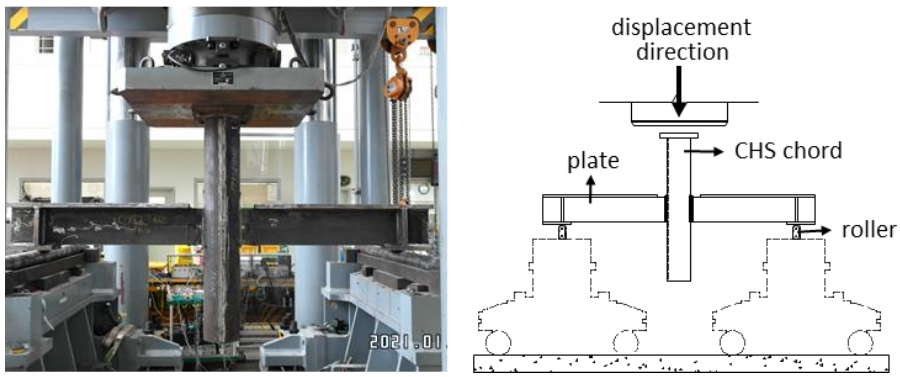

Figure 3.10. Test setup for IPB-loaded longitudinal XP joint

Displacement was applied to the upper branch plate. The test setup for IPB joint is given in Figure 3.10. The plates were supported with rollers, and downward displacement was applied to the chord to induce in-plane bending moment on the joint.

The arrangement of linear variable differential transformers (LVDTs) and strain gauges is shown in Figures 3.11 and 3.12. For tension specimens, the relative vertical distance between points A and B was measured using LVDTs, and the joint deformation was assumed as half of the relative distance (see Figure 3.11(a)). For

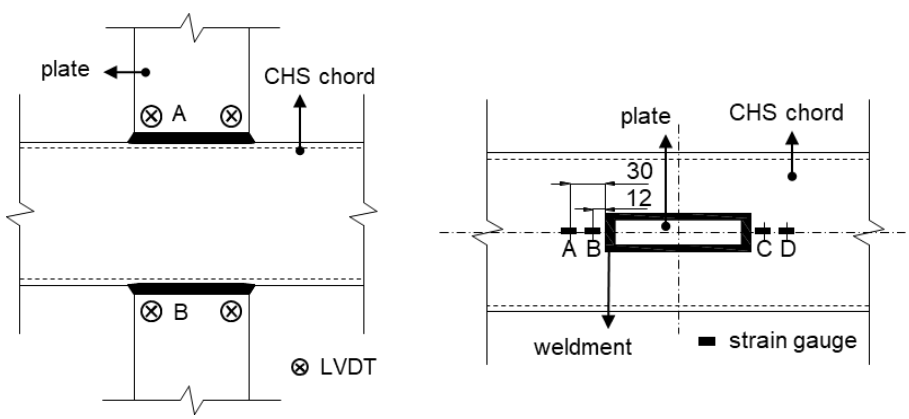

(a) LVDT arrangement (b) Strain gauges arrangement

Figure 3.11. Instrument arrangement for tension-loaded XP joints

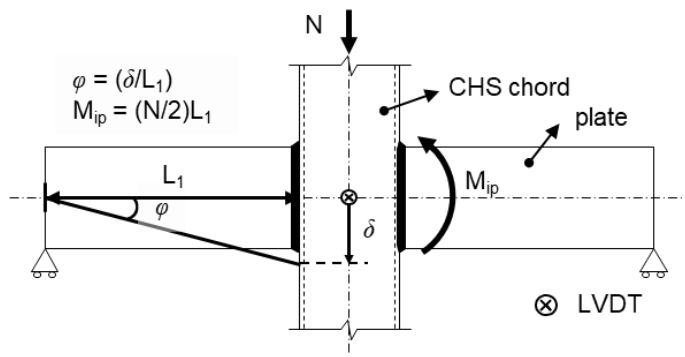

(a) LVDT arrangement and definition of joint rotation

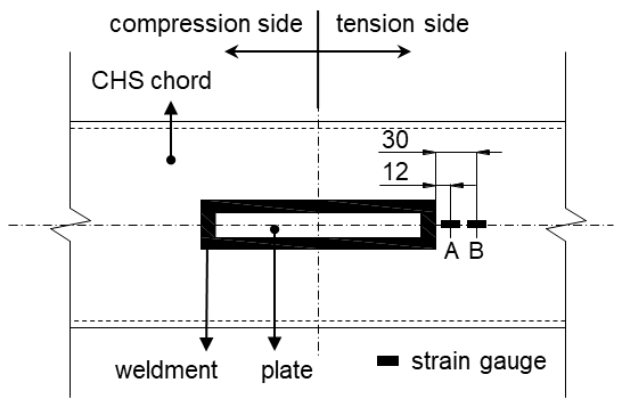

(b) Strain gauges arrangement

Figure 3.12. Instrument arrangement for IPB-loaded XP joint

IPB specimen, displacement of chord (δ) was measured and joint rotation was defined as δ divided by plate length (L_1), as shown in Figure 3.12(a). In addition, strain gauges were attached to the chord face to investigate the magnitude of plastic strain near the joint in order to assume the maximum strain at the weld toe. The strain at weld toe can be obtained by linearly extrapolating the measurements of strain gauges A (or C) and B (or D) in the Figures 3.11(b) and 3.12(b).

3.3. Test results and its evaluation

In evaluation of test results, the material properties of curved coupons had been used since the influence of welding should be reflected in the material factor. According to prEN 1993-1-8 (CEN (2019)) and ISO 14346 (ISO (2013)), steel grades SM460 (f_{y0} = 609.0 MPa) and ATOS80 (f_{y0} = 761.5 MPa) could not be applied to plate-to-CHS joints, exceeding the applicable range of yield stress ($f_{y0} \leq 460$ MPa). Further, the measured yield ratio of SM460 and ATOS80 were both 0.91, indicating that the yield stress of the material must be limited to $0.80f_{u0}$. In this section, the effect of the high-strength steel on the joint behavior (i.e. strength, deformation capacity, and failure mode) was firstly examined, and the possibility of relaxing the restriction to high-strength steel presented by provisions was also investigated. The joint strength was evaluated based on prEN 1993-1-8, which reflected the latest research on the plate-to-CHS joints.

Although the number and range of the test specimens is quite limited, it can provide general understanding of the behavior and failure mode for plate-to-CHS joints with high-strength steel. The test results were also compared to experimental database of plate-to-CHS joints under tension load or IPB from other authors.

3.3.1. Joints under branch plate tension

i. C-XP2-T-460

The tension-loaded longitudinal XP joints with SM460 (C-XP2-T-460) exhibited chord punching shear failure followed by sufficient plastification of the chord (see Figure 3.13). In Figure 3.14, the load-deformation relationship is illustrated with 3%d0 deformation limit. The joint underwent a larger deformation up to 20%d0.

(a) Overall deformed shape

(b) Chord punching shear failure

Figure 3.13. Failure of C-XP2-T-460

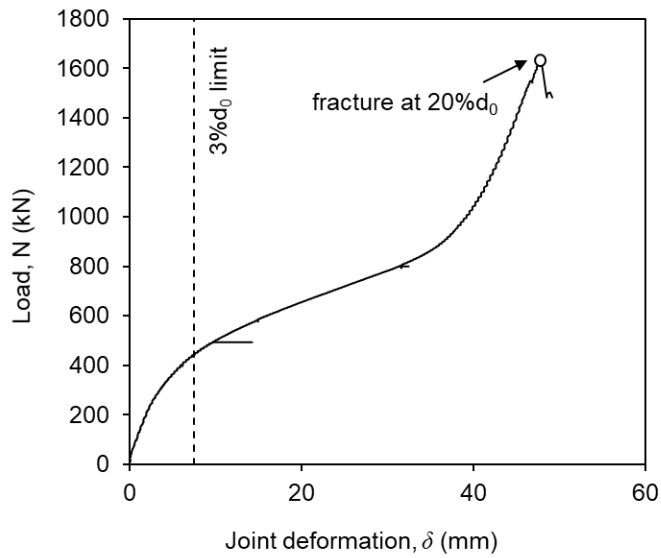

Figure 3.14. Load-deformation relationship of C-XP2-T-460

The measurements of the strain gauges according to the position of the chord face are shown in Figure 3.15, setting the plate centerline to 0 (mm). The strain at the weld toe was linearly extrapolated with the two measurements of strain gauges C and D (see Figure 3.11(b)). The strain gradually increased as the joint displacement increased. The strain concentration of the joint was very large at the weld toe. The maximum plastic strain just before joint failure was about 10%.

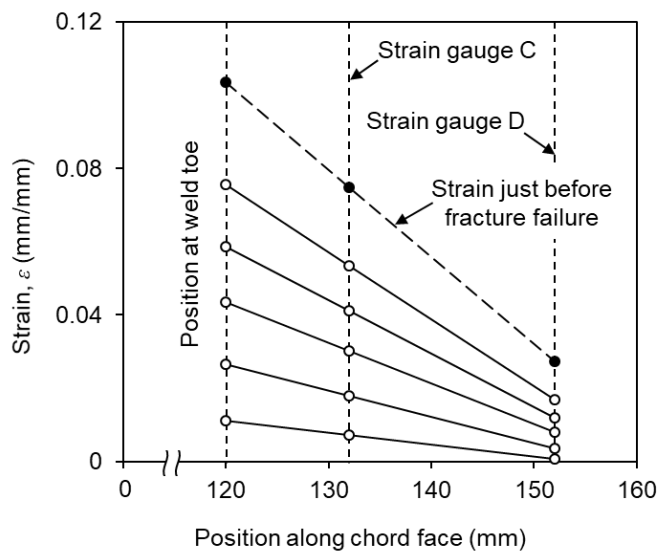

Figure 3.15. Strain distribution of C-XP2-T-460

ii. C-XP2-T-700

The tension-loaded longitudinal XP joint with ATOS80 (C-XP2-T-700) experienced through-thickness fracture of the chord rather than chord punching shear (see Figure 3.16). Compared to C-XP2-T-460 specimen, the deformation of the joint is not visually pronounced. The through-thickness failure of the joint may be related to the layered structure of ATOS80 observed from the coupon test (see Figure 3.8(b)).

(a) Overall deformed shape

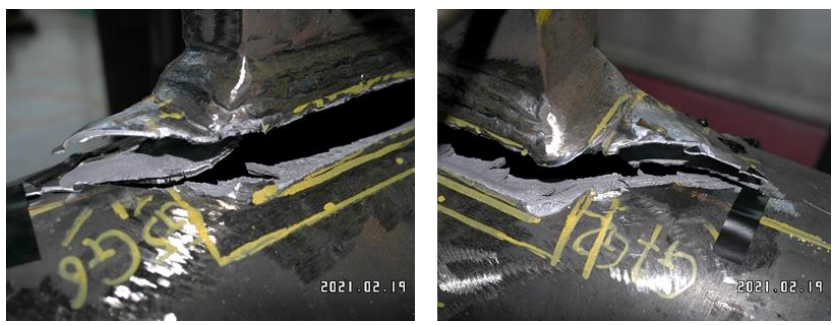

(b) Though-thickness fracture

(c) Fracture surface

Figure 3.16. Failure of C-XP2-T-700

In the load-deformation curve of the joint shown in Figure 3.17, contrary to C-XP2-T-460, the deformation capacity was significantly decreased and fracture occurred before regaining of the joint stiffness. Nonetheless, the joint still showed a sufficient deformation (11%d_0) after reaching the 3%d_0 deformation limit.

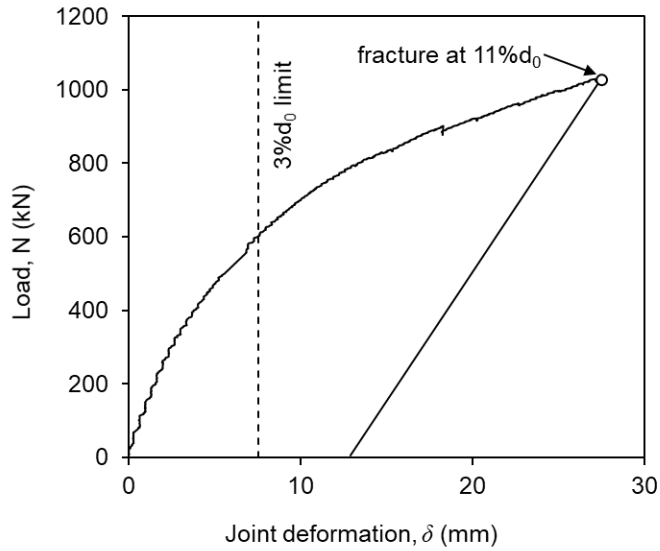

Figure 3.17. Load-deformation relationship of C-XP2-T-700

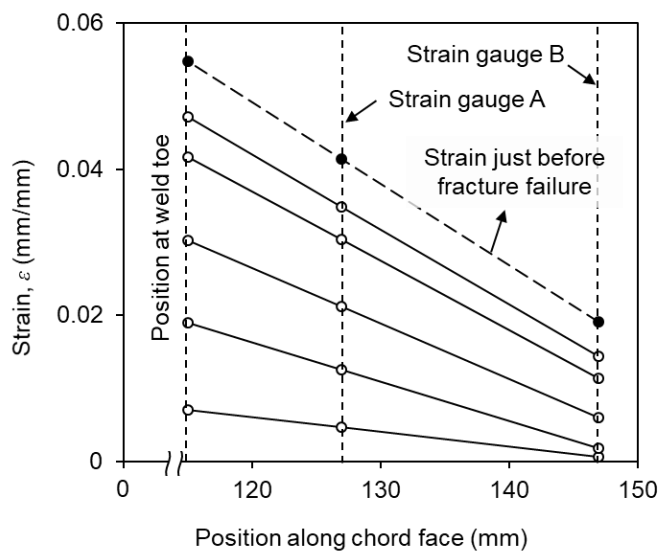

Figure 3.18. Strain distribution of C-XP2-T-700

The measured strain at the chord face is plotted gradually according to the deformation of the joint (see Figure 3.18). The strain at weld toe was linearly extrapolated by the measurements of strain gauges A and B (see Figure 3.11(b)). The

strain at the weld toe of the joint just before the fracture was about 4.4%, which is reduced by 45% compared to the C-XP2-T-460 specimen. Although the strain-hardening performance of ATOS80 was comparable to that of SM460, the joint behavior was apparently brittle, probably due to the occurrence of through-thickness fracture or the more significant material change in the heat affected zone (see Figures 3.5 and 3.6).

iii. Evaluation of test results with available test database

The load-deformation curves of C-XP2-T-460 and C-XP2-T-700 are plotted in Figure 3.19. The joint load was normalized by $f_{y0}t_0^2$ for a consistent comparison between the joints with different material yield stresses. The yield stresses of the chord (f_{y0}) are those from curved coupons. Until fracture, the ATOS80 joint exhibited equivalent performance to SM460 joint. The two curves are almost identical except for the deformation capacity. The material brittleness in this study appears to have

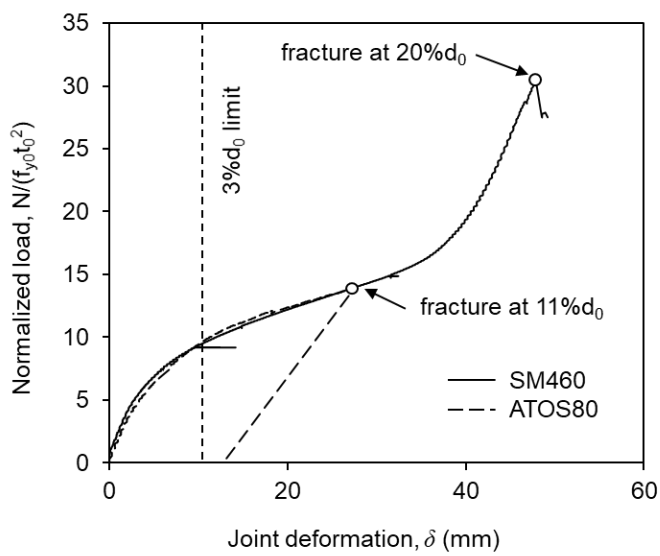

Figure 3.19. Normalized load-deformation relationship of C-XP2-T-460 and C-XP2-T-700

greater influence on deformation capacity at larger deformation rather than the ultimate strength of the joint as determined at 3%d_0. When observed based on the deformation limit at which the joints strength is determined, both high-strength steel joints exhibited sufficient deformation capacity.

Table 3.4 summarizes tension test results. Both specimens did not present clear peak load and the joint strengths (N_u) were determined at the 3% limit. The joint strength is compared with chord plastification and chord punching shear design resistance suggested by prEN 1993-1-8 (CEN (2019)) ($N_{prEN,CP}$ and $N_{prEN,PS}$, respectively). Since the joint strengths are lower than chord punching shear design resistance and sufficient chord plastification has been exhibited during the tests, the ultimate limit state of the joints appears more relevant to chord plastification. In calculating the design resistance, the measured yield stress and tensile stress of curved coupons were utilized (see Table 3.3). The design resistance was calculated in two ways: design resistance with or without material factor (C_f) and the yield stress limitation of $f_y \leq 0.8f_u$. According to prEN 1993-1-8, the steel grades SM460 (f_{y0} = 609.0 MPa) and ATOS80 (f_{y0} = 761.5 MPa) could not be applied to plate-to-CHS

Table 3.4. Test result summary for tension-loaded joints

Specimen	f_y (MPa)	N_{Peak} (kN)	$N_{3\%}$ (kN)	$N_{prEN,CP}$ (kN)	$N_{prEN,PS}$ (kN)	N_u/N_{prEN} [a]
C-XP2-T-460	609.0	-	443.7	311.2 [b] (247.3) [c]	1310.2 [b] (1040.2) [c]	1.43 [b] (1.79) [c]
C-XP2-T-700	761.5	-	603.0	434.7 [b] (342.9) [c]	1745.5 [b] (1376.8) [c]	1.39 [b] (1.76) [c]

[a] N_u: preceding load among the peak load or the load corresponding to ultimate deformation limit ($N_u = N_{3\%}$)
[a] N_{prEN}: design resistance of corresponding to the ultimate limit state of the joint ($N_{prEN} = N_{prEN,CP}$ for both specimens)
[b] Design resistance excluding $C_f = 0.9$ or $f_y \leq 0.8f_u$
[c] Design resistance including $C_f = 0.9$ and $f_y \leq 0.8f_u$

joints. Nonetheless, for research purpose, the material factor C_f = 0.9 proposed for the plate-to-CHS joints with 355 < f_y ≤ 460 MPa was extended arbitrarily to both specimens. The yield stress was lowered to 0.8f_{u0} since the yield ratio of SM460 and ATOS80 was 0.91.

The normalized strengths (N_u/N_{prEN}) of C-XP2-T-460 and C-XP2-T-700 show that the joints have safety margins of 1.43 and 1.39, respectively, when excluding the material-related reductions. As shown in Figure 3.19, though ATOS80 is a very high-strength steel, the joints of two steel grades showed similar performance at 3% limit. Thus, the normalized joint strength of ATOS80 joint hardly decreased unexpectedly. The safety margins significantly increase to 1.79 and 1.76, respectively, when the design resistance is reduced by C_f = 0.9 and f_{y0} = 0.8f_{u0}. In the evaluation of prEN 1993-1-8 design formulae for plate-to-CHS joints by Wardenier et al. (2018), compression-loaded longitudinal XP joints had an average strength of 1.59 times the design resistance. Besides, tension-loaded longitudinal XP joints had an average strength of 1.22 times the joint strength under compression load. That is, the tension joints can be estimated as having an average safety margin of 1.94 for design formula. The yield stress of joints used in the evaluation was 389 MPa. Therefore, it is slightly insufficient to provide a uniform safety margin with the evaluated data when using C_f = 0.9 and f_{y0} = 0.8f_{u0} for the tension-loaded XP joints of the specimens C-XP2-T460 and C-XP2-T-700, which gives safety margin of 1.79 and 1.76.

Further investigation on the experimental results was carried out with a supplemental test database of longitudinal XP joints under tension load from Voth (2010), Makino (1984), Togo (1967), and Akiyama et al. (1974), which are provided by Voth (2010). Figure 3.20 shows the strength distribution of the joints obtained from the test results including the available experimental database. The joint strength

is normalized by design resistance per prEN 1993-1-8 and was plotted against the measured yield stress (f_{y0}). In preparing Figure 3.20, the material factor or yield stress-related reduction ($f_y \leq 0.80 f_u$) was not applied. All of the joint strengths were determined based on the 3%d_0 deformation limit criterion.

As shown in Figure 3.20, the normalized joint strength of Akiyama et al. (1974) overestimates the prEN 1993-1-8 design resistance, and the joint strength of Voth (2010) greatly underestimates the design resistance. The data of Akiyama et al. (1974) were outside of the applicable range of nondimensional geometric properties per prEN 1993-1-8, having η range of 0.3–1.0 and 2γ range of 70.8–93.3. For the data of Voth (2010), the chord length was very short (α' = 5.1), and the deformation of the chord ends was restrained by the end plates. Accordingly, the joints may become stiff than not restrained. Thus, the data of Akiyama (1974) and Voth (2010) can be treated as outlier.

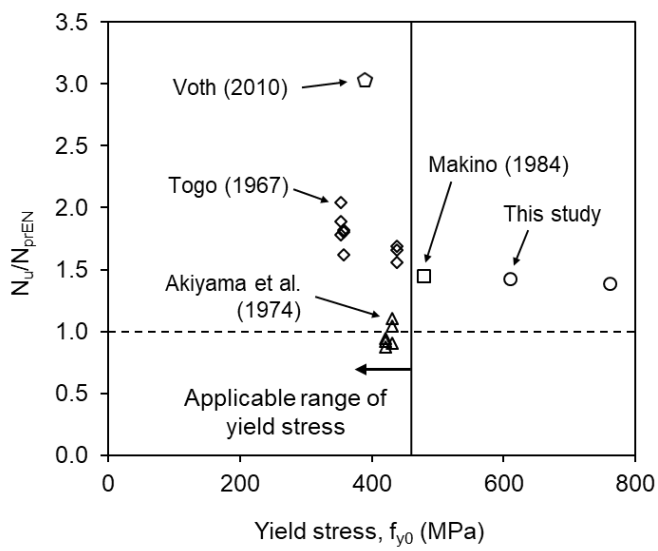

Figure 3.20. Evaluation of prEN 1993-1-8 design resistance for tension-loaded joints (material factor not included)

Compared to the data of Togo (1967) and Makino (1984), which belong to the mild steel joints, the normalized strength of high-strength steel joints in this study is slightly reduced, but still comparable. Some acceptable material factor would provide uniform safety margin with mild steel joints. Considering the sufficient deformation capacity of the tested joints in this study, the structural performance is not far beyond to mild steel joints. Consequently, the possibility of extending the design formula to high strength steel whose yield stress is up to 700 MPa is suggested. It should be noted that further experiments are necessary for a proposal of the specific material factor for tension-loaded plate-to-CHS joints with high-strength steel of higher than 460 MPa.

3.3.2. Joints under branch plate IPB

i. C-XP2-I-460

Figure 3.21 illustrates the failed configuration of the longitudinal XP joint with SM460 tested under IPB (C-XP2-I-460). The failure mode of chord punching shear was exhibited. Though it was shown visibly that the deformation of the joint is greater on the compression side than on the tension side, the fracture occurred on the tension side, indicating significantly lower deformation capacity under tension load. In Figure 3.22, the moment-rotation relationship is plotted with a newly proposed deformation limit on the joint rotation angle, which will be explained in detail later in Chapter 4. Although the fracture was initiated at around 0.15 rad, the joint underwent further rotation, which could be credited to the stiffness at the compression side. However, the rotation capacity after the fracture is not reliable, so it was excluded in the evaluation of the joint rotational capacity. The fracture began at approximately twice the rotation at the peak or deformation limit.

(a) Overall deformed shape

(b) Chord punching shear failure

Figure 3.21. Failure of C-XP2-I-460

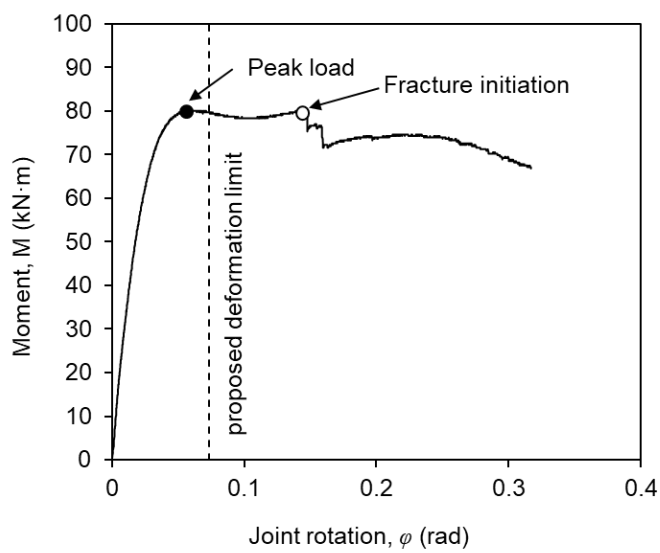

Figure 3.22. Moment-rotation relationship of C-XP2-I-460

Figure 3.23 depicts the measurements of tension side strain gauges A and B (see Figure 3.12(b)) including the extrapolated strain at weld toe. The maximum plastic strain level at weld toe was around 3%.

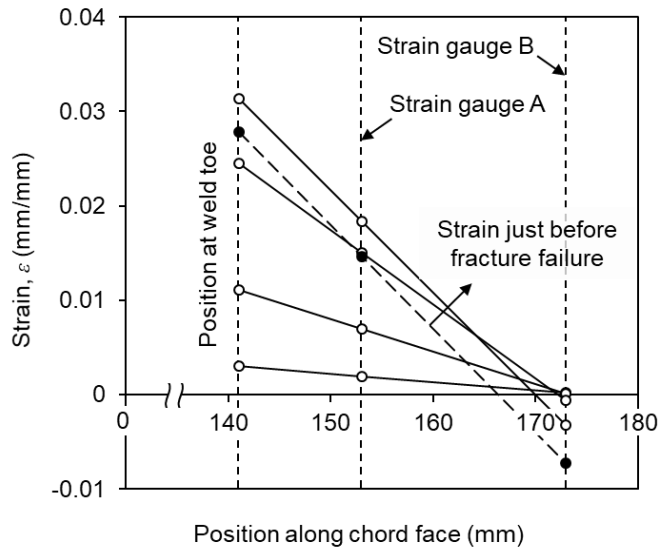

Figure 3.23. Strain distribution of C-XP2-I-460

ii. Evaluation of test result with available test database

The IPB test results are summarized in Table 3.5. Since the peak load preceded the load at deformation limit, the joint strength (M_u) was determined at peak. The joint strength is compared with chord plastification and chord punching shear design resistance suggested by prEN 1993-1-8 (CEN (2019)) ($M_{prEN,CP}$ and $M_{prEN,PS}$, respectively). Both the chord plastification and chord punching shear design resistance are less than the joint strength. However, in the test, the joint showed sufficient rotational capacity until the fracture. Therefore, the joint behavior was considered as being governed by chord plastification. The joint strength is normalized by the chord plastification design resistance, with applying C_f = 0.9 and

Table 3.5. Test result summary for IPB-loaded joint

Specimen	f_y (MPa)	M_{Peak} (kN·m)	$M_{proposed}$ (kN·m)	$M_{prEN,CP}$ (kN·m)	$M_{prEN,PS}$ (kN·m)	M_u/M_{prEN} [a]
C-XP2-I-460	609.0	80.0	79.7	57.3 [b] (45.5) [c]	68.5 [b] (54.4) [c]	1.40 [b] (1.76) [c]

[a] M_u: preceding load among the peak load or the load corresponding to ultimate deformation limit ($M_u = M_{peak}$)
[a] M_{prEN}: design resistance corresponding to the ultimate limit state of the joint ($M_{prEN} = M_{prEN,CP}$)
[b] Design resistance excluding $C_f = 0.9$ or $f_y \leq 0.8f_u$
[c] Design resistance including $C_f = 0.9$ and $f_y \leq 0.8f_u$

$f_{y0} \leq 0.80f_{u0}$. Because the compressive load acting on the chord inducing IPB on the joint, the chord stress function (Q_f) is also included in the design resistance calculation; nonetheless, the chord stress effect was negligible.

The strength ratio of the joint is 1.40 when the material factor and yield ratio limitation are not included and it is 1.76 when including the material-related reductions in design resistance. Despite the high yield stress of 609 MPa, the design formula could evaluate the ultimate joint strength with a sufficient safety margin even without the material factor or yield ratio limitation.

Figure 3.24 shows the normalized joint strength (M_u/M_{prEN}) in this study with available experimental database for longitudinal XP joints under IPB from Lee et al. (2012a) and Makino et al. (1994). In calculating the design resistance, the material factor was not included. The measured yield stress and tensile stress were utilized. As the moment-rotation relationship was available for all experiments, the joint strength was obtained based on the proposed deformation limit criterion (see Section 4.4.1). The experiment setups reported were all similar in a way that induces IPB at the joint by the reaction force or applied load at the end of the plate.

In Figure 3.24, the normalized strength of the joint in this study is comparable to that of mild steel joint. Even the joint in this study shows slightly higher

normalized strength compared to the joint with yield stress of 478 MPa from Lee et al. (2012a) despite a significant difference in yield stress. It should also be noted that the geometric properties of the joint from Lee et al. (η = 1.0, 2γ = 29.2) was similar to the joint in this study. The applicable range on yield stress according to the prEN 1993-1-8 may be relaxed to higher strength steel considering the strength and rotation capacity of the high-strength steel joint if use appropriately suggested material-related reduction in design resistance. However, as in the tension-loaded joints, additional experiments or FE analyses are indeed required in order to suggest a specific material factor.

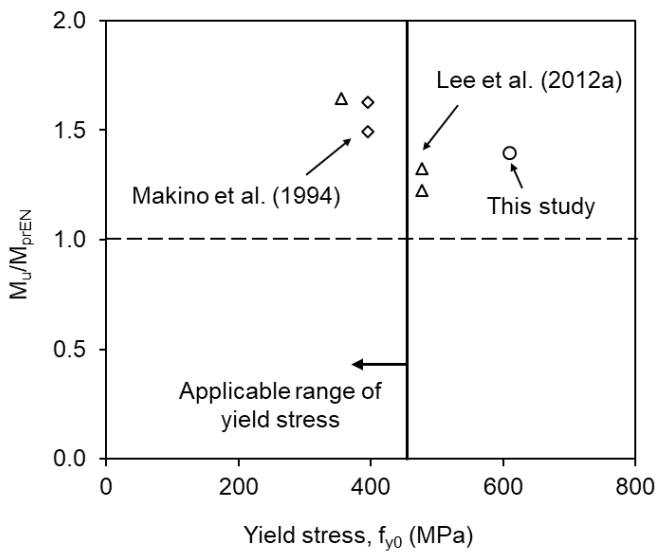

Figure 3.24. Evaluation of prEN 1993-1-8 design resistance for IPB-loaded joints (material factor not included)

The experimental program was conducted with Seon-Hu Kim, I-Hyun Ryu, Whi-Chan Chung, Si-Hyeong Park, and Chan-Ho Suk.

Chapter 4. Parametric Study

The experimental studies in Chapter 3 provided general understanding of the material effect and failure mode for longitudinal X-type plate-to-circular hollow section (CHS) joints with very high-strength steel. In this chapter, the numerical parametric analysis for plate-to-CHS joints in various loading type with wide range of geometric configurations was conducted to evaluate the prEN 1993-1-8 (CEN (2019)) design formulae including material factor.

For plate-to-CHS joints, representative design standards such as prEN 1993-1-8 and ISO 14346 (ISO (2013)) are suggested to use steel whose yield stress is up to 460 MPa, and apply material factor 0.9 when the yield stress is between $355 < f_y \leq 460$ MPa. The material limitation is related to low material-level ductility of high-strength steel. However, with the limited studies on plate-to-CHS joints with high-strength steel, the mechanical background behind the limitation is not clear. In addition, most of design standards do not clearly suggest the interaction equation for plate-to-CHS joints, though the axial load and bending moment often act simultaneously. Therefore, it is necessary to establish the basis of limitations on high-strength steel and an interaction relationship of combined load for plate-to-CHS joints. The FE analysis was performed on the longitudinal X- and T-type plate-to-CHS joints (longitudinal XP and TP joints, respectively), and the research issues were as follows:

i. When axial compression load or IPB acts on the plate-to-CHS joints with high-strength and mild steel, the design formulae and material factor according to prEN 1993-1-8 (CEN (2019)) were evaluated with FE results in this study and available experimental database.

ii. For the plate welded tubular joints under IPB or combined load, there is no appropriately suggested deformation limit criterion. Therefore, the widely used 3%d_0 deformation limit criterion was assessed and a new deformation limit criterion was defined, which can also be applicable to high-strength steel joints.

iii. The FE analysis for the plate-to-CHS joints under combined axial compression and IPB was carried out using proposed deformation limit criterion. The FE results were compared with the interaction equation for CHS-to-CHS joints provided by prEN 1993-1-8 and ISO 14346 (ISO (2013)), as will be shown in equation 4.12, and a new interaction equation for plate-to-CHS joints was proposed.

4.1. Finite element modeling

4.1.1. Joints modeling details

The configurations and definition of symbols for longitudinal XP and TP joints are plotted in Figure 4.1. A nonlinear FE analysis for longitudinal XP and TP joints was conducted using the general-purpose FE analysis software ABAQUS (Simulia (2014)) using a validated modeling technique for tubular joints used by Kim and Lee (2018). The modeling technique has been successfully applied for the FE analysis of CHS-to-CHS X- (Kim and Lee (2020)) and T-joints (Kim and Lee (2021)). The plate-to-CHS joint models were constructed using a 20-node solid element (C3D20R

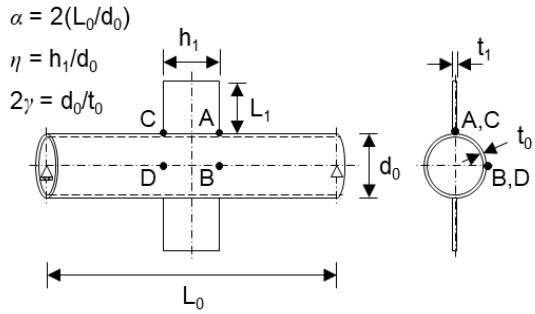

(a) Longitudinal XP joint

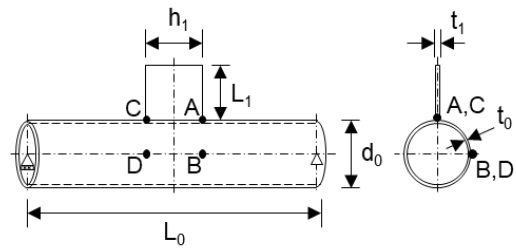

(b) Longitudinal TP joint

Figure 4.1. Geometric configurations and definition of symbols for longitudinal plate-to-CHS joint

in ABAQUS). The Riks method was employed for the numerical solver. The steel material was assumed to follow the von Mises yield criterion with isotropic hardening. The material properties of the weldment were assumed to be those of the base metal. Considering the symmetry in the geometry and loading, one quarter (XP joints) or half (TP joints) of a joint was modeled (see Figure 4.2). Finer meshes were applied within the vicinity of the joints, wherein large deformations and stress concentrations occur.

Numerical models for the parametric study of the longitudinal XP and TP joints were created within the selected geometric parameters, which will be discussed in Section 4.2.1. For the XP joints, a chord length-to-radius ratio (α) of 20 was chosen to exclude the effect of the chord length on the joint behavior. For the

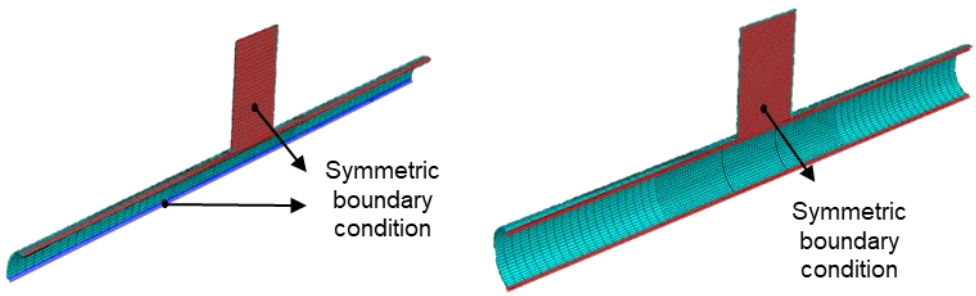

(a) XP joint (one quarter model) (b) TP joint (half model)

Figure 4.2. FE analysis models

TP joints, the saturated chord length was achieved by setting the effective chord length-to-radius ratio ($\alpha' = 2(L_0\text{-}h_1)/d_0$) to 20. The branch plate length (L_1) is sized larger than $1.5h_1$ to minimize the effect of shear on the joints relative to the bending moment. Groove welding was modeled as shown in Figure 4.3. The weld size of the FE models was designed to have prequalified minimum weld size suggested by AWS (2010). Displacement-controlled loading at the end of the branch plate was applied to the joints under pure axial compression or pure IPB. For the joints subjected to combined axial load and IPB, force-controlled loading was applied to maintain a fixed ratio between the magnitudes of the axial load and IPB during each step of the analysis.

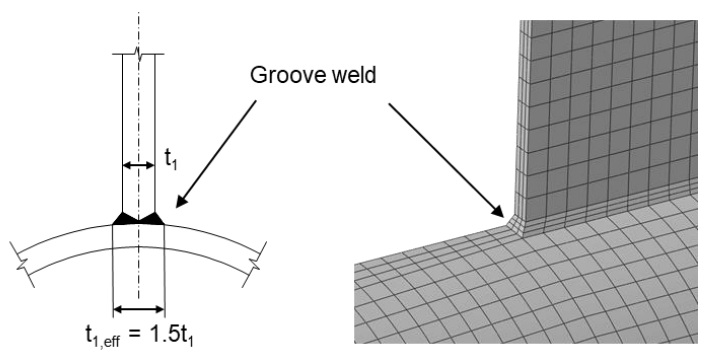

Figure 4.3. Detail and modeling of groove weld

The chord ends were modeled as simply supported. For simply supported TP joints under an axial load, chord bending is induced as a result of static equilibrium (see Figure 4.4(a)). To suppress the equilibrium-induced bending moment in the chord section at the joint, counter-active external bending moments were applied to both chord ends, as illustrated in Figure 4.4(a). When the compensating bending moments became larger than the plastic moment capacity of the chord (M_{p0}), a cross-sectional failure near the chord ends was avoided by properly increasing the yield stress of the end parts of the chord. For TP joints under IPB, because completely compensating for the chord stress effect by applying end moments or other means is infeasible, no compensation was attempted (see Figure 4.4(b)). Thus, the TP joint strength under IPB is expected to be slightly influenced by the chord stress effect.

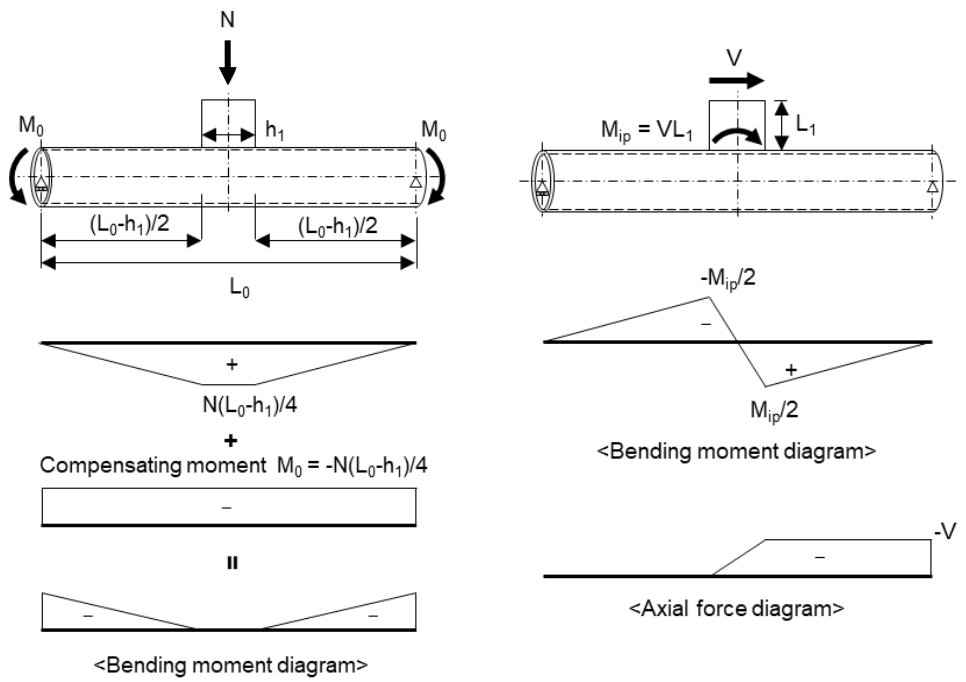

(a) Internal force diagram under compression

(b) Internal force diagram under IPB

Figure 4.4. Internal force distribution of TP joint under compression and IPB

4.1.2. Validation of modeling technique

To validate the accuracy of the FE modeling technique used, the experimental load-deformation relationships of longitudinal XP joints under axial tension and IPB in Chapter 3 were reproduced. Validation models for longitudinal XP joints were constructed based on the measured geometric properties (see Table 3.1). To investigate the influence of material properties on FE results, the measured stress-strain curves of curved coupons and W/D coupons were applied (see Table 3.3).

Figures 4.5 through 4.7 show a comparison between the FE analysis and test results. In the Figures, the load-deformation curve that exceeds the most among the dotted lines is the FE result of the initial model assuming that the reinforced weld is distributed constantly with the measured weld size (w_L and w_T in Table 3.1), as shown in Figure 4.8(c). However, in the FE results, the joint strength was very sensitive to the weld size, and therefore, the FE models were constructed in three configurations: without any reinforced weld (i.e. full penetration weld, see Figure 4.8(a)), with

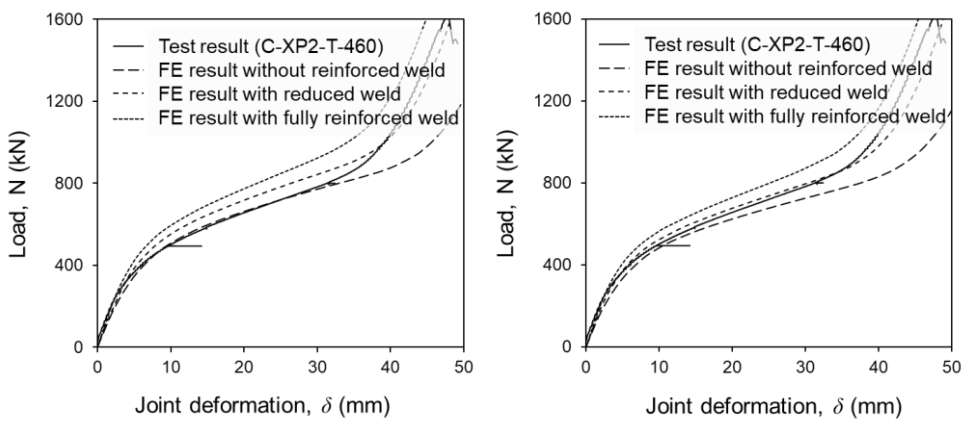

(a) FE models with material properties of curved coupons

(b) FE models with material properties of W/D coupons

Figure 4.5. Validation of FE modeling (C-XP2-T-460)

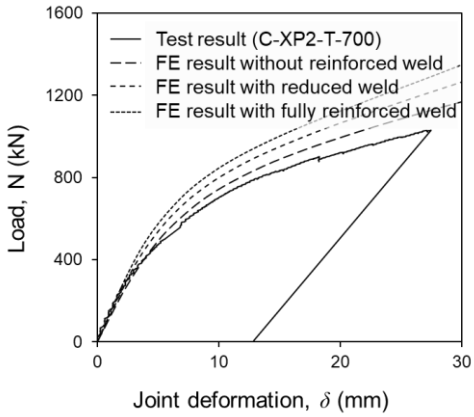

(a) FE models with material properties of curved coupons

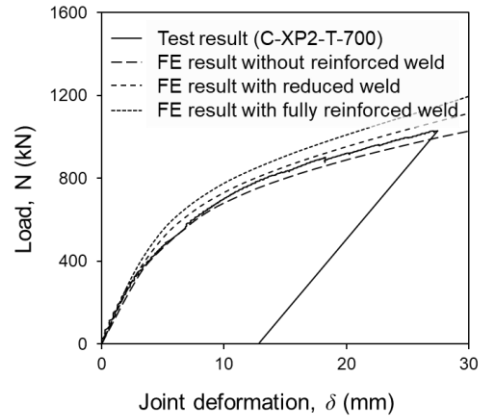

(b) FE models with material properties of W/D coupons

Figure 4.6. Validation of FE modeling (C-XP2-T-700)

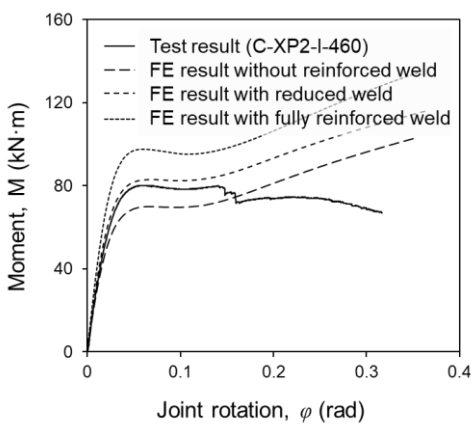

(a) FE models with material properties of curved coupons

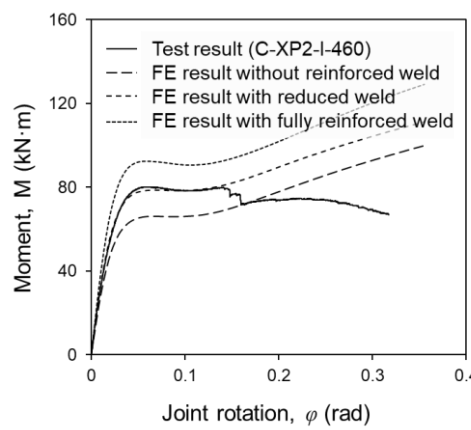

(b) FE models with material properties of W/D coupons

Figure 4.7. Validation of FE modeling (C-XP2-I-460)

reduced reinforced weld idealized similar to test specimen (see Figure 4.8(b)), and with fully reinforced weld (see Figure 4.8 (c)). In the reduced reinforced weld model, the maximum weld size was set to the measured weld size. Table 4.1 summarizes the

joint strength obtained from FE analysis and test results, and errors of the joint strength of the FE results compared to test result.

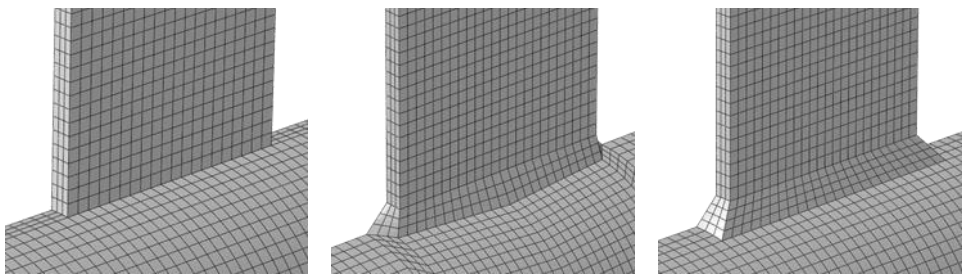

(a) Without reinforced weld (b) With reduced reinforced weld (c) With fully reinforced weld

Figure 4.8. Weld detail for FE modeling

Table 4.1. Results of FE modeling studies on material and weld size

Specimen		C-XP2-T-460		C-XP2-T-700		C-XP2-I-460	
		N_u [a] (kN)	Error [c] (%)	N_u [a] (kN)	Error [c] (%)	M_u [b] (kN·m)	Error [c] (%)
Test results		443.7	-	603.0	-	80.0	-
Without reinforced weld (FE)	Curve	439.5	1.0	636.0	5.5	70.0	12.5
	W/D	421.9	4.9	586.0	2.8	66.2	17.3
Reduced reinforced weld (FE)	Curve	480.1	8.2	688.9	14.3	83.0	3.8
	W/D	460.8	3.9	641.1	6.3	78.5	1.9
Full reinforced weld (FE)	Curve	523.8	18.0	731.4	21.3	97.6	22.0
	W/D	500.8	12.9	679.4	12.7	92.4	15.5

[a] The joint strengths are all determined at 3%d_0 deformation limit
[b] The joint strengths are all determined at peak
[c] Error in the FE joint strength compared to the test joint strength

When comparing the model with the material properties of curve and W/D coupons, the initial stiffness was identical and the joint strength of the curve coupons

was 4–9% greater than that of the W/D coupon FE model for all type of joints. In the experiment, it is expected that the heat affected zone has a significant influence on the joint behavior. Therefore, the use of material properties of W/D coupons is reasonable to regenerate the test results.

Meanwhile, the influence of weld size was also remarkable. As the size of reinforced weld decreased, not only the joint strength, but even the initial stiffness

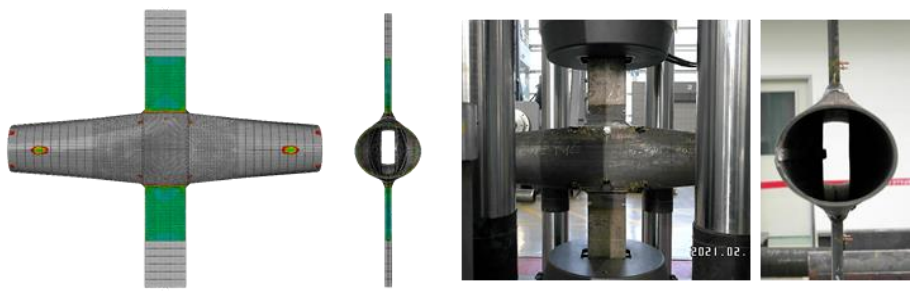

Figure 4.9. FE and test result of C-XP2-T-460 at fracture

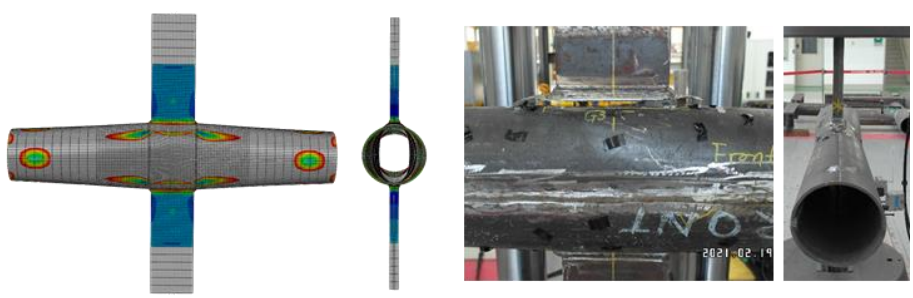

Figure 4.10. FE and test result of C-XP2-T-700 at fracture

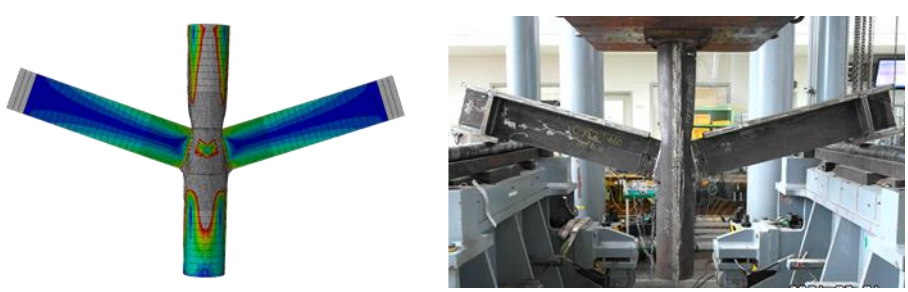

Figure 4.11. FE and test result of C-XP2-I-460 at the end of the test

declined. The trend particularly significant for IPB joint. There are 15–40% errors in the joint strength between the model without reinforced weld and with fully reinforced weld. It is noteworthy that careful consideration of the weld is needed when designing the joints.

As a result, FE models with reduced reinforced weld using material properties of W/D coupons showed satisfactory performance in predicting both the initial stiffness and behavior of the tested joints. Figures 4.9 through 4.11 show deformed shape of FE and test model at fracture or at the end of the experiment. It should also be noted that after the initial crack or fracture in the test specimen, the FE analysis could not well simulate the load-deformation behavior.

4.2. Geometric and material properties

4.2.1. Selection of nondimensional geometric parameters considered

There are two representative failure modes in the longitudinal plate-to-CHS joint: chord plastification and chord punching shear. Table 2.1 lists the relevant design limit states. Because it is difficult to reliably simulate a brittle chord punching shear failure through an FE analysis, the range of nondimensional geometric parameters to be considered for an FE analysis are carefully chosen to eliminate the possibility of chord punching shear; thus, only the joints failing in chord plastification are included in the analysis.

The procedure for selecting joint geometries that preclude chord punching shear is presented below. A joint has no chance of chord punching shear failure if the ultimate demand on that joint is below the design resistance corresponding to the chord punching shear limit state. Based on previous tests of Akiyama et el. (1974) and Makino et al (1994) and numerical results of Voth (2010), as presented in Figure

4.12, the upper bound of the ultimate demand on a joint may be estimated as 1.7 (XP joint) or 1.6 (TP joint) times the prEN 1993-1-8 (CEN (2019)) design resistance corresponding to the chord plastification. Figure 4.12 is redrawn from the original figures in Wardenier et al. (2018). The values of nondimensional geometric parameters η and 2γ are then chosen such that the punching shear design resistance is higher than the upper bound demand on a joint, or higher than 1.7- or 1.6-times the chord plastification design resistance; thus, chord plastification is triggered earlier than chord punching failure. The punching shear design resistance can be found in prEN 1993-1-8 (CEN (2019)) or ISO 14346 (ISO (2013)), which can be expressed as right-hand side of equations 4.1 and 4.2, respectively, for joints under a pure axial load and pure IPB (see Table 2.1).

$$1.7N_{Rd}\ \text{(XP) or}\ 1.6N_{Rd}\ \text{(TP)} < 1.16 f_{y0} t_0 h_1 \tag{4.1}$$

$$1.7M_{ip,Rd}\ \text{(XP) or}\ 1.6M_{ip,Rd}\ \text{(TP)} < 0.193 f_{y0} t_0 h_1^2 \tag{4.2}$$

where N_{Rd} and $M_{ip,Rd}$ are the axial and IPB design resistances, respectively.

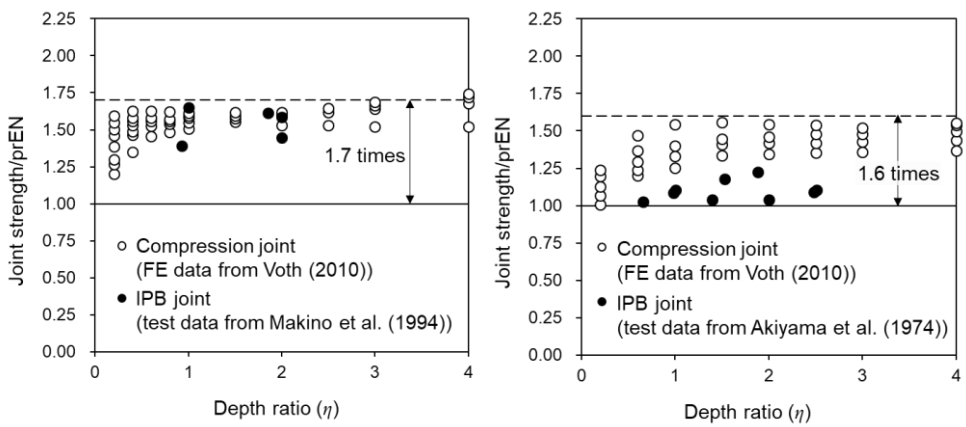

(a) XP joints (b) TP joints

Figure 4.12. Comparison of prEN 1993-1-8 design resistance with available data

Figures 4.13 and 4.14 show the selected sets of nondimensional parameters to be considered for the FE analysis. The gray region represents the geometries with no possibility of chord punching shear failure by satisfying the equations 4.1 and 4.2. It

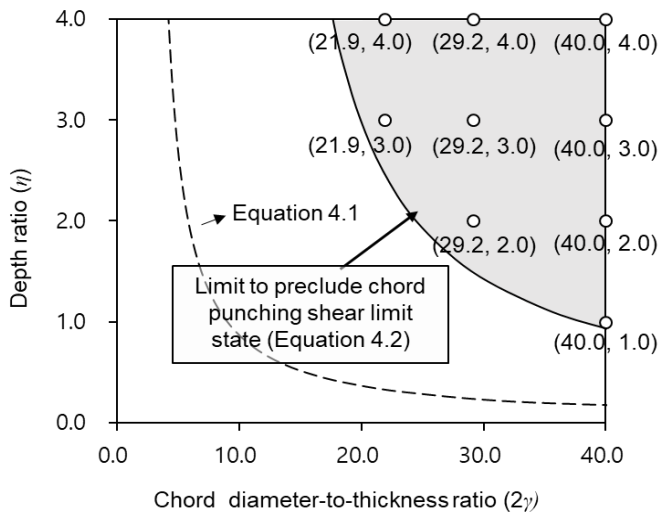

Figure 4.13. Selection of non-dimensional geometric parameters 2γ and η for longitudinal XP joints

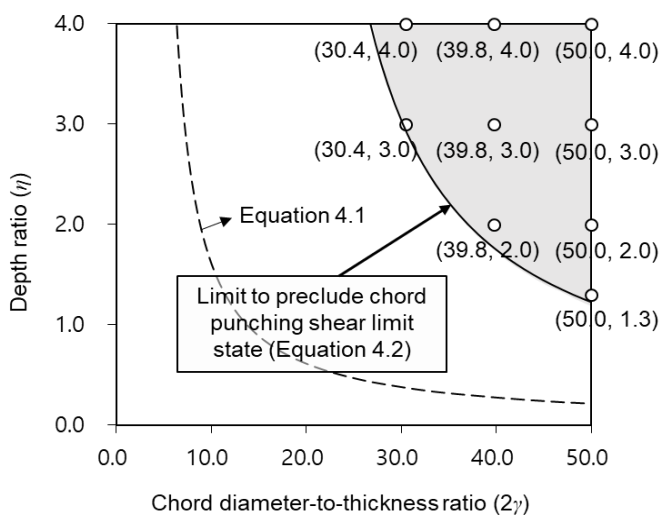

Figure 4.14. Selection of non-dimensional geometric parameters 2γ and η for longitudinal TP joints

will be shown later that all joints exhibit their ultimate joint resistance lower than the punching shear design resistance. The details of the joint models with the selected 18 geometries are presented in Table 4.2. The values of η range from 1.0 to 4.0, and 2γ from 21.9 to 40.0 (XP joint) or 30.4 to 50.0 (TP joint). Constant values were used for the chord diameter (d_0 = 350 mm) and plate thickness (t_1 = 24 mm).

Table 4.2. Geometric properties of FE analysis models

Model [a]	t_0 (mm)	h_1 (mm)	η	2γ	α
XP-1-40.0	8.8	350	1.0	40.0	20.0
XP-2-40.0	8.8	700	2.0	40.0	20.0
XP-3-40.0	8.8	1,050	3.0	40.0	20.0
XP-4-40.0	8.8	1,400	4.0	40.0	20.0
XP-2-29.2	12.0	700	2.0	29.2	20.0
XP-3-29.2	12.0	1,050	3.0	29.2	20.0
XP-4-29.2	12.0	1,400	4.0	29.2	20.0
XP-3-21.9	16.0	1,050	3.0	21.9	20.0
XP-4-21.9	16.0	1,400	4.0	21.9	20.0
TP-1-50.0	7.0	455	1.3	50.0	22.6
TP-2-50.0	7.0	700	2.0	50.0	24.0
TP-3-50.0	7.0	1,050	3.0	50.0	26.0
TP-4-50.0	7.0	1,400	4.0	50.0	28.0
TP-2-39.8	8.8	700	2.0	39.8	24.0
TP-3-39.8	8.8	1,050	3.0	39.8	26.0
TP-4-39.8	8.8	1,400	4.0	39.8	28.0
TP-3-30.4	11.5	1,050	3.0	30.4	26.0
TP-4-30.4	11.5	1,400	4.0	30.4	28.0

Additional properties:
d_0 = 350 mm, t_1 = 24 mm, w = 6mm, L_0 = 3500 mm (XP), L_0-h_1 = 3500 mm (TP), $L_1 = 1.5h_1$

[a] Identification of model: (Joint type)-(η)-(2γ)

4.2.2. Material properties

The material properties of the Korean steel SS400 and HSB600 used in the FE analysis are summarized in Table 4.3. The stress–strain curves of the steels taken from Lee et al. (2012b) are shown in Figure 4.15. The same material properties were

Table 4.3. Material properties used in FE analysis

Material grade	Measured yield stress, f_y (MPa)	Measured tensile stress, f_u (MPa)	Yield ratio f_y/f_u
SS400	356	497	0.72
HSB600	478	630	0.76

Nominal yield stress and tensile stress:
f_{yn} = 235 MPa, f_{un} = 400 MPa for SS400
f_{yn} = 450 MPa, f_{un} = 600 MPa for HSB600

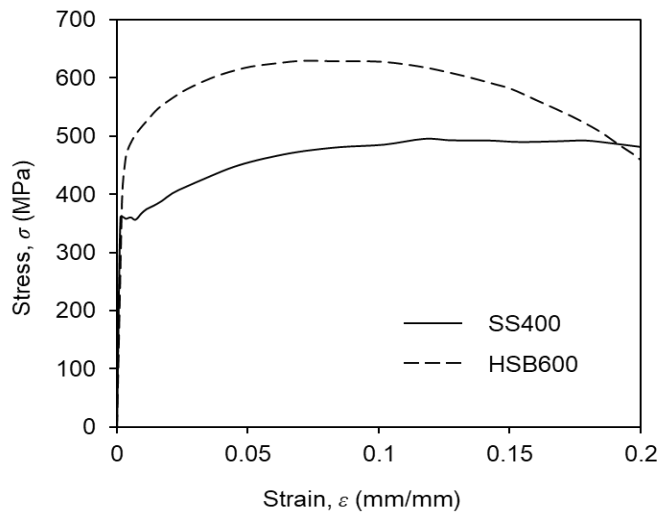

Figure 4.15. Stress-strain curves used in FE analysis
(reported by Lee at al. (2012b))

applied to all members of the models (chord, plate, and weldment). It can be observed that SS400 shows the material characteristics of typical mild steel, whereas HSB600, as a high-strength steel, shows a stress–strain curve with no distinct yield plateau and a reduced ultimate strain.

The measured yield stress of HSB600 (f_y = 478 MPa) is close to 460 MPa, facilitating an evaluation of the material factor for high-strength steel of up to 460 MPa specified in the design standards (see Table 2.2). According to prEN 1993-1-8

(CEN (2019)), the plate-to-CHS joints with steel grade HSB600 should apply material factor of 0.90. It should be noted that, in addition to the material factor-based reduction, a further reduction in the design resistance of high-strength steel joints can be made from the yield ratio limit of 0.80 ($f_{y0}/f_{u0} \leq 0.80$, as shown in Table 2.2). However, the yield ratio limit is considered to be more relevant to brittle failure modes (Packer (2020)), whereas the numerical investigation in this study is limited to a ductile chord plastification. Further, as shown in Table 4.3, the measured yield ratio of the high-strength steel considered in this study is smaller than 0.80 (0.76). Thus, the yield ratio limit is not discussed in this FE study. A total of 180 FE analyses were conducted on 18 models of plate-to-CHS joints with two steel grades (SS400 and HSB600) under compression, IPB, or combined loading (three patterns).

4.3. FE results of longitudinal plate-to-CHS joints under branch plate compression

4.3.1. Deformation limit criterion

For the plate-to-CHS joints under axial load, the widely accepted 3%d_0 deformation limit criterion was adopted. It was considered reasonable to apply the 3% limit because most of the existing studies on plate-to-CHS joints in axial load have used the 3% limit and the overall joint strength was determined at an acceptable point (near the peak load). However, as will be explained in the analysis results, for high-strength steel joints, the joint strength tends to be determined at a relatively early point than mild steel joints when using 3% limit. Nevertheless, the analysis results were evaluated with the 3%d_0 deformation limit criterion for conservatism and uniformity with international database.

4.3.2. Longitudinal X-type plate-to-CHS joints

In the typical deformed configurations of the FE model at the 3%d_0 deformation, overall chord plastification and stress concentration along the weld line were exhibited (see Figure 4.16). The black region in the figure indicates yielded area. At the 3% limit, the yielded area was decreased for HSB600 joint compared to SS400 joint, indicating that 3% limit criterion is slightly conservative for higher strength steel joints. The typical load-deformation curves are plotted in Figure 4.17. In can be seen that the deformation at the peak is larger in high-strength steel joints. The fixed indentation limit of 3% limit causes the strength of high-strength steel joints to be determined at premature point than mild steel joints.

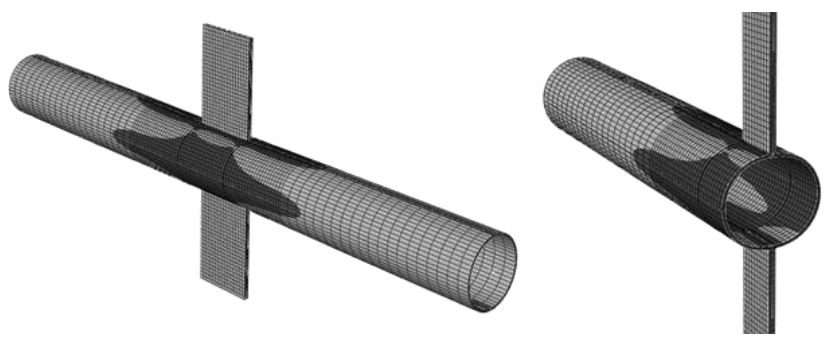

(a) SS400

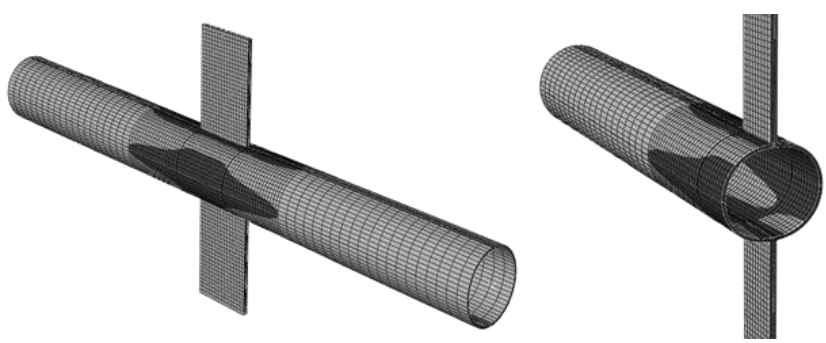

(b) HSB600

Figure 4.16. Typical deformed shape of compression-loaded XP joints (XP-1-40.0 model) at 3% limit (black region indicates yielding)

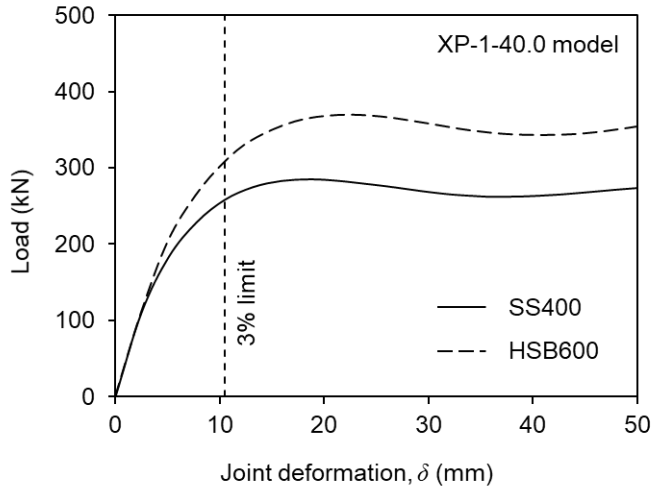

Figure 4.17. Typical load-deformation relationship for compression-loaded XP joints

Figure 4.18 shows the strength distribution of the longitudinal XP joints under axial compression obtained from the FE analysis. The joint strength (N_u) was normalized by the chord plastification design resistance per prEN 1993-1-8 (CEN (2019)) (N_{prEN}, see Table 2.1). Note that HSB600 has yield stress of 478 MPa, corresponding to the maximum applicable yield stress of 460 MPa according to prEN 1993-1-8. In preparing Figure 4.18, the material factor (C_f) was not applied. The normalized joint strength was plotted against the plate depth ratio (η). The joint strength of the axially loaded joints (N_u) was determined based on the 3%d_0 deformation limit criterion. When applying the deformation limit criterion, the joint deformation was assumed to be the relative vertical distance between the chord top face and the chord sidewall, as recommended by Voth and Packer (2012a, 2012b). For example, as shown in Figure 4.1, the out-of-plane indentation at the crown point is taken as the relative downward displacement at point A (or C) with respect to point B (or D). The detailed analysis results including load-deformation curves are presented in Appendix A.

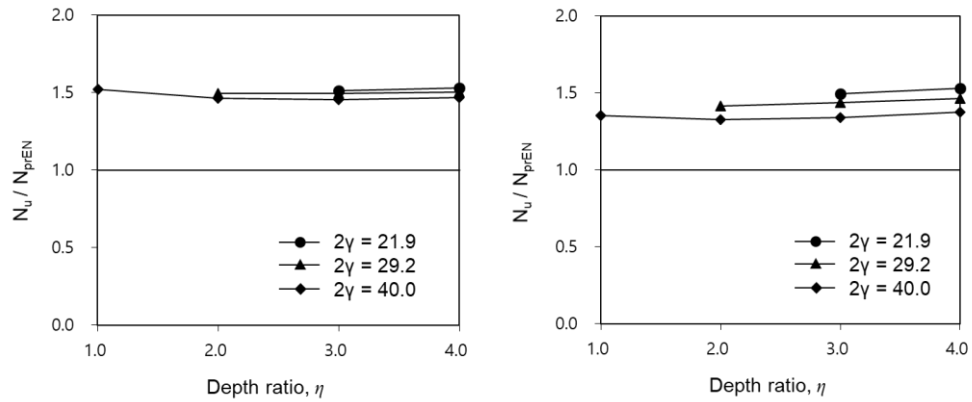

(a) SS400 (b) HSB600

Figure 4.18. Comparison of prEN 1993-1-8 design resistance and FE results for compression-loaded XP joints (material factor not included)

For the longitudinal XP joints in Figure 4.18, the values of the normalized joint strength are within the range of 1.45–1.53 for mild steel and 1.33–1.53 for high-strength steel. The high margin of safety for high-strength steel joints seems to indicate that the chord plastification design resistance formula in prEN 1993-1-8 could be extended to f_y = 460 MPa without applying the current material factor C_f = 0.9. There is no significant fluctuation depending on η, indicating that the η term in the design formula well expresses the joint behavior. On the other hand, there is a change in normalized strength of high-strength steel joints, indicating that the less stiff joints may more be sensitive to material properties.

The material factor can also be evaluated regardless of the specific design formula considered if joints with an identical geometry but made of different steel grades are directly compared. That is, the material factor required for high-strength steel can be obtained from each geometric configuration based on the normalized joint to material strength ratio. Or the required material factor can be calculated using equation 4.3.

$$C_{f,req} = \frac{\left(\frac{N_{u,\mathrm{HSS}}}{N_{u,\mathrm{MS}}}\right)}{\left(\frac{f_{y,\mathrm{HSS}}}{f_{y,\mathrm{MS}}}\right)} \tag{4.3}$$

where the subscripts HSS and MS denote high-strength steel and reference mild steel, respectively. In addition, $N_{u,HSS}$ and $N_{u,MS}$ represent the strengths of high-strength and mild steel joints with the same geometry, respectively. From a design perspective, the required material factor enables a design formula to provide a uniform safety margin for mild and high-strength steels. As shown in Figure 4.18, a decrease in the margin of safety is evident for HSB600 compared to SS400 when the material factor is not included. The material factor required for HSB600 (f_y = 478 MPa) relative to SS400 (f_y = 356 MPa), calculated using equation 4.10, ranges 0.89–1.00 for longitudinal XP joints (see Table 4.4). The material factor C_f = 0.9 for f_y = 460 MPa specified in prEN 1993-1-8 and ISO 14346 (ISO (2013)) corroborates the required material factor obtained for HSB600.

Table 4.4. Required material factor ($C_{f,req}$) for compression-loaded XP joints with HSB600

	η = 1.0	η = 2.0	η = 3.0	η = 4.0
2γ = 40.0	0.89	0.91	0.92	0.94
2γ = 29.2	-	0.95	0.96	0.97
2γ = 21.9	-	-	0.99	1.00

The evaluation of prEN 1993-1-8 with material factor of 0.9 was conducted with the FE results and available test database for compression-loaded longitudinal XP joints from Lee et al. (2012b), Togo (1967), and Makino (1984). The joint strength data of Togo and Makino are obtained by Voth (2010). The data of longitudinal XP joints under tension load were excluded from the evaluation. It is

noteworthy that the strength of tension-loaded joints is usually greater than compression-loaded joints, but most of design standards, such as prEN 1993-1-8 and ISO 14346, suggest the design formulae subjected to axial load (tension/compression) based on the joints under compression load due to the lower tensile deformability of the joints and conservatism.

Figure 4.19 shows the normalized joint strength for the FE results and test database. The joint strength was normalized by prEN 1993-1-8 design resistance and plotted against the measured yield stress or depth ratio (η). The material factor of 0.9 was applied for the joints with $356 < f_{y0} \leq 478$ MPa. The prEN 1993-1-8 design resistance including the material factor could provide uniform safety margin regardless of the yield stress or depth ratio (m = 1.53, CoV = 12.3%).

Meanwhile, the prEN 1993-1-8 design resistance is somewhat conservative, providing minimum safety margin of 1.3, as shown in Figure 4.19. However, it should be noted that the FE models all have one effective plate thickness including

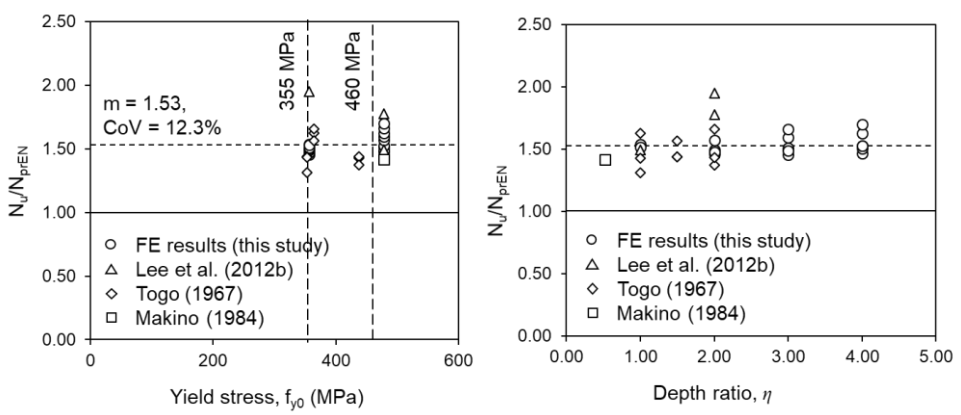

(a) Normalized joint strength against yield stress (f_{y0})

(b) Normalized joint strength against depth ratio (η)

Figure 4.19. Evaluation of prEN 1993-1-8 design resistance for compression-loaded XP joints with FE results in this study and available test database (material factor included)

plate thickness and weld size ($t_{1,eff} = t_1+2w$, see Figure 4.3). The information about effective thickness for most of experimental data were not provided. The effective thickness ratio ($\beta' = t_{1,eff}/d_0$) is 0.10 for the FE data. Instead, in the evaluation of the prEN 1993-1-8 design formula for axially loaded longitudinal XP joints, the various effective thicknesses were considered, and the influence of effective thickness can be expressed as function of β'. The design formula was suggested based on $\beta' = 0.05$ to exclude the increase in joint strength due to the large effective plate thickness (Wardenier (2018)). The FE data in this study may not give the most conservative joint strength because of the larger β' than 0.05. Therefore, it is recommended to use the design formula per prEN 1993-1-8 as it is as well as the material factor for longitudinal XP joints under axial load.

4.3.3. Longitudinal T-type plate-to-CHS joints

The typical deformed shape at 3%d_0 deformation limit and load-deformation relationship obtained from FE results are shown in Figures 4.20 and 4.21. As with the XP joints subjected to compression load, stress concentration occurred along the weld line accompanying with the overall plastification of the chord. In the load-deformation curves, the 3% limit criterion generally well predicts the peak load for the mild steel joints, while somewhat conservatively measuring the joint strength for high-strength steel joints.

The strength distribution of FE results for compression-loaded longitudinal TP joints is plotted in Figure 4.22. The joint strength (N_u) is normalized by the chord plastification design formula per prEN 1993-1-8 (CEN (2019)) (N_{prEN}, see Table 1) excluding the material factor. The joint strength was defined as preceding load between the peak load and the load at 3%d_0 deformation limit. The joint deformation was measured as the vertical distance between point A (or C) and point B (or D) in

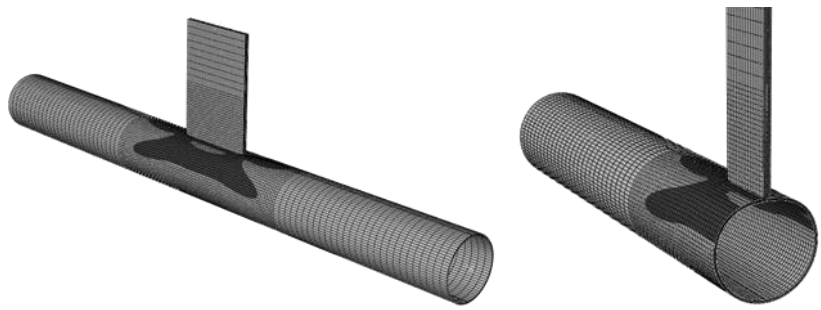

(a) SS400

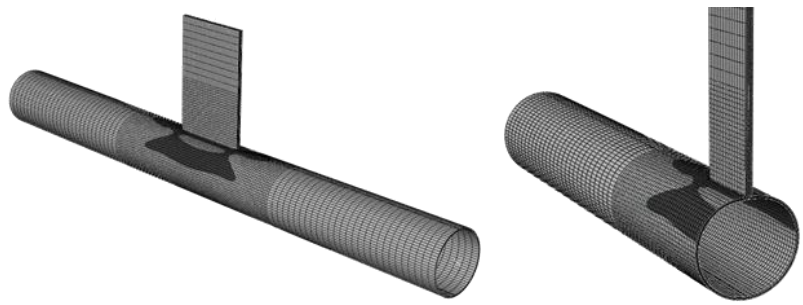

(b) HSB600

Figure 4.20. Typical deformed shape of compression-loaded TP joints (TP-1-50.0 model) at 3% limit (black region indicates yielding)

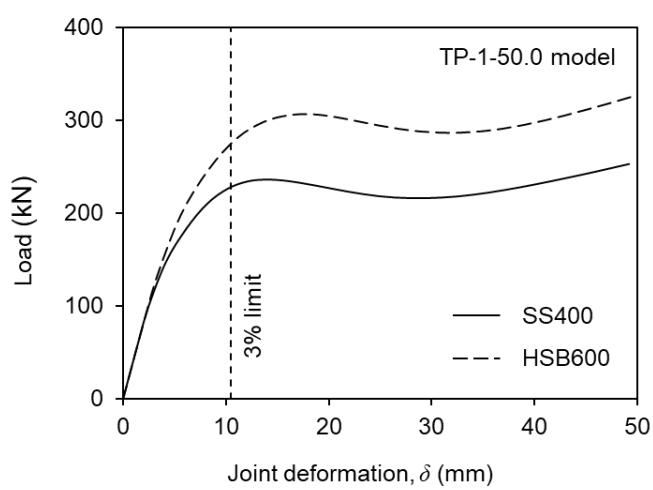

Figure 4.21. Typical load-deformation relationship for compression-loaded TP joints

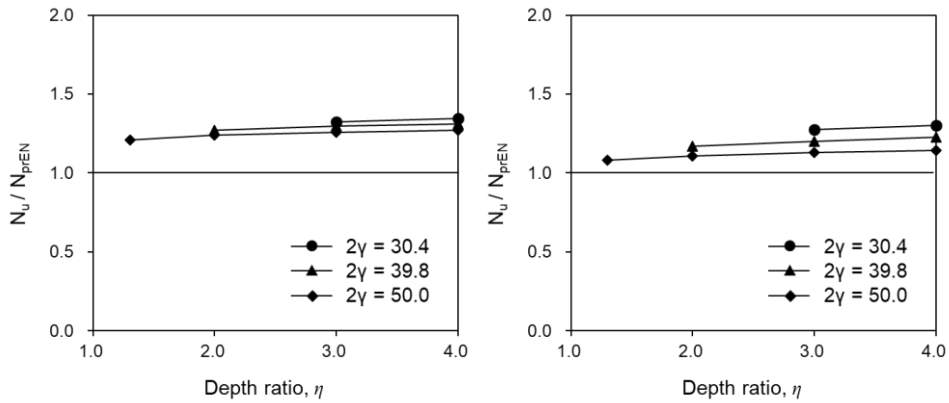

(a) SS400 (b) HSB600

Figure 4.22. Comparison of prEN 1993-1-8 design resistance and FE results for compression-loaded TP joints (material factor not included)

Figure 4.1. The joint strengths and load-deformation curves obtained from FE analysis are given in Appendix A.

For longitudinal TP joints under compression, the normalized joint strength ranges 1.21–1.34 for mild steel and 1.08–1.30 for high-strength steel (see Figure 4.22). The safety margins of mild steel as well as high-strength steel TP joints are relatively low compared to the design formula for XP joints. In addition, the material factor may be necessary for the high-strength steel TP joints with $2\gamma = 50$, in which a relatively lower safety margin is assured.

Table 4.5. Required material factor ($C_{f,req}$) for compression-loaded longitudinal TP joints with HSB600

	$\eta = 1.3$	$\eta = 2.0$	$\eta = 3.0$	$\eta = 4.0$
$2\gamma = 50.0$	0.90	0.89	0.90	0.90
$2\gamma = 39.8$	-	0.92	0.93	0.93
$2\gamma = 30.4$	-	-	0.97	0.97

The required material factors for HSB600 relative to SS400 are calculated with equation 4.3 for each FE models ($C_{f,req}$, see Table 4.5). The FE results provide required material factor of 0.89–0.97. Therefore, the use of C_f = 0.9 presented in prEN 1993-1-8 is recommended for compression-loaded longitudinal TP joints with HSB600.

The prEN 1993-1-8 design formula including material factor was evaluated with available experimental database from Washio et al. (1970), Akiyama et al. (1974), and Voth (2010) (see Figure 4.23). The joint strength data of Washio et al. reported by Voth was utilized. It is important to note that the FE data of TP joints generated by Voth (2010), which are the background data used for the formulation of the prEN 1993-1-8 design resistance, included only one plate thickness with a fixed fillet weld size. The effective thickness ratio ($\beta' = t_{1,eff}/d_0$) corresponds to 0.21 for the Voth data. Meanwhile, for XP joints, the design formula was proposed based on β' = 0.05. Therefore, additional FE analysis for TP joints with β' = 0.05 (t_1 = 12

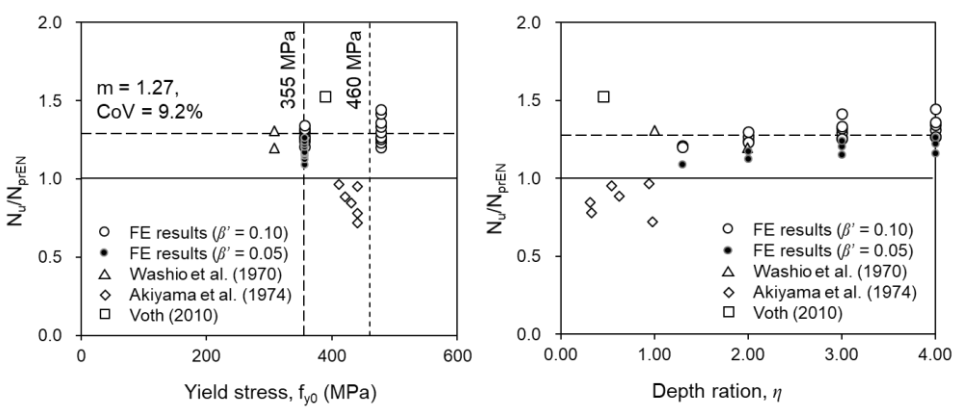

(a) Normalized joint strength against yield stress (f_{y0})

(b) Normalized joint strength against depth ratio (η)

Figure 4.23. Evaluation of prEN 1993-1-8 design resistance for compression-loaded TP joints with FE results in this study and available test database (material factor included)

mm, w = 3 mm) was carried out. The geometric properties are identical with original FE model except for plate thickness and weld size, and steel grade SS400 was applied. The value of β' was 0.10 for original FE models. Please refer to Appendix A for the detailed geometric information and joint strength.

Figure 4.23 illustrates the joint strength distribution normalized by prEN 1993-1-8 design resistance against yield stress or depth ratio (η). The material factor of 0.9 was applied to the joints with $356 < f_{y0} \leq 478$ MPa. In figure 4.23, the design resistance tends to overestimate the joint strength of Akiyama et al. (1974). The test specimens of Akiyama et al. had η within the range 0.3–1.0 of and 2γ within the range of 70.8–93.3, which is outside of the applicable range suggested by prEN 1993-1-8. The design formula could not assure reliability for joints outside the applicable range. In addition, the Voth data was measured very large due to the short chord length (α' = 4.2). Therefore, the data of Akiyama et al. and Voth will not be considered in this evaluation.

The prEN 1993-1-8 design formula including material factor well estimates the joint strength with generally uniform safety margin regardless of η or yield stress (m = 1.27, CoV = 9.2%). Meanwhile, the normalized joint strength of FE results with β' = 0.05 is clearly lower than that of original FE results, which has β' of 0.10. Nevertheless, the strength of joint with lower β' have some safety margin relative to the design formula. Therefore, for axially loaded longitudinal TP joints with applicable yield stress range of $f_y \leq 460$ MPa, the use of prEN 1993-1-8 design formula is suitable.

4.4. FE results of longitudinal plate-to-CHS joints under branch plate IPB

4.4.1. Proposal of deformation limit criterion

For the tubular joints under IPB, various rotation-based deformation limit criteria have been proposed in addition to 3% limit, as described in Section 2.2. The joint rotation-based limits suggested by Yu (1997) ($\varphi_{lim,Yu}$, equation 4.4), Lu and Wardenier (1994) ($\varphi_{lim,Lu}$, equation 4.5), and Kim and Lee (2021) ($\varphi_{lim,Kim}$, equation 4.6) are rewritten as equations. 4.4–4.6, respectively.

$$\varphi_{lim,Yu} = \frac{0.06}{\eta} \le 0.1 \text{ (rad)} \tag{4.4}$$

$$\varphi_{lim,Lu} = 0.1\frac{\beta}{\eta} \text{ (rad)} \tag{4.5}$$

$$\varphi_{lim,Kim} = 0.1\frac{\left(f_{u0}/f_{y0}\right)}{\left(f_u/f_y\right)_{S235}} \text{ (rad)} \tag{4.6}$$

However, the joint strength based on the criteria was determined by excessively small or large deformation for plate-to-CHS joints. Therefore, by combining key ideas from these existing limits, a new joint rotation limit, which is more rational for longitudinal plate-to-CHS joints under IPB, is proposed in equation 4.7. It should be noted that all limits in equations 4.4–4.6 are based on a reference value of 0.1 rad. Following this, a joint rotation of 0.1 rad is also employed as the basis for the new limit. If a fixed limit of 0.1 rad is applied regardless of the branch plate depth (h_1), proportionally larger and occasionally excessive out-of-plane joint deformation will be permitted for a wider branch plate, that is, for a larger η; e.g. when η = 4, the joint deformation of chord face is $0.2d_0$ at 0.1 rad. To prevent unacceptably excessive joint indentation or bulging when η is large, the ($1/\eta$)

correction from equation 4.4 or 4.5 is adopted in the proposed limit. Introducing the term ($1/\eta$), however, also brings about a side effect because an unrealistically large joint rotation will be allowed as η decreases. Various measures can be taken to overcome these side effects. For example, in equation 4.4, the upper bound rotation angle of 0.1 rad is set forth for joints with $\eta < 0.6$. The proposed limit also imposes the upper bound in a similar manner, as shown in equation 4.7. Meanwhile, the term β in equation 4.5 was originally intended to control the acceptable limit for a small η in I beam-to-RHS column connections, considering that β is generally small if η is small. The β correction is unsuitable for longitudinal plate-to-CHS joints because the value of β based on the plate thickness is extremely small, i.e., almost zero. The strain hardening correction in equation 4.6 is also included in the proposed limit to cover both mild and high-strength steel. With a nominal ultimate-to-yield stress ratio of S235, which is approximately 1.5, the proposed limit on the joint rotation angle in equation 4.7 can be further simplified as equation 4.8, which will be used throughout the study.

$$\varphi_{lim} = \frac{0.1}{\eta}\frac{\left(f_{u0}/f_{y0}\right)}{\left(f_u/f_y\right)_{S235}} \le 0.1\frac{\left(f_{u0}/f_{y0}\right)}{\left(f_u/f_y\right)_{S235}} \text{ (rad)} \tag{4.7}$$

$$\varphi_{lim} \text{ (simplified)} = \frac{1}{15\eta}\frac{f_{u0}}{f_{y0}} \le \frac{1}{15}\frac{f_{u0}}{f_{y0}} \text{ (rad)} \tag{4.8}$$

To prove the validity of the proposed deformation limit (equation 4.8), the comparison between conventional $3\%d_0$ deformation limit and the proposed deformation limit has been made. The 3% limit was proposed in order to be used for all types of tubular joints based on the empirical approach (Lu et al. (1994)). For the considered joints in the paper, the joint deformations corresponding to a peak load varied between 2.5–4.0%d_0. Moreover, the deformation limit of $3\%d_0$ was very close

to the inflection point in the load-deformation curves. Therefore, they recommended the 3%d_0 deformation limit criterion for any type of tubular joints. In addition, 3% limit implies that the joint deformation can be controlled to 1%d_0 or less at the action load level. If the load at the allowable deformation for serviceability limit state (N_s) is larger than (N_u/1.5) (equation 4.9), the serviceability check is unnecessary, indicating that the sufficient action load is permitted. In the equation 4.9, a constant of 1.5 is a product of action load factor (γ_g) and safety factor (γ_M). Lu et al. used 1%d_0 as a serviceability deformation limit and most of the data considered satisfied the relationship ($N_{s,1\%} \geq N_{u,3\%}$/1.5). The 1% limit is not used anymore in the tubular joints because it may become highly strict depending on the joint configurations. It is generally considered that the serviceability limit state can be neglected because the 3% limit itself is sufficiently conservative.

$$N_s \geq \frac{N_u}{1.5} \tag{4.9}$$

In Figure 4.24, the load-deformation diagrams obtained from the FE analysis for plate-to-CHS joints under IPB is plotted with the proposed joint rotation limit (equation 4.8) and 3% limit. In Figure 4.24(b), the joint rotation (φ) is converted to joint indentation (δ). Overall, the proposed limit corresponds to the post-yield state, where the re-gain of the stiffness commences by the membrane action. It should be noted that this stage of "inflection point" in the load-deformation curve has often been considered an appropriate choice for the ultimate deformation limit of the tubular joints (Makino et al. (1991), Lu et al. (1994), Lu and Wardenier (1994)). Utilizing a further strength beyond the "inflection point" does not appear feasible because of crack initiation and serviceability issues. Thus, it can be stated that the joint strength can be exploited with the proposed deformation limit. However, the ultimate joint strength is obtained at a small deformation when the 3%d_0 limit

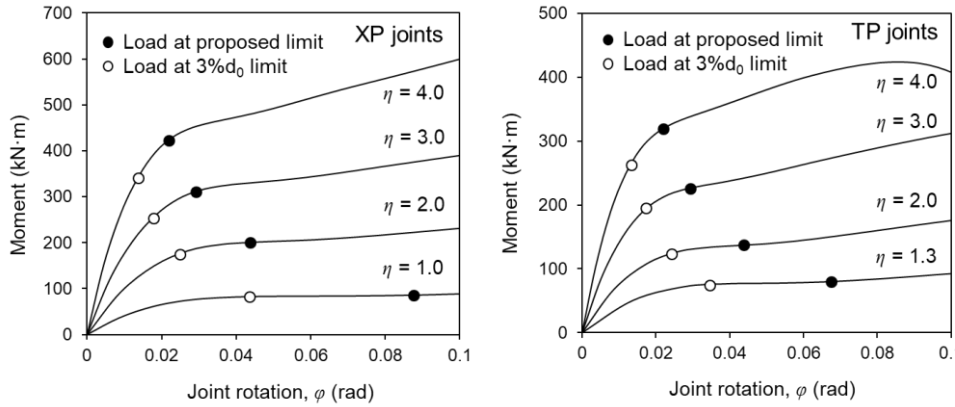

(a) Moment-rotation relationships for XP (left) and TP (right) joints

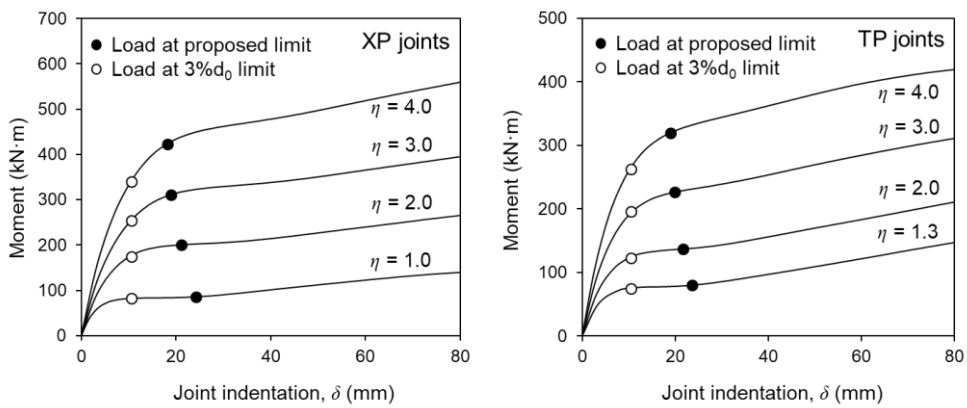

(b) Moment-indentation relationships for XP (left) and TP (right) joints

Figure 4.24. Comparison of 3%d_0 and proposed deformation limit for numerical IPB joints

criterion is applied. In particular, when η is high (e.g., η = 3.0 or 4.0), the 3%d_0 strength is determined at a too early loading stage where material yielding and subsequent strain hardening have not yet been fully developed. Meanwhile, the proposed limit corresponds to 4.4–4.6%d_0 which is slightly larger than 3%d_0. Therefore, it is reasonable to use re-defined deformation limit that allows to utilize more capacity of the joints with no significant increase in deformation.

To check the serviceability, the deformation corresponding to the serviceability load (N_s or M_s) that satisfies the equation 4.9 was calculated for IPB joints analyzed in this study. The ultimate joint strength (N_u or M_u) was obtained using proposed deformation limit criterion. The serviceability deformation ranged between 0.6–2.0%d_0, which was around 1%d_0. Accordingly, the proposed deformation limit (φ_{lim}) can be an alternative of traditional 3%d_0 limit both in terms of ultimate strength and serviceability for longitudinal plate-to-CHS joints under IPB.

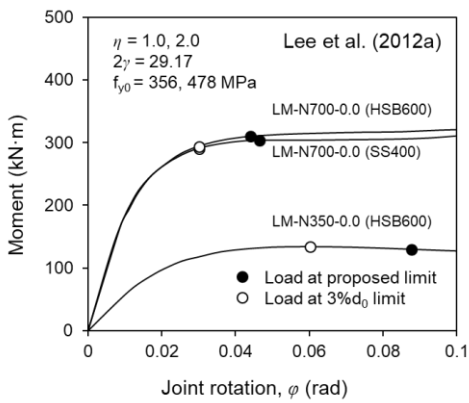

(a) XP joints from Lee et al. (2012a)

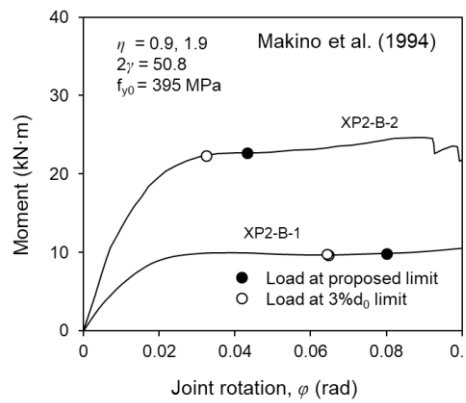

(b) XP joints from Makino el al. (1994)

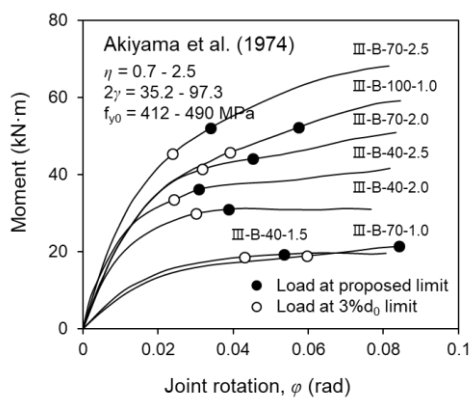

(c) TP joints from Akiyama et al. (1974)

Figure 4.25. Comparison of 3%d_0 and proposed deformation limit for IPB joints from available test data

The proposed deformation limit is further validated in Figure 4.25 using the available experimental load-deformation relationship. Again, the proposed limit provides a more reasonable ultimate joint strength compared to the 3%d_0 limit. As can be seen in Figure 4.25(c), even extremely high 2γ cases can also be covered by the proposed deformation limit criterion.

4.4.2. Longitudinal X-type plate-to-CHS joints

In the typical deformed configurations of the FE models with SS400 and HSB600 at the proposed deformation limit (equation 4.8), it can be obviously observed that the joint deformation is lager in compression side than tension side (see Figure 4.26). The yielded area is decreased in HSB600 joint compared to SS400 joint because the

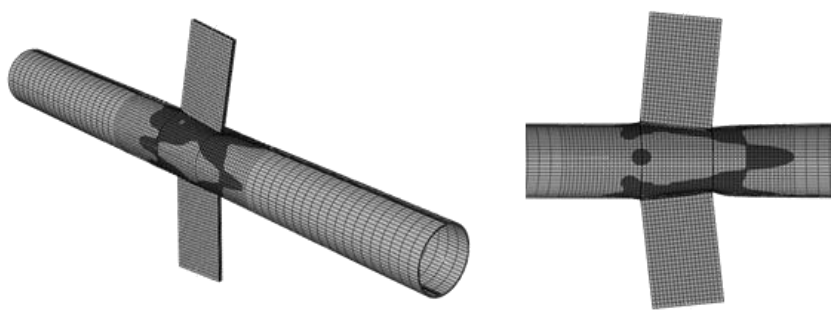

(a) SS400

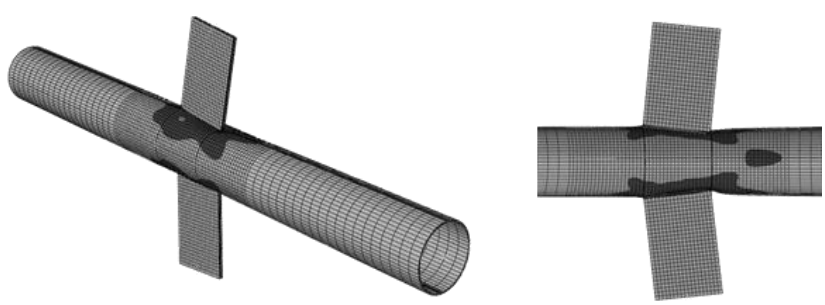

(b) HSB600

Figure 4.26. Typical deformed shape of IPB-loaded XP joints (XP-1-40.0 model) at the proposed deformation limit (black region indicates yielding)

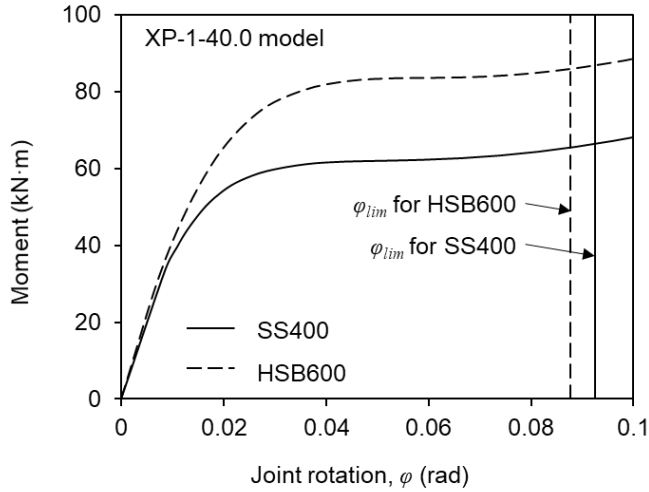

Figure 4.27. Typical moment-rotation relationship for IPB-loaded XP joints

proposed deformation limit was determined at earlier point for high-strength steel joints. The conservatism for high-strength steel joint was due to its lower rotational capacity. The typical moment-rotation relationship is plotted in Figure 4.27 including proposed deformation limit. For all of FE models, the peak load was not exhibited in the moment-rotation relationship.

Figure 4.28 shows the strength distribution of the longitudinal XP joints under IPB obtained from the FE analysis. The joint strength (M_u) was determined based on the proposed deformation limit criterion and normalized by the chord plastification design resistance in prEN 1993-1-8 (CEN (2019)) (M_{prEN}, see Table 2.1). The material factor was not applied in plotting Figure 4.28. As can be seen in Figure 4.28, prEN 1993-1-8 provides a non-conservative design resistance even for mild steel joints for larger depth ratio (η). The normalized joint strength ranges 0.99–1.63 for mild steel joints, and 0.98-1.57 for high-strength steel joints. To examine the effect of η on the joint strength in detail, the joint strength of FE results normalized to $M_u/(f_{y0}t_0^2h_1)$ was plotted with normalized design resistance in Figure 4.29. The

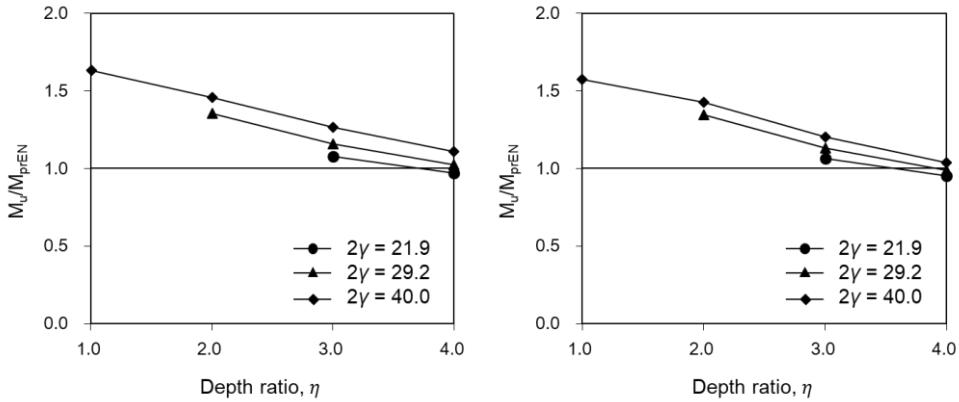

(a) SS400 (b) HSB600

Figure 4.28. Comparison of prEN 1993-1-8 design resistance and FE results for IPB-loaded XP joints (material factor not included)

normalized design resistance for XP joints per prEN 1993-1-8 is written in equation 4.10, which takes the η as a parameter.

$$M_{prEN} / (f_{y0} t_0^2 h_1) = 3.1(1 + 0.4\eta) \tag{4.10}$$

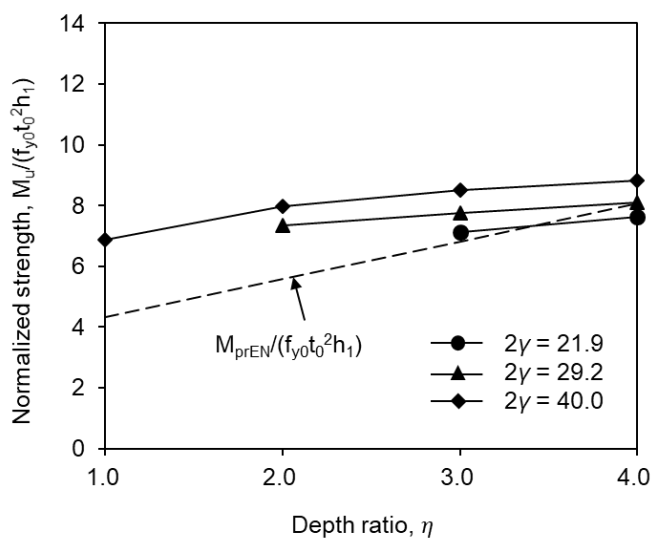

Figure 4.29. Influence of η on IPB-loaded XP joint strength

As η becomes larger, the normalized joint strength increased gently while the normalized design resistance increased rapidly. Consequently, the design resistance gets to over-predict the joint strength for large η.

Meanwhile, the normalized strength in Figure 4.28 shows little difference between the mild and high-strength steel joints. Table 4.6 summarizes the required material factors ($C_{f,req}$, see equation 4.3) for high-strength steel HSB600 (f_y = 478 MPa) relative to the mild steel SS400 (f_y = 356 MPa) based on the joint strength determined by the proposed rotation limit criterion. The required material factors are 0.93–0.99 for longitudinal XP joints. A comparison of the required material factors between axially loaded joints (see Table 4.4) and IPB-loaded joints clearly indicates that the material effect can vary among different loading types. It is also worth noting that the material effect has been found to be dependent on the joint type and the governing failure mode (Wardenier (2020)). Nonetheless, because the IPB design resistance is defined on the basis of the axial design resistance, the use of the same material factor for the two loading types may be favored for consistency. Thus, regardless of the loading type, a material factor of C_f = 0.9 is recommended based on the discussions in Section 4.3.2.

Table 4.6. Required material factor ($C_{f,req}$) for IPB-loaded longitudinal XP joints with HSB600

	η = 1.0	η = 2.0	η = 3.0	η = 4.0
2γ = 40.0	0.97	0.98	0.95	0.95
2γ = 29.2	-	0.99	0.97	0.96
2γ = 21.9	-	-	0.99	0.98

Figure 4.30 shows the strength distribution of the FE results and the test database obtained from Lee et al. (2012a) and Makino et al. (1994). The joint strength is also normalized by prEN 1993-1-8 design resistance and plotted against

yield stress (f_{y0}) or depth ratio (η). The prEN 1993-1-8 formula for XP joints in axial load was suggested based on the effective thickness ratio (β') of 0.05 in order to exclude the effect of plate thickness and weld leg size. Thus, the FE models with β' = 0.05 were additionally analyzed for IPB-loaded XP joints. The joint strength was determined based on the proposed deformation limit criterion (equation 4.8). In calculating design resistance, the material factor (C_f) of 0.9 was included for the joints with $356 < f_y \leq 478$ MPa. The tested IPB joint in Chapter 3, whose yield stress was much higher than 460 MPa, was excluded because the material factor could not be specified.

In Figure 4.30(a), the design resistance with C_f = 0.9 generally provides higher safety margins than that of mild steel joints. Meanwhile, the normalized joint strength for the experimental data as well as FE results tends to obviously decrease as the η increases, as was described in Figure 4.29 (see Figure 4.30(b)). It should be noted that the proposed deformation limit criterion allows more joint strength

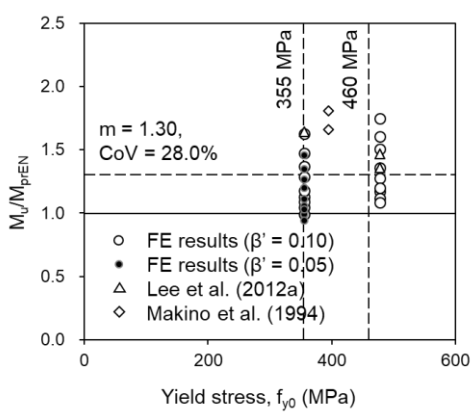

(a) Normalized joint strength against yield stress (f_{y0})

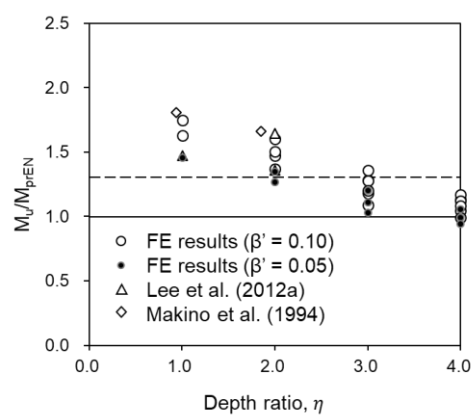

(b) Normalized joint strength against depth ratio (η)

Figure 4.30. Evaluation of prEN 1993-1-8 design resistance for IPB-loaded XP joints with FE results in this study and available test database (material factor included)

compared to 3% limit especially for high η (see Figure 4.24). Nevertheless, the design formula could not well capture the influence of η on the IPB joint strength.

4.4.3. Longitudinal T-type plate-to-CHS joints

The deformed shapes for IPB-loaded TP joint with SS400 and HSB600 at the proposed deformation limit (equation 4.8) are shown in Figure 4.31. The plastification of the chord occurred to some extent. Similar to XP joints, HSB600 joint has less yielded area compared to SS400 joints due to the conservatism of the proposed deformation limit for high-strength steel joints. The moment-rotation relationships obtained from FE analysis are plotted in Figure 4.32 with the proposed deformation limits depending on the steel grades.

In Figure 4.33, the joint strength is normalized by prEN 1993-1-8 (CEN (2019)) design resistance (M_{prEN}, see Table 1) without material factor (C_f). The

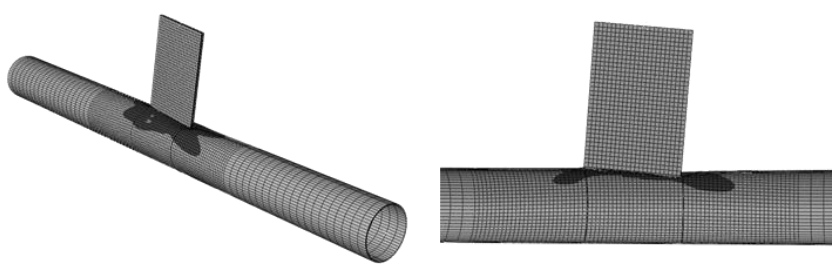

(a) SS400

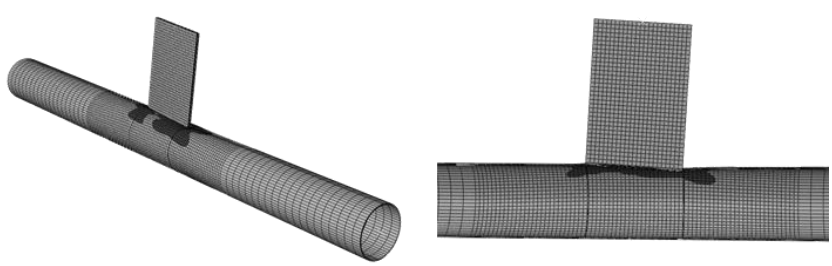

(b) HSB600

Figure 4.31. Typical deformed shape of IPB-loaded TP joints (TP-1-50.0 model) at the proposed deformation limit (black region indicates yielding)

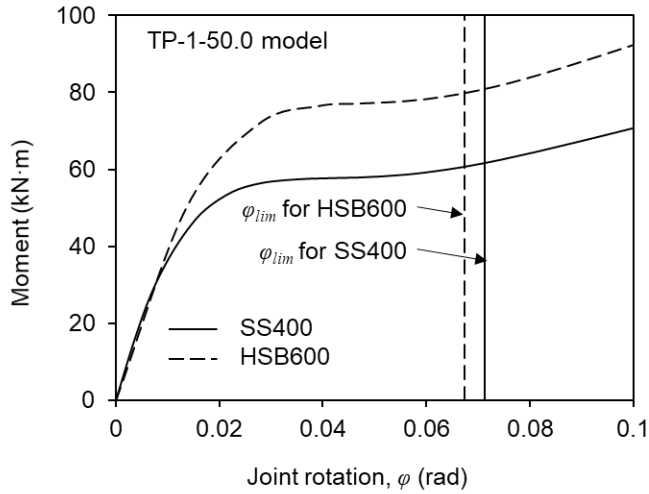

Figure 4.32. Typical moment-rotation relationship for IPB-loaded TP joints

equilibrium-induced bending moment in the chord should be considered for the TP joints, as shown in Figure 4.4(b). Therefore, the design resistance was calculated by including the chord stress function (Q_f, see prEN 1993-1-8 of Table 2.1). The chord stress effect was considerable for large η. The joint strength (M_u) was determined

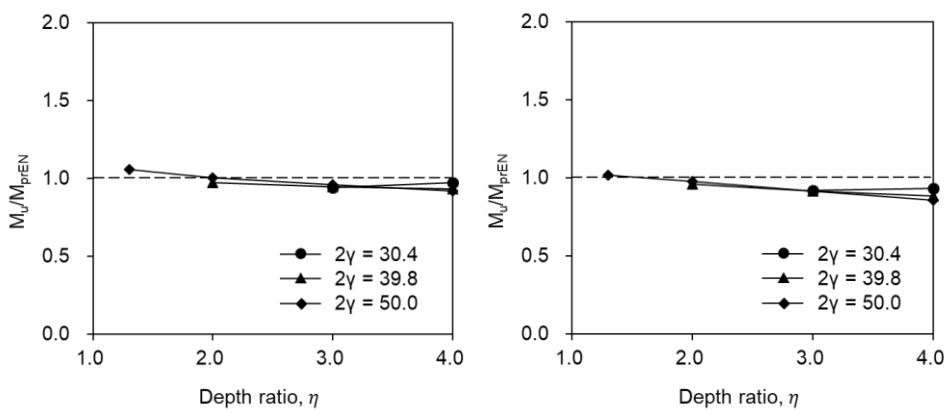

(a) SS400 (b) HSB600

Figure 4.33. Comparison of prEN 1993-1-8 design resistance and FE results for IPB-loaded TP joints (material factor not included)

based on the proposed deformation limit criterion. The design formula overestimates the joint strength regardless of yield stress, depth ratio (η), and chord diameter-to-thickness ratio (2γ). The influence of η on the strength of TP joints is less than that of XP joints. This clearly indicates the need for a re-examination of the formula.

To investigate the material effect on the joint strength in detail, the required material factors ($C_{f,req}$, see equation 4.3) for high-strength steel HSB600 (f_y = 478 MPa) relative to the mild steel SS400 (f_y = 356 MPa) were calculated with the FE results (see Table 4.7). The required material factors are 0.93–0.98 for IPB-loaded TP joints, which have mean value of 0.96. However, considering that the IPB design formula is based on the axial design formula, the material factor C_f = 0.9 is recommended for longitudinal TP joints under IPB, as suggested for the longitudinal TP joints under compression load (see Section 4.3.3).

Table 4.7. Required material factor ($C_{f,req}$) for IPB-loaded longitudinal XP joints with HSB600

	η = 1.3	η = 2.0	η = 3.0	η = 4.0
2γ = 50.0	0.96	0.97	0.95	0.93
2γ = 39.8	-	0.98	0.97	0.95
2γ = 30.4	-	-	0.98	0.96

To evaluate the prEN 1993-1-8 design formula with material factor, existing experimental database were utilized with the FE results. The load-deformation curves of test data were obtained from Akiyama et al. (1974), and the joint strength was defined with the proposed deformation limit criterion. Moreover, FE analysis on the IPB joints with β' = 0.05 were also conducted in order to evaluate the formula consistently with axially loaded joints. Figure 4.34 shows the normalized joint strength of the FE results and Akiyama et al. against yield stress or depth ratio. In

calculating the design resistance, the chord stress effect (Q_f) was included for all data and the material factor of 0.9 was used for the joints with f_{y0} > 356 MPa. The joint data of Akiyama et al. were divided to joints within the applicable range of 2γ per prEN 1993-1-8, and outside the applicable range.

In Figure 4.34, although the Akiyama et al. data with $2\gamma \geq 50.0$ were comparable to other data, the data were treated as outliers because the geometric parameters outside the applicable range are not the scope of this study. The safety margins for high-strength steel joints become higher than that for mild steel joints due to the material factor C_f = 0.9. However, overall design resistance overestimates the joint strength (m = 1.00, CoV = 10.8%), especially for the FE results of the joints with lower effective thickness ratio (β').

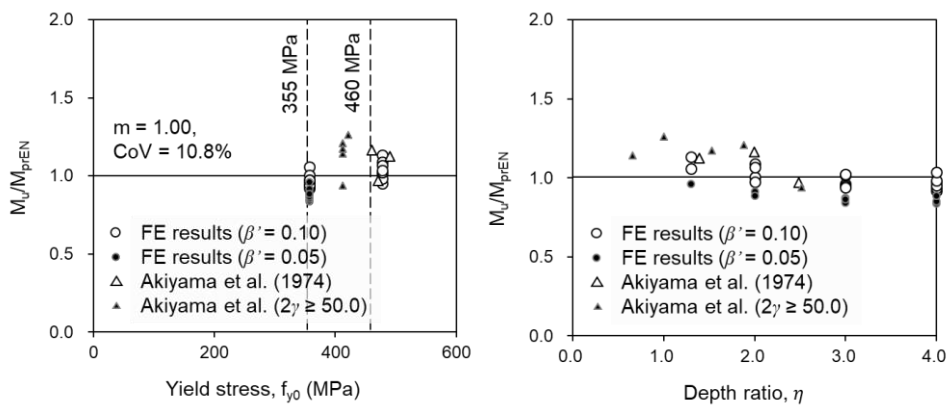

(a) Normalized joint strength against yield stress (f_{y0})

(b) Normalized joint strength against depth ratio (η)

Figure 4.34. Evaluation of prEN 1993-1-8 design resistance for IPB-loaded TP joints with FE results in this study and available test database (material factor included)

4.5. New proposal of interaction equation for longitudinal plate-to-CHS joints under combined compression and IPB

4.5.1. Proposal of deformation limit criterion

In this study, different ultimate deformation limits are suggested depending on the loading type, i.e., for axial compression, the traditional 3%d_0 limit, and for IPB loading, the joint rotation-based limit φ_{lim} (equation 4.8). For plate-to-CHS joints in which axial compression and IPB act simultaneously, both deformation limits are considered in defining the ultimate joint strength.

As shown in Figure 4.35, the joint deformation under combined loading can be divided into the average indentation component δ_{avg} (equation 4.11), and the rotation component φ (equation 4.12). The ultimate joint deformation was assumed to be reached when either δ_{avg} reaches 3%d_0 or φ reaches φ_{lim}. The combined joint strength (N_{uc}, M_{uc}) is then determined as the set of axial force and IPB moment at the ultimate joint deformation if this ultimate deformation state is not preceded by the peak axial load or peak IPB moment. If the peak axial load or peak IPB moment develops before the ultimate deformation state is reached, the combined joint

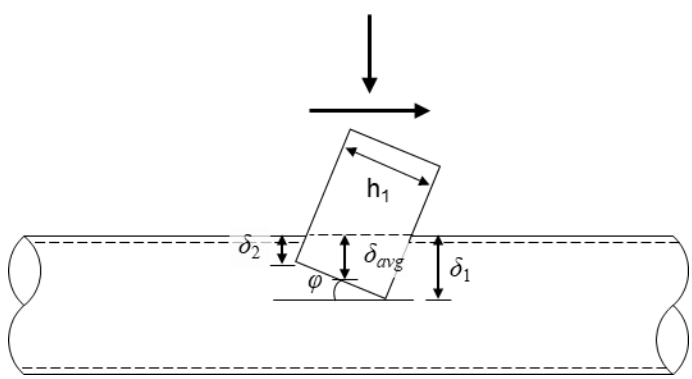

Figure 4.35. Symbols to define combined indentation and rotation-based deformation limit

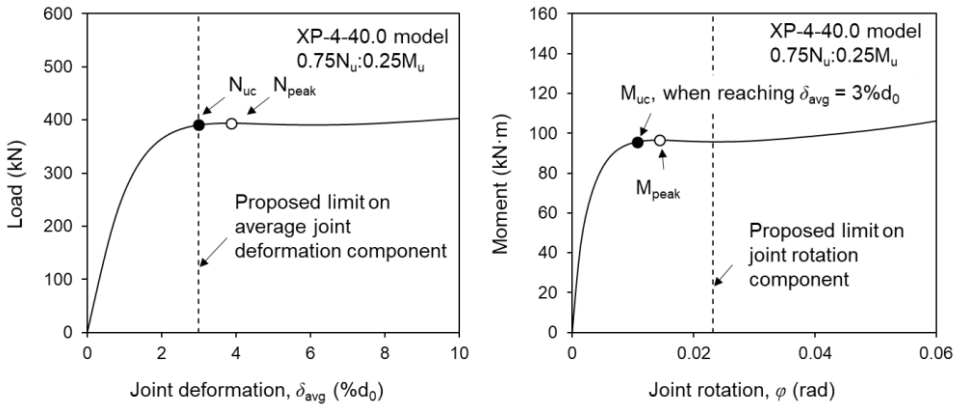

(a) Axial load-average indentation relationship

(b) IPB moment-rotation relationship

Figure 4.36. Determination of ultimate joint strength under combined load

strength is determined under the state corresponding to the earlier peak. An example of determining the combined joint strength is shown in Figure 4.36. In the case of Figure 4.36, the ultimate state is governed by the 3%d_0 limit. Please note that the 3%d_0 limit herein applies to the average joint deformation (δ_{avg}). This approach may seem unfamiliar because the 3%d_0 limit for tubular joints is generally associated with the maximum joint deformation (e.g., δ_1 or δ_2 in Figure 4.35). The average joint deformation is nonetheless used, considering that an excessively conservative combined joint strength will be obtained if the 3%d_0 criterion is based on the maximum joint deformation.

$$\delta_{avg} = \frac{\delta_1 + \delta_2}{2} \tag{4.11}$$

$$\varphi = \frac{\delta_1 - \delta_2}{h_1} \tag{4.12}$$

Based on the joint strengths obtained from the prior FE analyses for pure axial compression (N_u) and for pure IPB loading (M_u) (see Figures 4.18, 4.22, 4.28 and

4.33), the magnitudes of applied axial compression and IPB are set proportional to $0.75N_u$:$0.25M_u$, $0.50N_u$:$0.50M_u$, or $0.25N_u$:$0.75M_u$ during the analysis. Figure 4.37 shows the progress of the joint deformation depending on the ratio of the load combination. The circles represent the ultimate deformation states. As expected, the joint rotation component becomes more critical as the portion of the bending moment increases. It is noteworthy that a slight joint indentation component occurs even under pure IPB loading. This non-symmetric local deformation is due to the higher stiffness at the tension side of the IPB joint compared to the compression side, as shown in Figures 4.26 and 4.31.

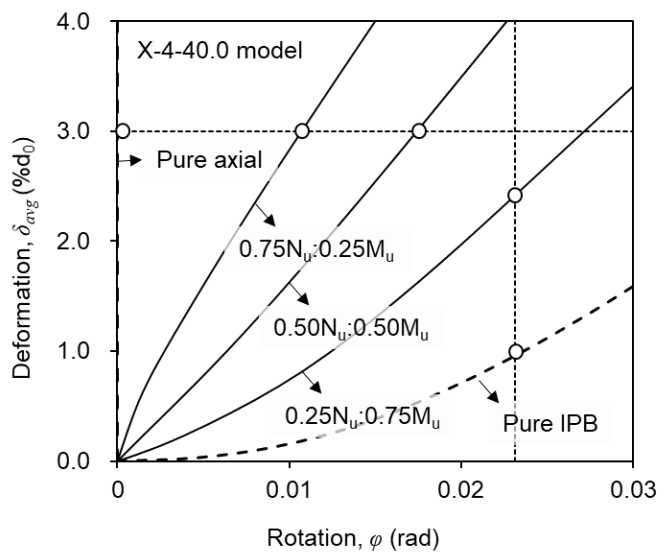

Figure 4.37. Example of determining joint deformation limit for combined load

4.5.2. Longitudinal X- and T-type plate-to-CHS joints

In Figure 4.38, the deformed shapes of longitudinal XP joints under combined load at ultimate deformation limit are shown, classified with loading pattern and steel grade. Depending on the loading pattern, the joints yields in slightly different

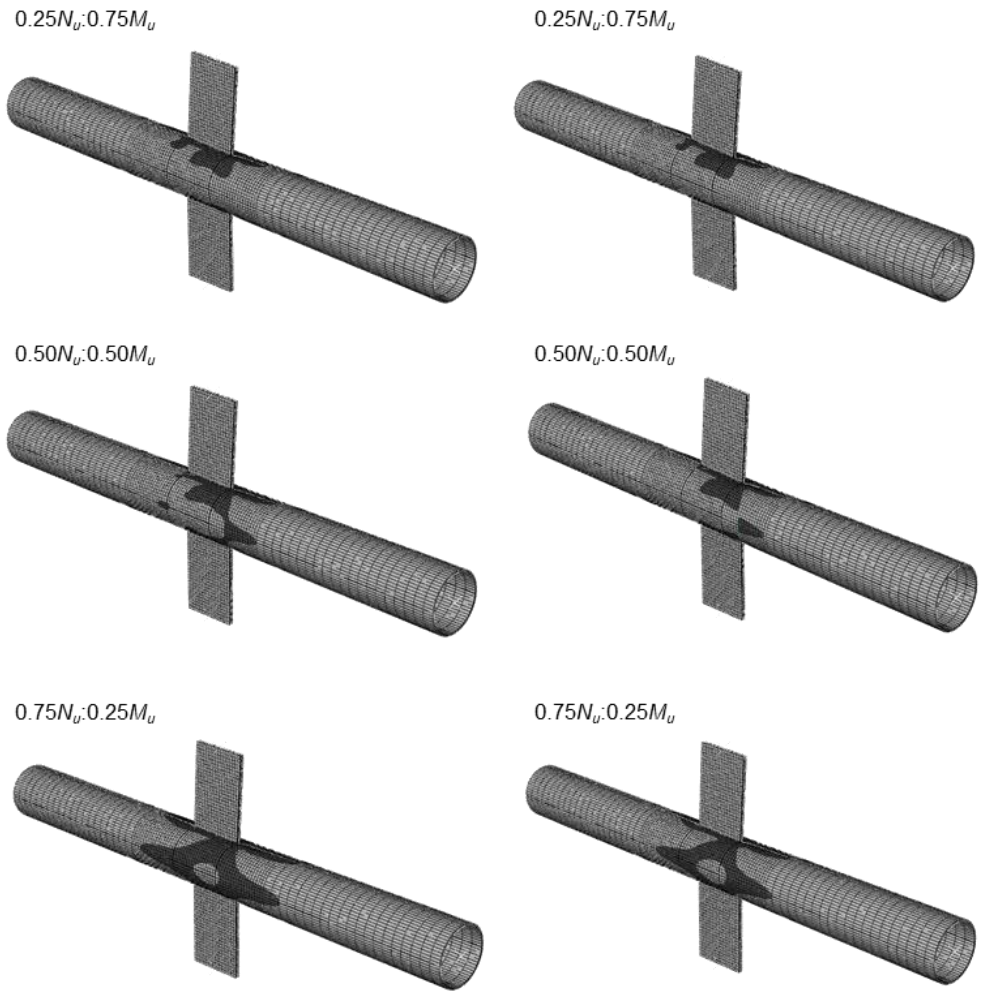

(a) SS400 (b) HSB600

Figure 4.38. Typical deformed shape of XP joints under combined load (XP-1-40.0 model) at ultimate deformation limit (black region indicates yielding)

aspect. Nonetheless, all of the joints exhibit stress concentration along the weld line. The yielded area is less for HSB600 joints compared to SS400 joints because the deformation limit is determined at earlier point for high-strength steel joints. The appearance or tendency of deformed shape of TP joints was similar to the XP joints.

The load-deformation curves for the joints under combined load are plotted in Appendix A.

Figure 4.39 plots the combined strength (N_{uc}, M_{uc}) of the longitudinal XP and TP joints, normalized by the joint strength under pure compression (N_u) or pure IPB (M_u). Both the linear interaction and the code-specified interaction equation for CHS-to-CHS joints (equation 4.13) are drawn. The interaction relationship of the XP joint is close to the convex profile shown in equation 4.13, whereas for the TP joints, it is closer to the linear interaction line. Mild and high-strength steel joints show similar load interaction trends. Regardless of the joint type (XP or TP) and steel grade, the use of the linear interpolation relationship is recommended as a conservative approach which can be expressed as equation 4.14

$$\frac{N}{N_{Rd}} + \left(\frac{M_{ip}}{M_{ip,Rd}} \right)^2 \leq 1.0 \tag{4.13}$$

$$\frac{N}{N_{Rd}} + \frac{M_{ip}}{M_{ip,Rd}} \leq 1.0 \tag{4.14}$$

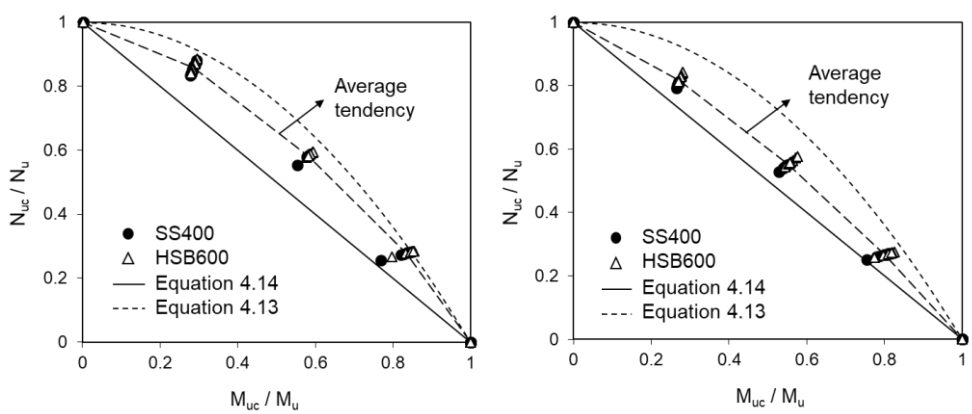

(a) XP joint (b) TP joint

Figure 4.39. Evaluation of interactive relationship

where N_{Rd} and $M_{ip,Rd}$ represent the design resistances for the individual loading cases of the axial load and IPB moment, and N and M_{ip} are the applied (factored) axial load and IPB moment, respectively.

In Figure 4.40, to check whether the interaction relationship depends on the specific deformation limit adopted, the combined joint strength is evaluated by adopting the 3%d_0 deformation limit criterion for all loading types (axial compression, IPB, and their combined loading). A comparison of Figures 4.39 and 4.40 shows that the interaction is only marginally affected by the deformation limit criteria, and a linear interaction can be assumed in both cases.

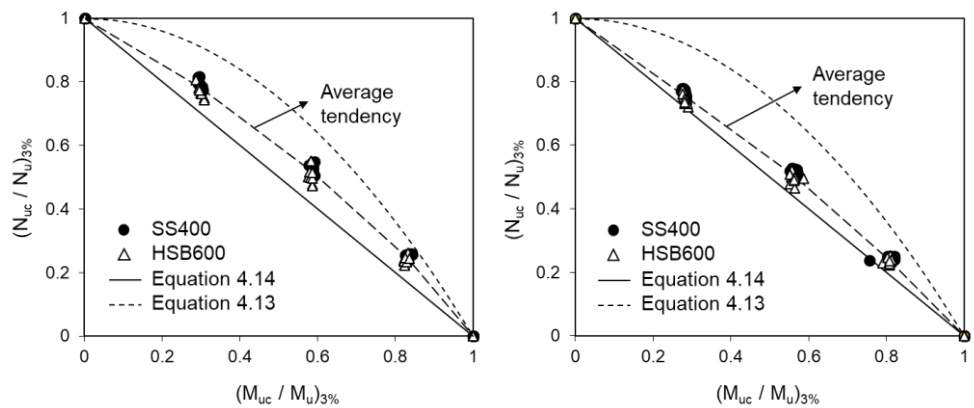

(a) XP joint (b) TP joint

Figure 4.40. Interactive relationship based on 3%d_0 deformation limit criterion

4.6. Recommendations for design

In Sections 4.3–4.5, the material factor and load interaction relationship were evaluated for longitudinal plate-to-CHS joints that failed through chord plastification. A code-specified material factor of $C_f = 0.9$ for $f_y = 460$ MPa was shown to be suitable for both the XP and TP joints regardless of the type of loading.

Table 4.8. Summary of recommended design method

Type of joint	Chord plastification design resistance [a]	Material factor	Deformation limit criterion
Longitudinal XP joint under axial load	$N_{Rd} = 4.4 C_f f_{y0} t_0^2 (1 + 0.4\eta) Q_f$	(1) C_f = 1.0 for $f_{y0} \le 355$ MPa (2) C_f = 0.9 for $355 \le f_{y0} \le 460$ MPa	$\delta \le \delta_{lim} = 3\% d_0$
Longitudinal TP joint under axial load	$N_{Rd} = 7.1 C_f f_{y0} t_0^2 (1 + 0.4\eta) Q_f$ Q_f: see prEN 1993-1-8 (Table 2.1)	(1) C_f = 1.0 for $f_{y0} \le 355$ MPa (2) C_f = 0.9 for $355 \le f_{y0} \le 460$ MPa	$\delta \le \delta_{lim} = 3\% d_0$
Longitudinal XP and TP joint under IPB	$M_{ip,Rd} = 0.7 N_{Rd} h_1$	-	$\varphi \le \varphi_{lim} = \frac{1}{15\eta}\left(\frac{f_{u0}}{f_{y0}}\right) \le \frac{1}{15}\left(\frac{f_{u0}}{f_{y0}}\right)$ (rad)
Longitudinal XP and TP joint under combined load	$\frac{N}{N_{Rd}} + \frac{M_{ip}}{M_{ip,Rd}} \le 1.0$	-	$\delta_{avg} \le \delta_{lim}$ and $\varphi \le \varphi_{lim}$ δ_{avg}, φ: see Figure 4.35

[a] Range of applicability: see prEN 1993-1-8 (Table 2.3)

Table 4.8 presents the prEN 1993-1-8 provisions supplemented by the linear interaction relationship proposed for the combined loading. The use of the new joint deformation limit criterion is also recommended in conjunction with the proposed design rules. The recommended deformation limit is based on the separate consideration of the joint indentation and joint rotation components. The basic design equations in prEN 1993-1-8 are retained, although they were shown to reduce the margin of safety for the joints loaded in IPB (see Figures 4.30 and 4.34). The evaluation of these basic equations is beyond the scope of the present study.

The proposed design resistances for the XP and TP joints (Table 4.8) are evaluated in Figure 4.41. For TP joints under combined or IPB loading, the chord stress function (Q_f) was included in the design resistance calculation because the chord stress was not compensated (see Figure 4.4). The conservatism and scatter in the prediction based on the design resistance equations may be evaluated by linearly combining the strength prediction ratios for axial compression and IPB (see equation 4.15 below), which is consistent with the linear interaction relationship assumed for the combined loading.

$$\chi_c = \frac{N_{uc}}{N_{Rd}} + \frac{M_{uc}}{M_{ip,Rd}} \tag{4.15}$$

In equation 4.15, N_{uc} and M_{uc} represent the joint strength under the combined loading, and N_{Rd} and $M_{ip,Rd}$ represent the joint axial and IPB design resistances, respectively. The mean (m) and coefficient of variation (CoV) of the prediction index χ_c were calculated using the FE data and are presented in Figure 4.41 for each joint type and steel grade. For the XP joints (Figure 4.41(a)), m = 1.48 and CoV = 18.6% were obtained for SS400, whereas m = 1.58, and CoV = 20.0% were obtained for HSB600. For the TP joints (Figure 4.41(b)), compared to the XP joints, the margin of safety

decreases but the scatter in the prediction is reduced. Overall, a slightly safer margin is provided for high-strength steel joints with the application of the material factor.

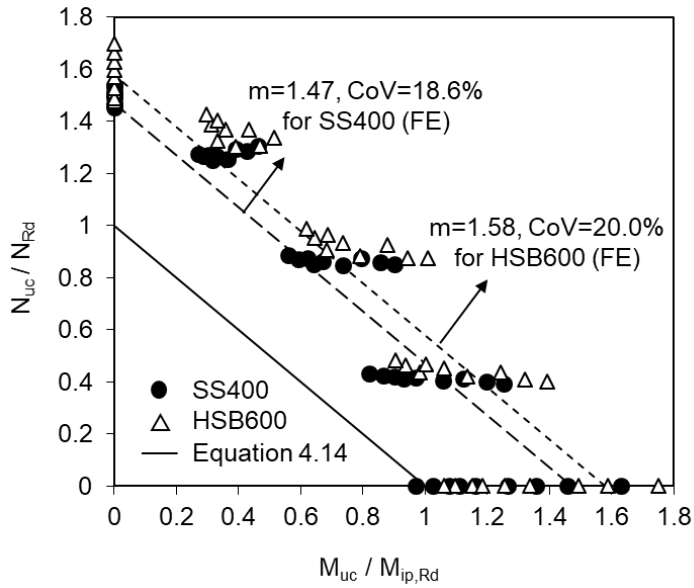

(a) XP joint

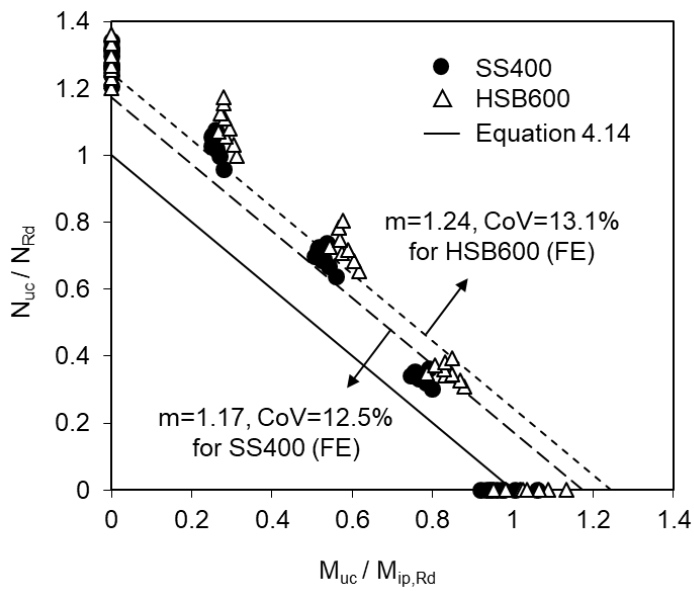

(b) TP joint

Figure 4.41. Evaluation of proposed design method

Chapter 5. Conclusions

In this study, the behavior of longitudinal X- and T-type plate-to-CHS joints with mild and high-strength steels was investigated under axial load, an in-plane bending (IPB) moment, and a combination of the two. The main findings of this study are summarized as follows:

i. In the experimental program, the tension-loaded joints with steel grades 460 and 700 exhibited fracture failure at 20%d_0 and 11%d_0, respectively. The IPB joint with steel grade 460 underwent 0.15 rad until the fracture. Compared to the deformation at ultimate joint strength, the tested high-strength steel joints showed sufficient deformation capacity.

ii. The strength of the tested joints provides high safety margin for prEN 1993-1-8 design resistance even without any material-related reduction.

iii. The possibility of relaxing the yield stress limitation according to prEN 1993-1-8 ($f_y \leq 460$ MPa) was suggested.

iv. In the FE analysis, the use of the widely accepted 3% indentation limit often results in a joint strength rating that is too conservative when the IPB moment acts on the joint with a high η.

v. A more rational criterion to determine the ultimate strength of longitudinal plate-to-CHS joints was proposed by considering both the 3% indentation limit and an additional limit on the joint rotation angle.

vi. Although the proposed deformation limit criterion allows more strength in the joint, the prEN 1993-1-8 design resistance can overestimate the ultimate IPB strength depending on the joint geometric parameters and requires further investigation.

vii. A code-specified material factor of 0.9 was found to be suitable for both longitudinal XP and TP joints with a chord yield stress of approximately 460 MPa.

viii. A linear interaction relationship was shown to be more appropriate for the design of longitudinal XP and TP joints under combined axial compression and IPB.

Bibliography

[1] Akiyama, N., Yajima, M., Akiyama, H., and Ohtake, A. (1974). "Experimental study on strength of joints in steel tubular structures." *Journal of Society of Steel Construction, 10*(102), 37-68 (in Japanese).

[2] CEN (2005). "Eurocode 3: Design of steel structures. Part 1. 8: Design of joints." *EN1993-1-8: 2005(E)*, European Committee for Standardization, Brussels, Belgium.

[3] CEN (2007). "Eurocode 3: Design of steel structures. Part 1. 12: Additional rules for the extension of EN 1993 up to steel grades S700." *EN1993-1-12: 2007(E)*, European Committee for Standardization, Brussels, Belgium.

[4] CEN (draft, 2019). "Eurocode 3: Design of steel structures. Draft Part 1-8: Design of joints." *prEN 1993-1-8*, European Committee for Standardization, Brussels, Belgium.

[5] Hoadley, P. W. (1984). "*Ultimate strength of tubular joints subjected to combined loads.*" Ph.D. dissertation, The University of Texas at Austin, TX.

[6] ISO (2013). "*Static design procedure for welded hollow-section joints – Recommendations.*" ISO 14346, International Organization for Standardization, Geneva, Switzerland.

[7] Kim, D.-K., Lee, C.-H., Han, K.-H., Kim, J.-H., Lee, S.-E., and Sim, H. B. (2013). "Compressive strength and residual stress evaluation of stub columns

fabricated of high strength steel." Proc., the seventh int symp. on steel structures (ISSS 2013), *Korean Society of Steel Construction*.

[8] Kim, S.-H. and Lee, C.-H. (2020). "Investigation of high-strength steel CHS X-Joints loaded in compression including effect of chord stresses." *Engineering Structures, 205*, 110052.

[9] Kim, S.-H. and Lee, C.-H. (2021). "Static behaviour of high-strength steel CHS T-Joints under in-plane moment loading." *Proc., the ninth European conf. on steel and composite structures*, Sheffield, UK.

[10] Kim, S.-H. and Lee, C.-H. (2018). "Structural performance of CHS X-joints fabricated from high-strength steel." *Steel Construction, 11*(4), 278-285.

[11] Lan, X., Chan, T. M., and Young, B. (2020). "Experimental study on the behaviour and strength of high strength steel CHS T- and X-joints." *Engineering Structures, 206*, 110182.

[12] Lee, C.-H., Kim, S.-H., Chung, D.-H., Kim, D.-K., and Kim, J.-W. (2017). "Experimental and numerical study of cold-formed high-strength steel CHS X-Joints." *Journal of Structural Engineering, 143*(8), 04017077.

[13] Lee, H.-D., Lee, S.-H., Chu, D.-S., Shin, H.-M., Shin, K.-J., Kim, H.-J., and Kim, W.-B. (2017). "Interaction strength for CHS-to-longitudinal plate joints under axial load and in-plane bending moment." Proc., the 9th int structural engineering and construction conf., *International Structural Engineering and Construction*, Spain.

[14] Lee, S.-H., Shin, K.-J., Lee, H.-D., Kim, W.-B., and Yang, J.-G. (2012a). "Behavior of plate-to-circular hollow section joints of 600MPa high-strength steel." *International Journal of Steel Structures, 12*(4), 473-482.

[15] Lee, S.-H., Shin, K.-J., Lee, H.-D., and Kim, W.-B. (2012b). "Test and analysis on the longitudinal gusset plate connection to circular hollow section (CHS) of

high strength." *Journal of Korean Society of Steel Construction*, *24*(1), 35-46 (in Korean).

[16] Lee, S.-H., Shin, K.-J., Kim, S.-Y., and Lee, H.-D. (2019). "Numerical study on the deformation behavior of longitudinal plate-to-high-strength circular hollow-section X-joints under axial Load." *Applied Sciences*, *9*(19), 3999.

[17] Liu, D. K. and Wardenier, J. (2004). *"Effect of the yield strength on the static strength of uniplanar K-joints in RHS (steel grades S460, S355 and S235)."* IIW Doc. XV-E-04-293, Delft University of Technology, Delft, The Netherlands.

[18] Lu, L. H., de Winkel, G. D., Yu, Y., and Wardenier, J. (1994). "Deformation limit for the ultimate strength of hollow section joints." Proc., the 6th int symp. on tubular structures, *Tubular Structures VI*, A. A. Balkema, Netherlands, 341-347.

[19] Lu, L. H. and Wardenier, J. (1994). "Ultimate deformation criteria for uniplanar connections between I-beams and RHS columns under in-plane bending." *Proc., the fourth int offshore and polar engineering conf.*, Osaka, Japan.

[20] Makino, Y. (1984). "*Experimental study on ultimate capacity and deformation for tubular joints*." Ph.D. dissertation, Osaka University, Osaka, Japan (in Japanese).

[21] Makino, Y., Kurobane, Y., Paul, J. C., Orita, Y., and Hiraishi, K. (1991). "Ultimate capacity of gusset plate-to-tube connections under axial and in-plane bending loads." Proc., the 4th int symp. on tubular structures, *Tubular Structures IV*, Delft University Press, Delft, The Netherlands, 424-434.

[22] Meng, X. and Gardner, L. (2020). "Cross-sectional behaviour of cold-formed high strength steel circular hollow sections." *Thin-Walled Structures*, *156*, 106822.

[23] Packer, J. A. (2020). “Connection design with high-strength HSS.” *Steel Tube Institute*.

[24] Simulia (2014). “Abaqus 6.14: Abaqus/CAE user’s guide.” *Simulia*, Providence, RI.

[25] Togo, T. (1967). *Experimental study on mechanical behaviour of tubular joints*. D.Eng. thesis, Osaka University, Osaka, Japan (in Japanese).

[26] Voth, A. P. (2010). “*Branch plate-to-circular hollow structural section connections.*” Ph.D. dissertation, University of Toronto, Canada.

[27] Voth, A. P. and Packer, J. A. (2012). “Branch plate-to-circular hollow structural section connections. I: Experimental investigation and finite-element modeling.” *Journal of Structural Engineering, 138*(8), 995-1006.

[28] Voth, A. P. and Packer, J. A. (2012). “Branch plate-to-circular hollow structural section connections. II: X-Type parametric numerical study and design.” *Journal of Structural Engineering – ASCE, 138*(8), 1007-1018.

[29] Voth, A. P. and Packer, J. A. (2012). “Numerical study and design of T-type branch plate-to-circular hollow section connections.” *Engineering Structures, 41*, 477-489.

[30] Wardenier, J. (2020). *“Considerations with respect to high strength steel (S460-S700) hollow section joints.”* IIW Doc. XV-E-486-20.

[31] Wardenier, J., Kurobane, Y., Packer, J. A., van der Vegte, G. J., and Zhao, X.-L. (2008). “*Design guide for circular hollow section (CHS) joints under predominantly static loading, 2nd ed.*” CIDECT, Geneva, Switzerland.

[32] Wardenier, J., Packer, J. A., and Puthli, R. (2018). “Simplified design equations for plate-to-CHS T and X Joints for use in codes.” *Steel Construction, 11*(2), 146-161.

[33] Washio, K., Kurobane, Y., Togo, T., Mitsui, Y., and Nagao, N. (1970). "Experimental study of ultimate capacity for tube to gusset plate joints - part 1." *Proc., the annu conf. of the AIJ,* Japan.

[34] Yu, Y. (1997). "*The static strength of uniplanar and multiplanar connections in rectangular hollow sections.*" Ph.D. dissertation, National Univ. of Singapore, Singapore.

[35] Zhao, X.-L., Herion, S., Packer, J.A., Puthli, G. Sedlacek, G., Wardenier, J., Weynand, K., van Wingerde, A.M., and Yeomans, N.F. (2000). "*Design guide for circular and rectangular hollow section welded joints under fatigue loading.*", CIDECT and TÜV Verlag GmbH, Köln, Germany.

Appendix A. FE results

This Appendix chapter summarizes the joint ultimate strength and load-deformation relationships obtained from numerical analysis. Please refer to Table 4.2 in Chapter 4 for detailed geometric dimensions of the joints. Based on the deformation limit criterion in Table 4.8, the ultimate strength of the joint is determined as the preceding one among the peak load and the load corresponding to the deformation limit. The analysis results are organized into three sections: (1) longitudinal X-type plate-to-CHS joints, (2) longitudinal T-type plate-to-CHS joints, (3) longitudinal X- and T-type plate-to-CHS joints with an effective thickness ratio (β') of 0.05.

Table A.1. Analysis results for longitudinal X-type plate-to-CHS joints (continued)

Model	η	2γ	f_{y0} (MPa)	Loading pattern N/N_u:M/M_u	N_{uc} (kN)	M_{uc} (kN·m)	N_{uc}/N_u	M_{uc}/M_u
XP-1-40.0	1	40.0	356	Pure axial	258.4	0.0	1.00	0.00
				0.75:0.25	219.4 [a]	18.6 [a]	0.85	0.28
				0.50:0.50	143.0 [a]	36.3 [a]	0.55	0.55
				0.25:0.75	66.2 [a]	50.4 [a]	0.26	0.77
				Pure IPB	0.0	65.6	0.00	1.00
			478	Pure axial	307.9	0.0	1.00	0.00
				0.75:0.25	271.4	25.0	0.88	0.29
				0.50:0.50	177.5	49.1	0.58	0.58
				0.25:0.75	81.8 [a]	67.9 [a]	0.27	0.80
				Pure IPB	0.0	85.1	0.00	1.00
XP-2-40.0	2	40.0	356	Pure axial	315.8	0.0	1.00	0.00
				0.75:0.25	278.0	44.7	0.88	0.29
				0.50:0.50	185.6	89.5	0.59	0.59
				0.25:0.75	86.4	125.0	0.27	0.82
				Pure IPB	0.0	152.3	0.00	1.00
			478	Pure axial	385.1	0.0	1.00	0.00
				0.75:0.25	341.2	59.2	0.89	0.30
				0.50:0.50	228.5	119.0	0.59	0.59
				0.25:0.75	106.7	166.8	0.28	0.83
				Pure IPB	0.0	200.5	0.00	1.00
XP-3-40.0	3	40.0	356	Pure axial	383.4	0.0	1.00	0.00
				0.75:0.25	330.9	70.0	0.86	0.29
				0.50:0.50	223.3	141.6	0.58	0.58
				0.25:0.75	106.8	203.2	0.28	0.84
				Pure IPB	0.0	243.3	0.00	1.00
			478	Pure axial	474.3	0.0	1.00	0.00
				0.75:0.25	414.9	90.6	0.87	0.29
				0.50:0.50	280.9	184.1	0.59	0.59
				0.25:0.75	134.2	263.8	0.28	0.85
				Pure IPB	0.0	310.8	0.00	1.00
XP-4-40.0	4	40.0	356	Pure axial	458.2	0.0	1.00	0.00
				0.75:0.25	390.6	95.7	0.85	0.28

[a] Joint strength which is determined at peak load

Table A.1. Analysis results for longitudinal X-type plate-to-CHS joints (continued)

Model	η	2γ	f_{y0} (MPa)	Loading pattern N/N_u:M/M_u	N_{uc} (kN)	M_{uc} (kN·m)	N_{uc}/N_u	M_{uc}/M_u
XP-4-40.0	4	40.0	356	0.50:0.50	265.2	194.9	0.58	0.58
				0.25:0.75	128.3	283.0	0.28	0.84
				Pure IPB	0.0	336.8	0.00	1.00
			478	Pure axial	575.5	0.0	1.00	0.00
				0.75:0.25	499.3	122.2	0.87	0.29
				0.50:0.50	341.9	251.1	0.59	0.59
				0.25:0.75	163.8	360.9	0.28	0.85
				Pure IPB	0.0	422.6	0.00	1.00
XP-2-29.2	2	29.2	356	Pure axial	606.1	0.0	1.00	0.00
				0.75:0.25	524.8	76.2	0.87	0.29
				0.50:0.50	354.8 [a]	154.7 [a]	0.59	0.59
				0.25:0.75	167.2 [a]	218.6 [a]	0.28	0.83
				Pure IPB	0.0	264.2	0.00	1.00
			478	Pure axial	770.8	0.0	1.00	0.00
				0.75:0.25	671.0	102.1	0.87	0.29
				0.50:0.50	453.3	206.9	0.59	0.59
				0.25:0.75	213.8 [a]	292.8 [a]	0.28	0.83
				Pure IPB	0.0	351.7	0.00	1.00
XP-3-29.2	3	29.2	356	Pure axial	741.6	0.0	1.00	0.00
				0.75:0.25	628.9	117.9	0.85	0.28
				0.50:0.50	429.2	241.4	0.58	0.58
				0.25:0.75	206.6 [a]	348.5 [a]	0.28	0.84
				Pure IPB	0.0	417.0	0.00	1.00
			478	Pure axial	957.6	0.0	1.00	0.00
				0.75:0.25	820.5	155.8	0.86	0.29
				0.50:0.50	559.5	318.9	0.58	0.58
				0.25:0.75	270.0	461.5	0.28	0.85
				Pure IPB	0.0	545.7	0.00	1.00
XP-4-29.2	4	29.2	356	Pure axial	881.8	0.0	1.00	0.00
				0.75:0.25	742.6	163.4	0.84	0.28
				0.50:0.50	510.2	336.7	0.58	0.58
				0.25:0.75	248.4	491.8	0.28	0.85

[a] Joint strength which is determined at peak load

Table A.1. Analysis results for longitudinal X-type plate-to-CHS joints

Model	η	2γ	f_{y0} (MPa)	Loading pattern N/N_u:M/M_u	N_{uc} (kN)	M_{uc} (kN·m)	N_{uc}/N_u	M_{uc}/M_u
XP-4-29.2	4	29.2	356	Pure IPB	0.0	581.9	0.00	1.00
			478	Pure axial	1152.8	0.0	1.00	0.00
				0.75:0.25	982.9	214.2	0.85	0.28
				0.50:0.50	676.6	442.4	0.59	0.59
				0.25:0.75	327.9	643.1	0.28	0.85
				Pure IPB	0.0	753.8	0.00	1.00
XP-3-21.9	3	21.9	356	Pure axial	1333.3	0.0	1.00	0.00
				0.75:0.25	1121.3	190.7	0.84	0.28
				0.50:0.50	772.3 [a]	394.1 [a]	0.58	0.58
				0.25:0.75	372.7 [a]	570.6 [a]	0.28	0.84
				Pure IPB	0.0	680.5	0.00	1.00
			478	Pure axial	1772.1	0.0	1.00	0.00
				0.75:0.25	1496.9	254.9	0.84	0.28
				0.50:0.50	1029.7	526.1	0.58	0.58
				0.25:0.75	499.6	765.7	0.28	0.85
				Pure IPB	0.0	905.4	0.00	1.00
XP-4-21.9	4	21.9	356	Pure axial	1595.9	0.0	1.00	0.00
				0.75:0.25	1331.2	270.1	0.83	0.28
				0.50:0.50	924.1	562.6	0.58	0.58
				0.25:0.75	450.5	822.7	0.28	0.85
				Pure IPB	0.0	971.6	0.00	1.00
			478	Pure axial	2139.2	0.0	1.00	0.00
				0.75:0.25	1797.5	359.9	0.84	0.28
				0.50:0.50	1246.1	748.4	0.58	0.58
				0.25:0.75	607.4	1094.4	0.28	0.85
				Pure IPB	0.0	1284.8	0.00	1.00

[a] Joint strength which is determined at peak load

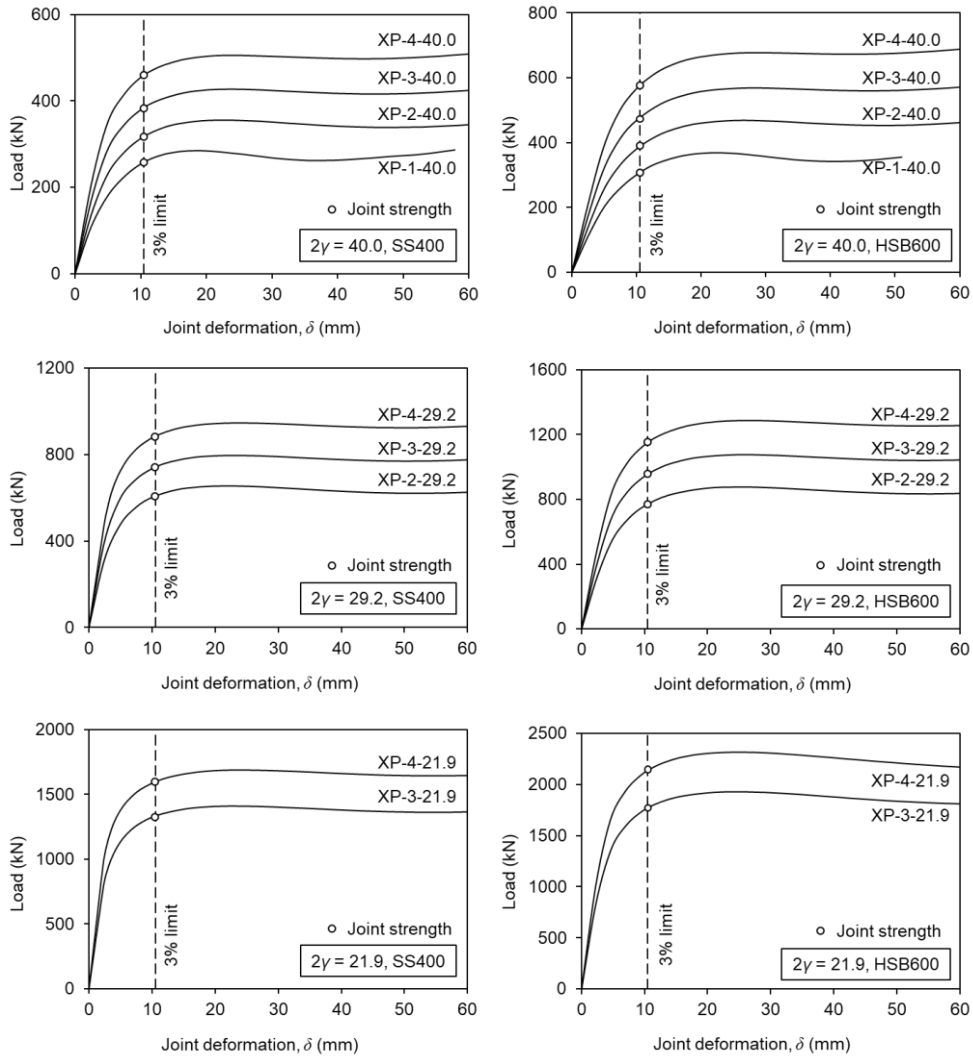

(a) SS400 (b) HSB600

Figure A.1. Load-deformation relationships for longitudinal X-type plate-to-CHS joints under axial compression

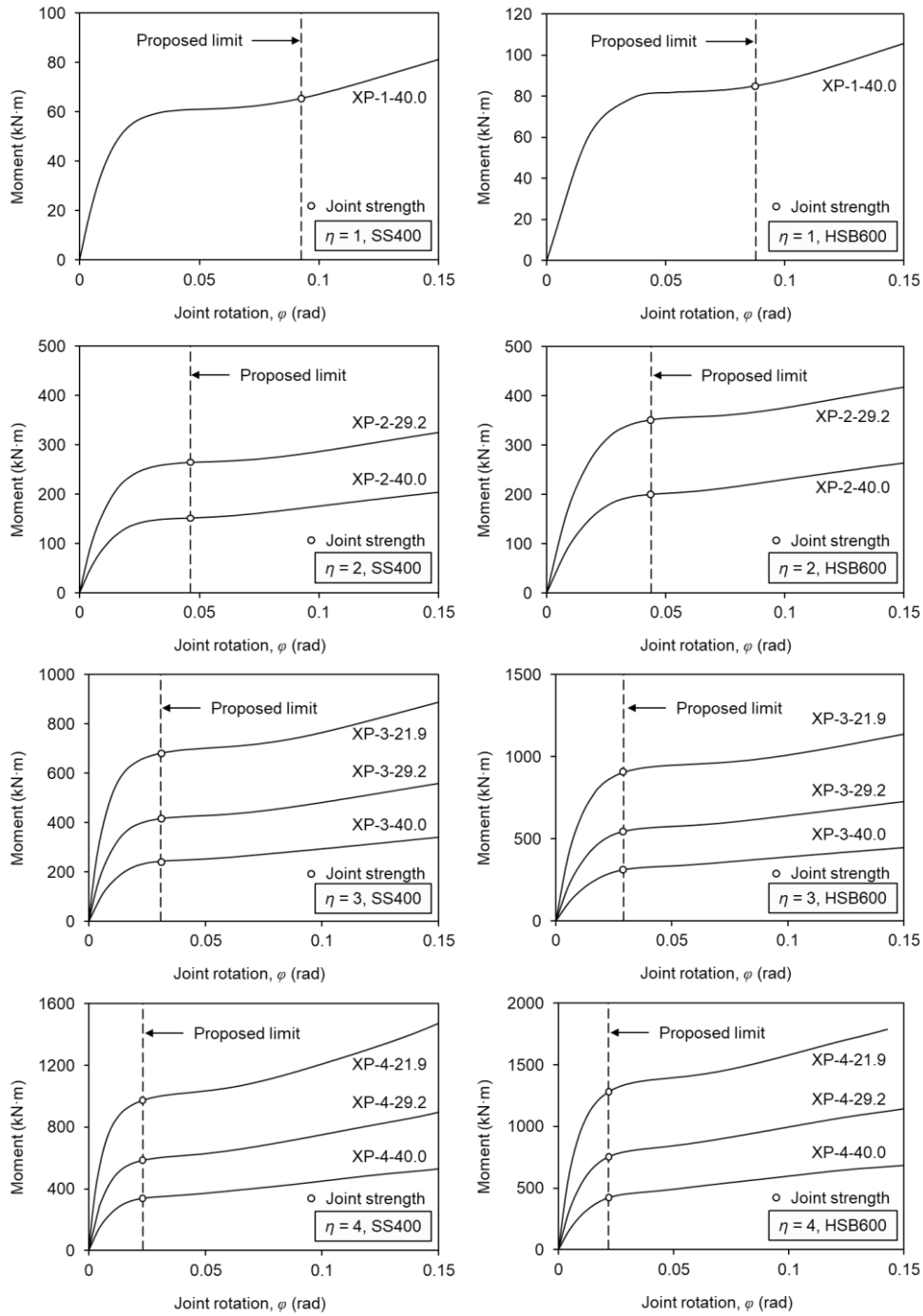

(a) SS400 (b) HSB600

Figure A.2. Moment-rotation relationships for longitudinal X-type plate-to-CHS joints under in-plane bending

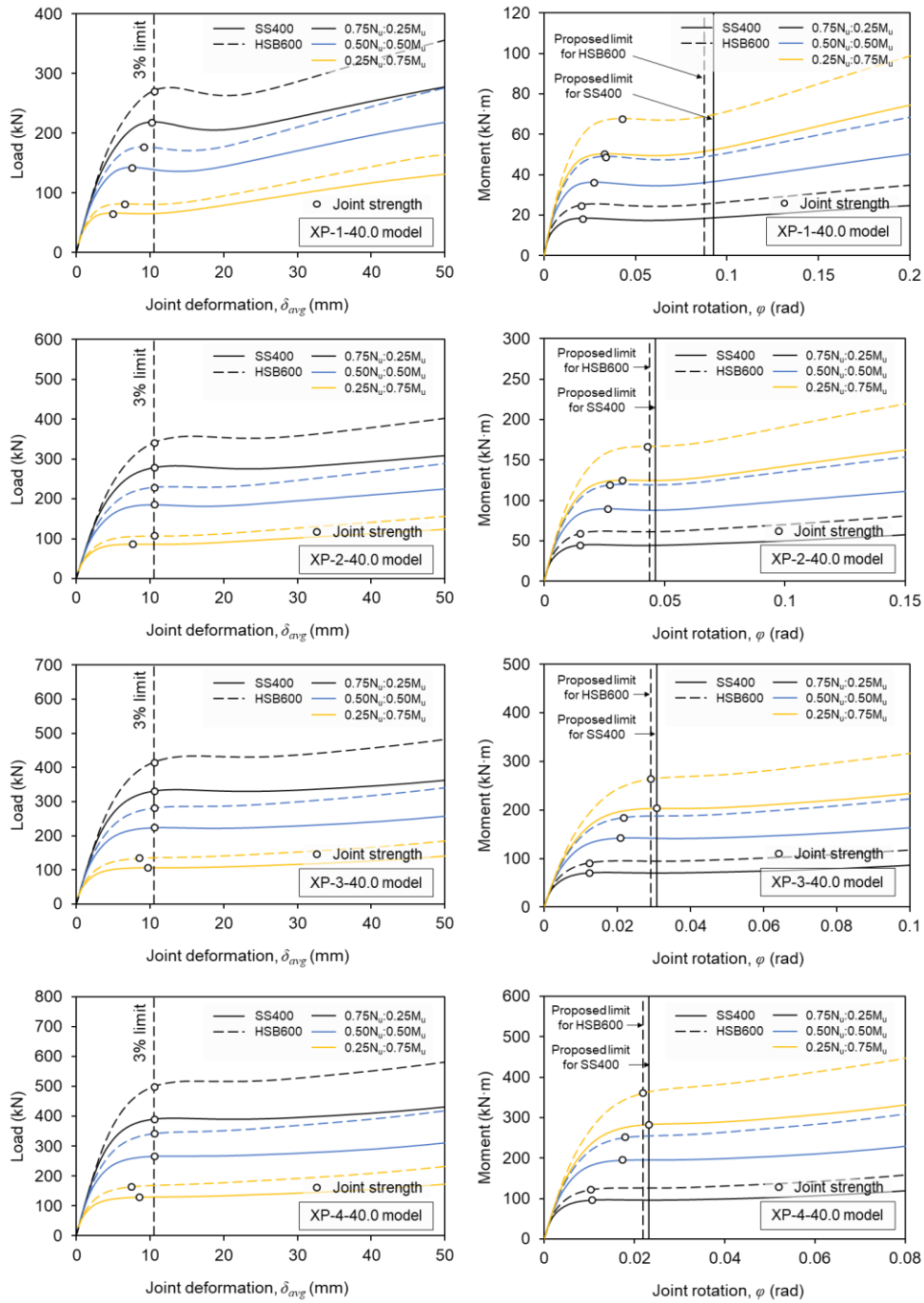

(a) Axial load-average indentation relationships

(b) IPB moment-rotation relationships

Figure A.3. Load-deformation relationships for longitudinal X-type plate-to-CHS joints under combined load (continued)

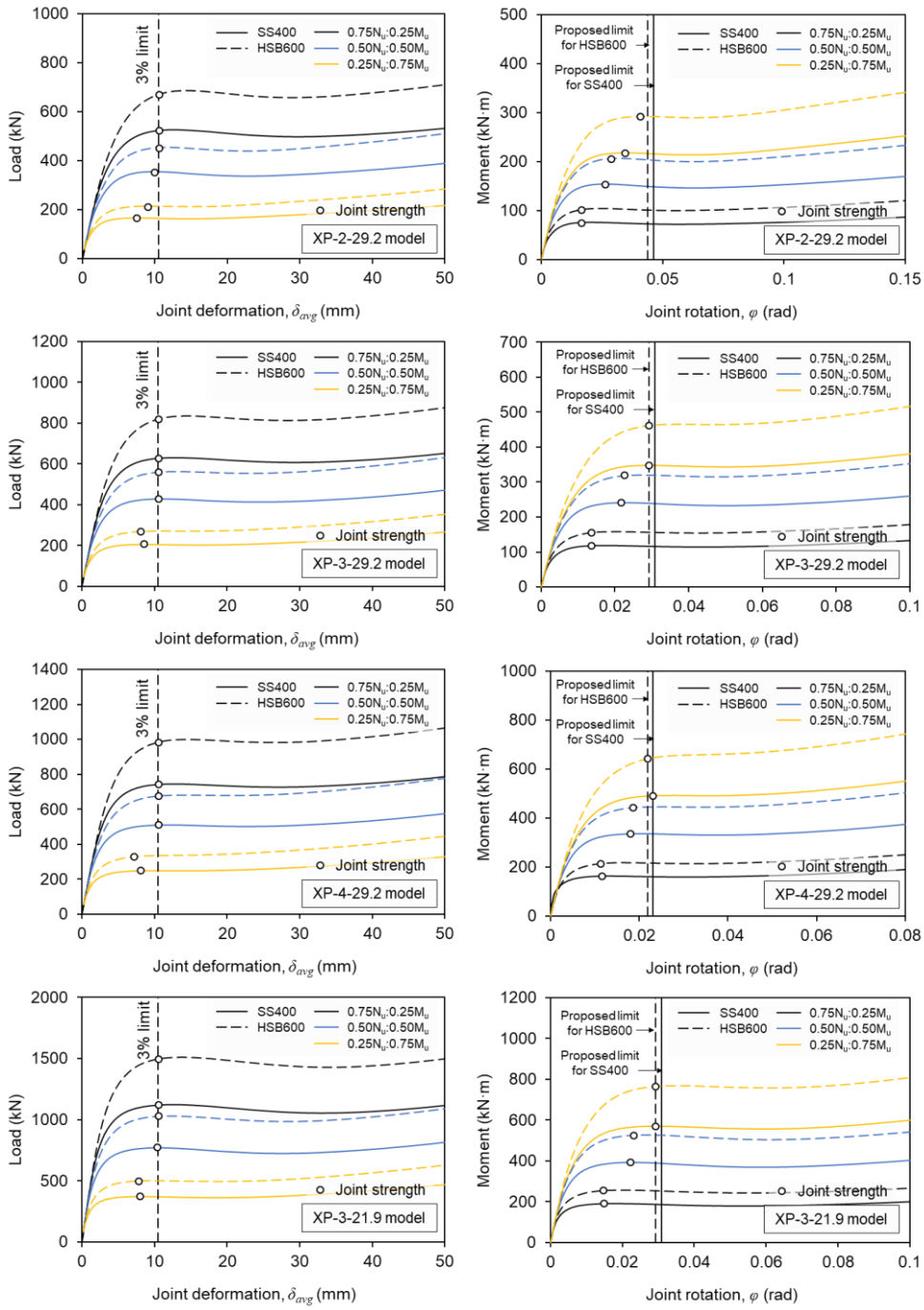

(a) Axial load-average indentation relationships

(b) IPB moment-rotation relationships

Figure A.3. Load-deformation relationships for longitudinal X-type plate-to-CHS joints under combined load (continued)

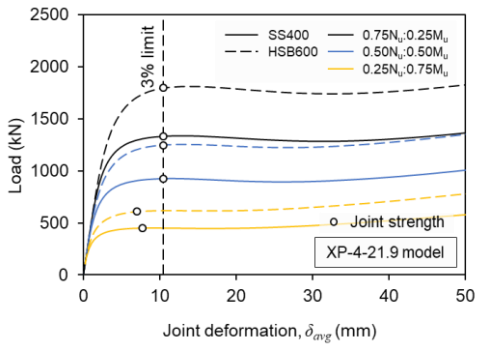

(a) Axial load-average indentation relationships

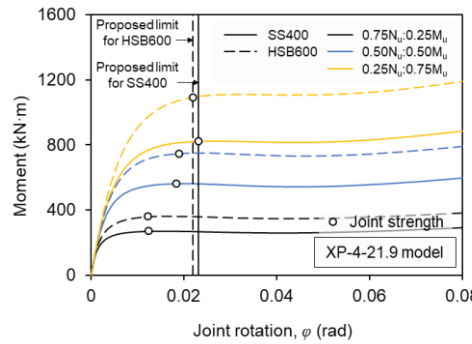

(b) IPB moment-rotation relationships

Figure A.3. Load-deformation relationships for longitudinal X-type plate-to-CHS joints under combined load

Table A.2. Analysis results for longitudinal T-type plate-to-CHS joints (continued)

Model	η	2γ	f_{y0} (MPa)	Loading pattern N/N_u:M/M_u	N_{uc} (kN)	M_{uc} (kN·m)	N_{uc}/N_u	M_{uc}/M_u
TP-1-50.0	1.3	50.0	356	Pure axial	227.5	0.0	1.00	0.00
				0.75:0.25	180.5 [a]	16.3 [a]	0.79	0.26
				0.50:0.50	120.1 [a]	32.6 [a]	0.53	0.53
				0.25:0.75	57.2 [a]	46.6 [a]	0.25	0.75
				Pure IPB	0.0	61.8	0.00	1.00
			478	Pure axial	273.4	0.0	1.00	0.00
				0.75:0.25	226.9	22.1	0.83	0.28
				0.50:0.50	148.9 [a]	43.5 [a]	0.54	0.54
				0.25:0.75	70.6 [a]	61.9 [a]	0.26	0.77
				Pure IPB	0.0	79.9	0.00	1.00
TP-2-50.0	2	50.0	356	Pure axial	276.6	0.0	1.00	0.00
				0.75:0.25	222.8 [a]	28.1 [a]	0.81	0.27
				0.50:0.50	149.2 [a]	56.4 [a]	0.54	0.54
				0.25:0.75	71.8 [a]	81.5 [a]	0.26	0.78
				Pure IPB	0.0	104.6	0.00	1.00
			478	Pure axial	332.0	0.0	1.00	0.00
				0.75:0.25	278.1	38.2	0.84	0.28
				0.50:0.50	184.0 [a]	75.9 [a]	0.55	0.55
				0.25:0.75	88.5	109.5	0.27	0.80
				Pure IPB	0.0	136.9	0.00	1.00
TP-3-50.0	3	50.0	356	Pure axial	342.9	0.0	1.00	0.00
				0.75:0.25	277.6	47.4	0.81	0.27
				0.50:0.50	186.7 [a]	95.7 [a]	0.54	0.54
				0.25:0.75	91.3	140.3	0.27	0.80
				Pure IPB	0.0	175.8	0.00	1.00
			478	Pure axial	413.1	0.0	1.00	0.00
				0.75:0.25	347.3	63.4	0.84	0.28
				0.50:0.50	232.8	127.4	0.56	0.56
				0.25:0.75	112.4	184.6	0.27	0.82
				Pure IPB	0.0	226.1	0.00	1.00
TP-4-50.0	4	50.0	356	Pure axial	408.5	0.0	1.00	0.00
				0.75:0.25	331.5	68.2	0.81	0.27

[a] Joint strength which is determined at peak load

Table A.2. Analysis results for longitudinal T-type plate-to-CHS joints (continued)

Model	η	2γ	f_{y0} (MPa)	Loading pattern N/N_u:M/M_u	N_{uc} (kN)	M_{uc} (kN·m)	N_{uc}/N_u	M_{uc}/M_u
TP-4-50.0	4	50.0	356	0.50:0.50	224.9	138.8	0.55	0.55
				0.25:0.75	110.2	204.1	0.27	0.81
				Pure IPB	0.0	252.1	0.00	1.00
			478	Pure axial	493.7	0.0	1.00	0.00
				0.75:0.25	416.2	89.6	0.84	0.28
				0.50:0.50	282.2	182.3	0.57	0.57
				0.25:0.75	136.0	263.5	0.28	0.83
				Pure IPB	0.0	318.9	0.00	1.00
TP-2-39.8	2	39.8	356	Pure axial	447.5	0.0	1.00	0.00
				0.75:0.25	359.2	42.3	0.80	0.27
				0.50:0.50	242.9 [a]	85.9 [a]	0.54	0.54
				0.25:0.75	117.2 [a]	124.3 [a]	0.26	0.79
				Pure IPB	0.0	158.2	0.00	1.00
			478	Pure axial	552.7	0.0	1.00	0.00
				0.75:0.25	459.3	58.0	0.83	0.28
				0.50:0.50	305.9	115.9	0.55	0.55
				0.25:0.75	146.8	166.8	0.27	0.80
				Pure IPB	0.0	209.3	0.00	1.00
TP-3-39.8	3	39.8	356	Pure axial	558.5	0.0	1.00	0.00
				0.75:0.25	449.1	71.7	0.80	0.27
				0.50:0.50	304.8	145.9	0.55	0.55
				0.25:0.75	148.6	213.3	0.27	0.80
				Pure IPB	0.0	267.3	0.00	1.00
			478	Pure axial	694.6	0.0	1.00	0.00
				0.75:0.25	577.2	96.7	0.83	0.28
				0.50:0.50	388.2	195.1	0.56	0.56
				0.25:0.75	188.2	283.8	0.27	0.81
				Pure IPB	0.0	349.0	0.00	1.00
TP-4-39.8	4	39.8	356	Pure axial	667.9	0.0	1.00	0.00
				0.75:0.25	536.7	103.3	0.80	0.27
				0.50:0.50	366.6	211.8	0.55	0.55
				0.25:0.75	179.9	311.8	0.27	0.81

[a] Joint strength which is determined at peak load

Table A.2. Analysis results for longitudinal T-type plate-to-CHS joints

Model	η	2γ	f_{y0} (MPa)	Loading pattern N/N_u:M/M_u	N_{uc} (kN)	M_{uc} (kN·m)	N_{uc}/N_u	M_{uc}/M_u
TP-4-39.8	4	39.8	356	Pure IPB	0.0	385.9	0.00	1.00
			478	Pure axial	836.8	0.0	1.00	0.00
				0.75:0.25	692.4	136.9	0.83	0.28
				0.50:0.50	482.2	285.9	0.58	0.58
				0.25:0.75	228.9	407.2	0.27	0.82
				Pure IPB	0.0	496.2	0.00	1.00
TP-3-30.4	3	30.4	356	Pure axial	971.7	0.0	1.00	0.00
				0.75:0.25	780.6 [a]	116.6 [a]	0.80	0.27
				0.50:0.50	532.9 [a]	238.8 [a]	0.55	0.55
				0.25:0.75	259.3 [a]	348.6 [a]	0.27	0.80
				Pure IPB	0.0	435.4	0.00	1.00
			478	Pure axial	1259.2	0.0	1.00	0.00
				0.75:0.25	1025.9	156.0	0.81	0.27
				0.50:0.50	696.8 [a]	318.0 [a]	0.55	0.55
				0.25:0.75	340.0	465.4	0.27	0.81
				Pure IPB	0.0	574.6	0.00	1.00
TP-4-30.4	4	30.4	356	Pure axial	1167.6	0.0	1.00	0.00
				0.75:0.25	934.9 [a]	168.0 [a]	0.80	0.27
				0.50:0.50	642.6 [a]	346.4 [a]	0.55	0.55
				0.25:0.75	315.4	510.1	0.27	0.81
				Pure IPB	0.0	629.5	0.00	1.00
			478	Pure axial	1517.4	0.0	1.00	0.00
				0.75:0.25	1233.0	222.1	0.81	0.27
				0.50:0.50	845.6	456.9	0.56	0.56
				0.25:0.75	414.2	671.4	0.27	0.82
				Pure IPB	0.0	819.8	0.00	1.00

[a] Joint strength which is determined at peak load

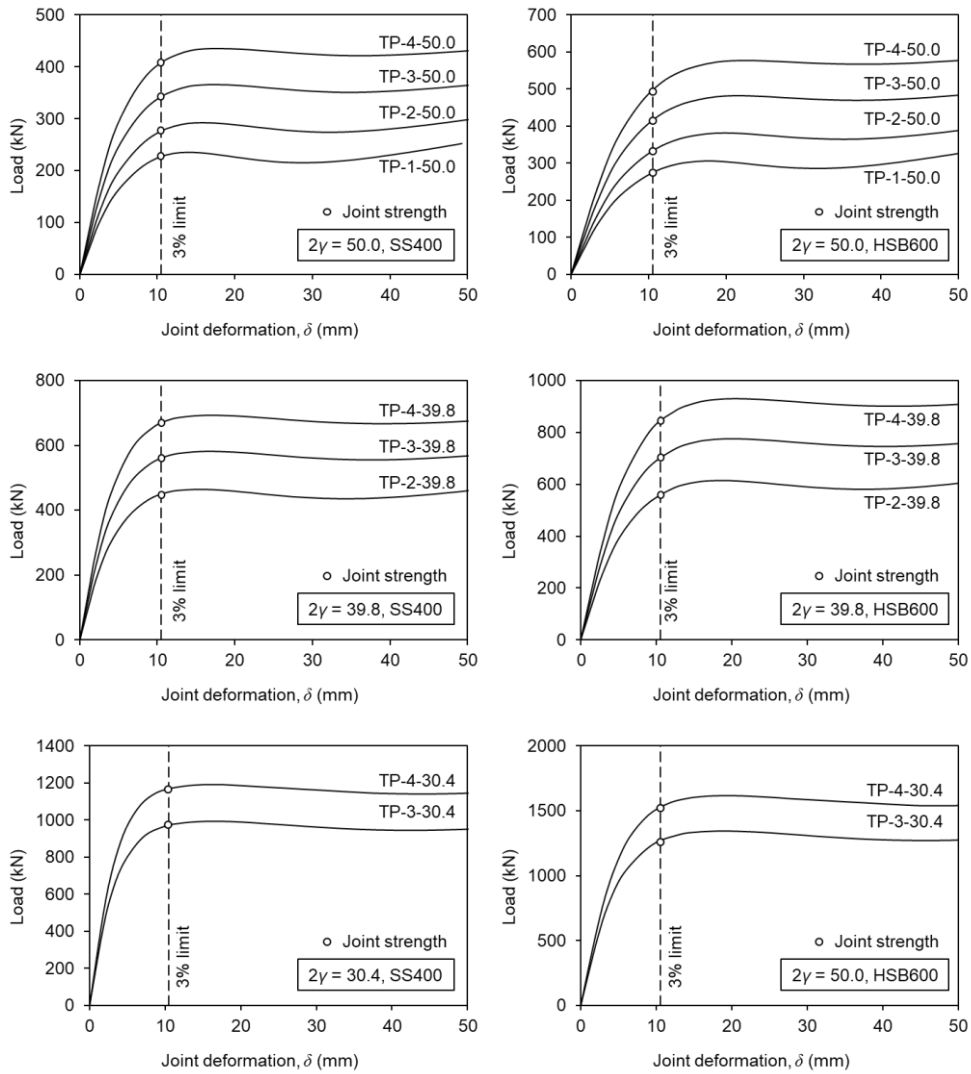

(a) SS400 (b) HSB600

Figure A.4. Load-deformation relationships for longitudinal T-type plate-to-CHS joints under axial compression

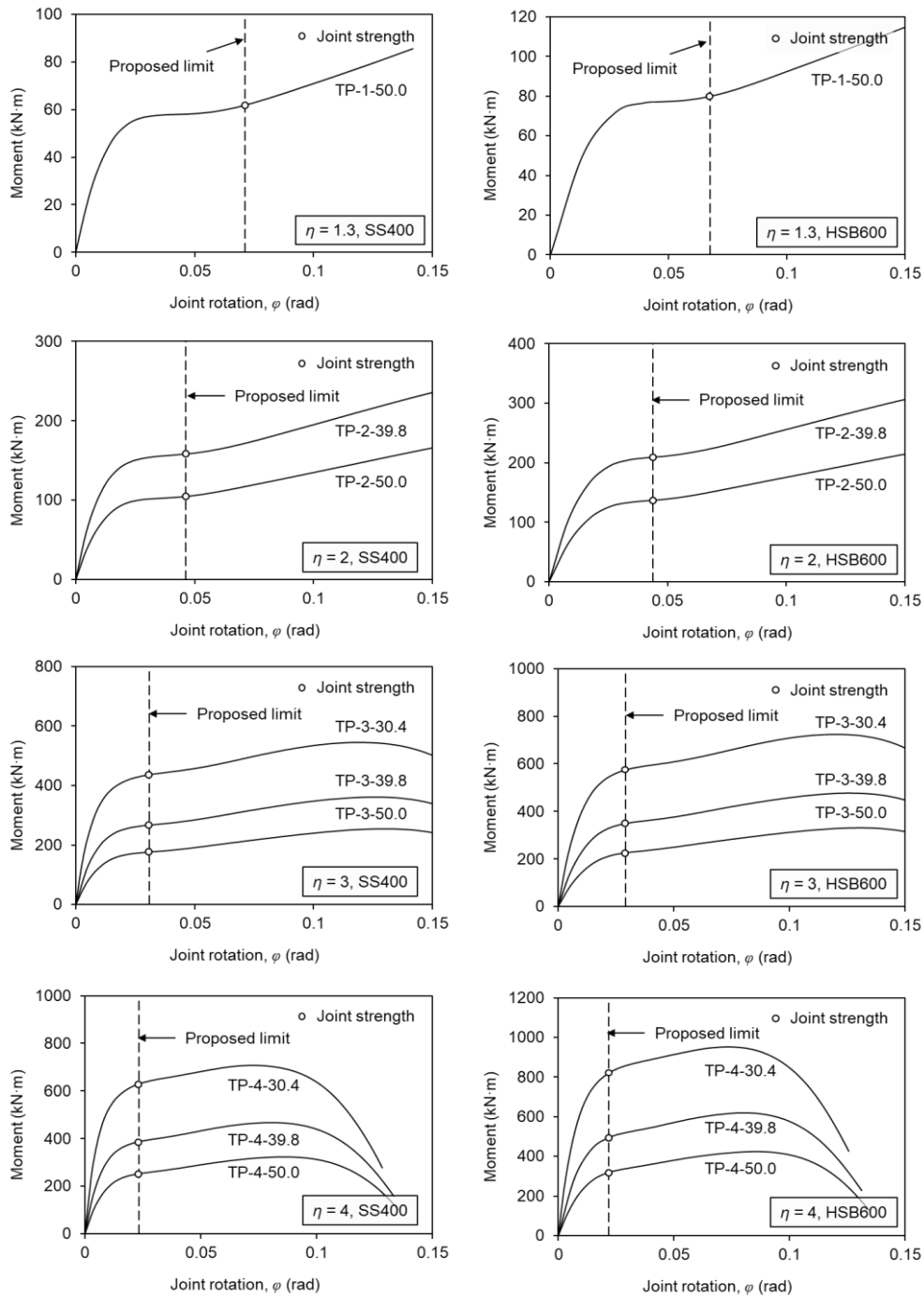

(a) SS400 (b) HSB600

Figure A.5. Moment-rotation relationships for longitudinal T-type plate-to-CHS joints under in-plane bending

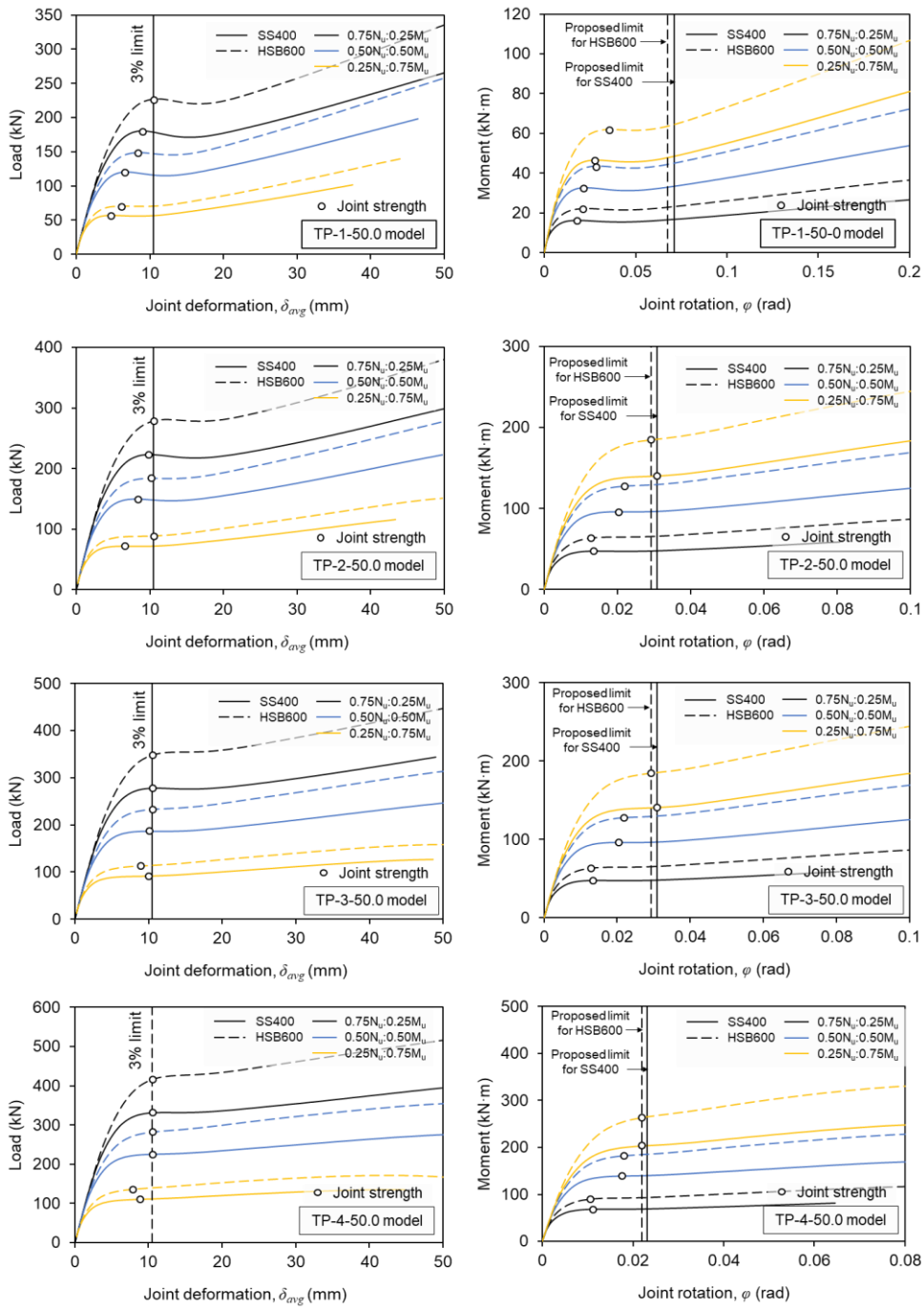

(a) Axial load-average indentation relationships

(b) IPB moment-rotation relationships

Figure A.6. Load-deformation relationships for longitudinal T-type plate-to-CHS joints under combined load (continued)

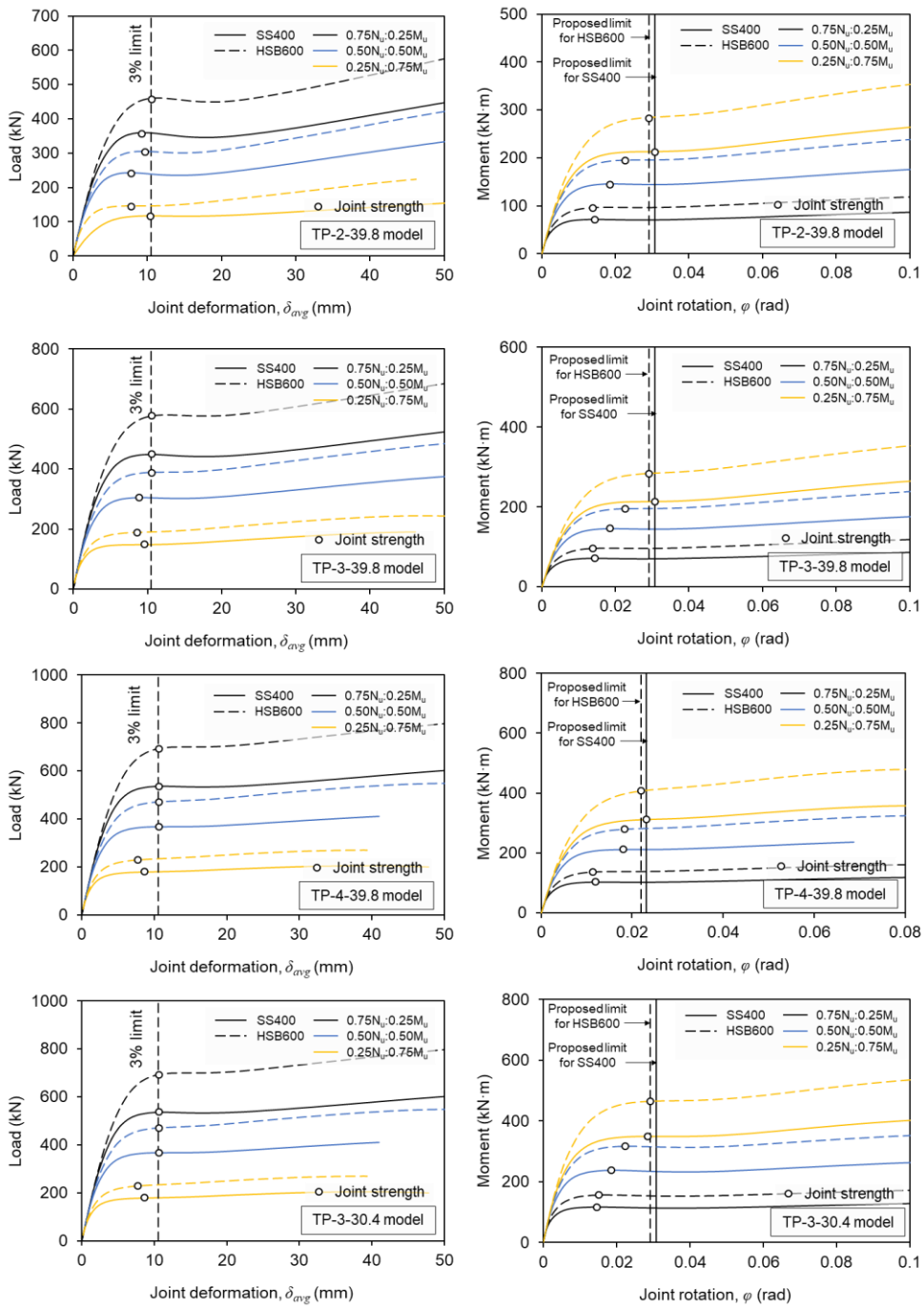

(a) Axial load-average indentation relationships

(b) IPB moment-rotation relationships

Figure A.6. Load-deformation relationships for longitudinal T-type plate-to-CHS joints under combined load (continued)

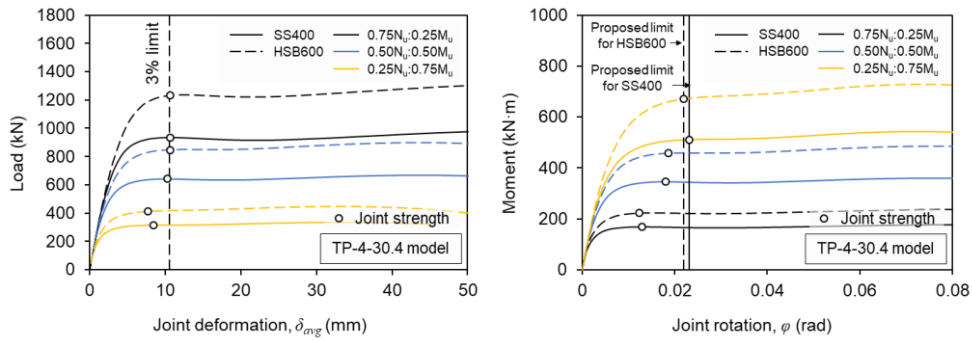

(a) Axial load-average indentation relationships

(b) IPB moment-rotation relationships

Figure A.6. Load-deformation relationships for longitudinal T-type plate-to-CHS joints under combined load

Table A.3. Analysis results for longitudinal T-type plate-to-CHS joints with $\beta' = 0.05$ under axial compression

Model	η	2γ	β'	N_u (kN)
TP-1-50.0 (R)	1.3	50.0	0.05	205.7
TP-2-50.0 (R)	2.0	50.0	0.05	251.4
TP-3-50.0 (R)	3.0	50.0	0.05	313.5
TP-4-50.0 (R)	4.0	50.0	0.05	374.7
TP-2-39.8 (R)	2.0	39.8	0.05	413.3
TP-3-39.8 (R)	3.0	39.8	0.05	519.4
TP-4-39.8 (R)	4.0	39.8	0.05	622.4
TP-3-30.4 (R)	3.0	30.4	0.05	913.0
TP-4-30.4 (R)	4.0	30.4	0.05	1099.9

Additional properties:
d_0 = 350 mm, t_1 = 12 mm, w = 3mm, L_0-h_1 = 3500 mm, $L_1 = 1.5h_1$, f_{y0} = 356 MPa

Table A.4. Analysis results for longitudinal X- and T-type plate-to-CHS joints with $\beta' = 0.05$ under in-plane bending

Model	η	2γ	β'	M_u (kN·m)
XP-1-40.0 (R)	1.0	40.0	0.05	58.8
XP-2-40.0 (R)	2.0	40.0	0.05	139.8
XP-3-40.0 (R)	3.0	40.0	0.05	227.6
XP-4-40.0 (R)	4.0	40.0	0.05	315.6
XP-2-29.2 (R)	2.0	29.2	0.05	245.3
XP-3-29.2 (R)	3.0	29.2	0.05	393.6
XP-4-29.2 (R)	4.0	29.2	0.05	552.3
XP-3-21.9 (R)	3.0	21.9	0.05	644.5
XP-4-21.9 (R)	4.0	21.9	0.05	924.4
TP-1-50.0 (R)	1.3	50.0	0.05	56.2
TP-2-50.0 (R)	2.0	50.0	0.05	95.6
TP-3-50.0 (R)	3.0	50.0	0.05	161.2
TP-4-50.0 (R)	4.0	50.0	0.05	232.6
TP-2-39.8 (R)	2.0	39.8	0.05	144.8
TP-3-39.8 (R)	3.0	39.8	0.05	241.1
TP-4-39.8 (R)	4.0	39.8	0.05	358.8
TP-3-30.4 (R)	3.0	30.4	0.05	406.1
TP-4-30.4 (R)	4.0	30.4	0.05	588.7

Additional properties:
d_0 = 350 mm, t_1 = 12 mm, w = 3mm, L_0 = 3500 mm (XP), L_0-h_1 = 3500 mm (TP), $L_1 = 1.5h_1$, f_{y0} = 356 MPa

Abstract (in Korean)

기존 유로코드의 개정안인 prEN 1993-1-8 에서는 플레이트가 용접된 강관접합부에 대한 최신의 설계기준을 제안하고 있다. 설계기준에서는 플레이트-원형강관 접합부에 항복강도 460MPa 이하의 고강도강을 적용할 것을 제시하며, 이때 항복강도가 355MPa 이상일 경우에는 재료계수(또는 강도저감계수) 0.9 를 사용하여 설계강도를 저감시켜야 한다. 이러한 고강도강에 대한 제한사항은 일반강에 비해 낮은 고강도강의 연성에 대한 우려 때문이다. 그러나 기준에서의 규제는 그 역학적 근거가 불분명하여 이에 대한 타당성을 확보할 필요가 있다. 본 논문에서는 실험 및 수치해석을 통해 고강도강을 적용한 플레이트-원형강관 접합부의 강도 및 연성을 검토하여 고강도강에 대한 현행의 제한사항을 평가하였다. 한편, 설계기준에서는 플레이트-원형강관 접합부가 축력과 면내휨의 조합력을 받을 때 그들의 상관관계식을 제시하지 않고 있다. 따라서 조합력을 받는 횡방향 플레이트-원형강관 접합부에 대한 해석적 연구를 통해 상관관계를 정립하고자 하였다.

실험에서는 횡방향 X 형 플레이트-원형강관 접합부에 대해 항복강도 460 또는 700 MPa 의 고강도강을 적용하였다. 실험 결과, 모든 고강도강 접합부는 접합부의 강도가 결정되는 변형한계와 비교했을 때 충분한 변형 능력을 갖고 있음을 확인하였으며, 접합부의 강도 또한 일반강에 비견될 만한 성능을 보였다. 이에 따라 설계기준에서 제시하는 항복강도 상한(f_y = 460MPa)이 완화될 수 있음을 제시하였다. 또한, 검증된 수치해석 기법을 사용하여

기준에서 제시하고 있는 재료계수를 평가하였다. 횡방향 X 형, T 형 플레이트-원형강관 접합부에 압축력, 면내휨, 그리고 압축력과 면내휨의 조합력을 가하였으며, 해석에 고려된 접합부의 기하학적 형상은 주관소성화 파괴모드만 유도될 수 있도록 선정되었다. 해석적 연구를 통해 플레이트-원형강관 접합부에 면내휨이 작용할 때 강관접합부에서 널리 사용되는 3% 변형한계 기준의 사용은 대체로 보수적인 접합부 강도를 제공하였다. 따라서 3% 변형한계 기준을 기반으로 추가적인 보정을 통해 보다 합리적인 회전각 변형한계 기준을 제시하였다. 새롭게 정의한 변형한계 기준을 사용하여 기준에서 제시하는 항복강도 460MPa 에 대한 재료계수 0.9 가 하중 조건에 관계없이 X 형, T 형 접합부에 적절함을 확인하였다. 더불어 조합력을 받는 플레이트-원형강관 접합부의 경우, 선형 상관관계식을 사용할 것을 새롭게 제시하였다.

주요어: 고강도강; 플레이트-원형강관 접합부; X 형 접합부; T 형 접합부; P-M 상관관계;

학 번: 2019-29294